

Universidade de São Paulo  
Instituto de Física

# Impurezas magnéticas no modelo de Kane-Mele com supercondutividade

Raphael Levy Ruscio Castro Teixeira

Orientador: Prof. Dr. Luis Gregório G. de V. Dias da Silva

Dissertação de mestrado apresentada ao Instituto de  
Física da Universidade de São Paulo, como requisito par-  
cial para a obtenção do título de Mestre(a) em Ciências.

Banca Examinadora:

Prof. Dr. Luis Gregório G. de V. Dias da Silva - IFUSP  
Prof. Dr. Eric de Castro e Andrade - IFSC/USP  
Prof. Dr. Edson Vernek - UFU

São Paulo  
2018

**FICHA CATALOGRÁFICA**  
**Preparada pelo Serviço de Biblioteca e Informação**  
**do Instituto de Física da Universidade de São Paulo**

Teixeira, Raphael Levy Ruscio Castro

Impurezas magnéticas no modelo de Kane-Mele com  
supercondutividade. São Paulo, 2018.

Dissertação (Mestrado) – Universidade de São Paulo. Instituto de  
Física. Depto. de Física dos Materiais e Mecânica.

Orientador: Prof. Dr. Luis Gregório Godoy de Vasconcellos Dias da  
Silva

Área de Concentração: Física.

Unitermos: 1. Física teórica; 2. Física da matéria condensada; 3.  
Sistema quântica; 4. Supercondutividade.

USP/IF/SBI-032/2018

University of São Paulo  
Physics Institute

# Magnetic impurities in the superconducting Kane-Mele model

Raphael Levy Ruscio Castro Teixeira

Supervisor: Prof. Dr. Luis Gregório G. de V. Dias da Silva

Dissertation submitted to the Physics Institute of the  
University of São Paulo in partial fulfillment of the  
requirements for the degree of Master of Science.

Examining Committee:

Prof. Dr. Luis Gregório G. de V. Dias da Silva - IFUSP  
Prof. Dr. Eric de Castro e Andrade - IFSC/USP  
Prof. Dr. Edson Vernek- UFU

São Paulo  
2018



*To my parents.*



# Acknowledgments

During the past few years, in special the last two, I learned a lot both of the subject covered in this work but about others too. I end this thesis with even more passion for this subject than when I started.

Many were those who helped in one way or another shaped this work, I do not have the pretentiousness to believe that I would be able to thank everyone. However, I would like to thank some of the most important ones.

To Prof. Dr. Luis Gregório Dias da Silva, I thank you for being a great advisor and to whom I am grateful for first teaching me about topological condensed matter. I also thank you for always support my dream of studying abroad.

To Prof. Dr. Annica Black-Schaffer, I thank you for accepting me in your group during my exchange. I learned a lot from it, and some of your directions helped shape this work.

To Prof. Dr. Carlos Moyses Graca Araujo, I thank you for helping with the reception and looking out for us during the exchange.

To Dr. Dushko Kuzmanovski, I thank you for advising me during my stay in Uppsala. Most of what I learned there was thanks to the weekly meetings.

To my mother, Maria Paula, who was always supportive of my choices and helping me during difficult times. In special, I thank you for some of the figures in this work. Without whom everything would have been more difficult.

To my grandparents, Ellis and Myrna Levy Ruscio and Ignes Castro, for all the support and discussions during all these years.

To my friends that helped me go through Uppsala winter, always willing to go to Fika or drink some beer, Felipe Sá, Gabriel Nagaoka, Mirco di Gioia and Severino Adler.

To my long-lasting friends, Humberto Akira, Radharani Kanesiro, Rodrigo Morimoto and Natália Zakalski for those long years of friendship and discussions that helped shaping me.

To my room colleagues Dimy Nancles, Jesús Cifuentes and Marcos Medeiros for discussions about topological condensed matter that helped with my understanding of the subject.

To Uppsala University and Physics Institute of University of São Paulo, for the exchange program that allowed most of the work presented here.

Last not least, to CNPq for the financial support that without it none of this work would have been possible.

*”You say the speculative topics are useless. Useless to whom? Only to people who don’t use them as they should. I mean, salves and ointments are not useless to people who apply them when and how they’re supposed to; weights are not useless in themselves, they’re useful to some people, worthless to others.”*

Epictetus, Discourses II, 21.20



# Resumo

Neste trabalho estudamos uma rede hexagonal com uma cadeia de impurezas nas bordas e com supercondutividade induzida, de forma a mostrar a existência de fases com férmiões de Majorana.

Para tal, começamos introduzindo invariantes topológicos, número de Chern e  $Z_2$  e mostramos dois modelos para rede hexagonal. O primeiro, modelo de Haldane, fazemos como motivação histórica. O segundo, modelo de Kane-Mele[1], é usado como base para todo o trabalho.

Seguimos introduzindo supercondutividade e como ela ocorre quando aplicada junto do Modelo de Kane-Mele, o método auto-consistente e quais as condições necessárias para termos supercondutividade apenas nas bordas. Continuamos com efeitos de impurezas magnéticas nas bordas e introduzimos férmiões de Majorana que são os alvos principais dos resultados.

Mostramos então, que existe fases topológicas em cadeias de impureza magnética, com momentos em espiral, contudo o diagrama de fase depende de várias condições. Por fim, mostramos que a variação da fase topológica se deve a oscilações nos níveis de energia em que o invariante topológico também varia, contrariando resultados obtidos para a rede quadrada[2].

Concluímos esse trabalho com implicações experimentais desse resultado e possíveis caminhos que podem ser seguidos.

**Palavras-chave:** Kane-Mele; Isolantes topológicos; Supercondutividade; Férmiões de Majorana.



# Abstract

In this work, we study a honeycomb lattice with induced superconductivity and edge impurity in order to show the existence of a phase that host Majorana bound state.

To do so, we start introducing topological invariants, Chern number and  $Z_2$ , and we show two models for honeycomb lattice. The first, Haldane's Model, due its historical importance. The second, Kane-Mele model[1], because it will be used during all this work.

Then we review superconductivity, showing the self-consistent method, and we apply it to Kane-Mele model, in which we find some necessary conditions to induce superconductivity only at the edges. From this point, we study the effect of magnetic impurities at the edges, and we introduce Majorana bound state, that will be the main objective of our results.

In our results, we show the existence of topological non-trivial phases for spiral magnetic chain in the zigzag edge. With this we make a phase diagram. We also find oscillation in the energy spectrum and the topological phase changes with the oscillation, this is different from square lattice in which we should not have a change in the topological phase[2].

We conclude this work with experimental implications of our result and possible developments.

**Keywords:** Kane-Mele; Topological Insulators; Superconductivity; Majorana bound states.



# Contents

<b>1</b>	<b>Introduction</b>	<b>21</b>
1.1	Topological insulators . . . . .	23
1.2	Honeycomb lattice materials . . . . .	23
1.3	Majorana zero modes . . . . .	24
1.4	Dissertation outline . . . . .	26
<b>2</b>	<b>Topological invariants for honeycomb lattice</b>	<b>27</b>
2.1	Topological Invariants . . . . .	27
2.1.1	Chern Number . . . . .	28
2.1.2	Kramers' Theorem . . . . .	29
2.1.3	$Z_2$ . . . . .	30
2.2	Honeycomb lattice models . . . . .	33
2.2.1	Haldane Model . . . . .	33
2.2.2	Kane-Mele model . . . . .	35
<b>3</b>	<b>Superconductivity and Impurities</b>	<b>41</b>
3.1	Superconductivity . . . . .	41
3.1.1	Introduction to superconductivity . . . . .	41
3.1.2	The self-consistency method . . . . .	42
3.1.3	The free-energy . . . . .	43
3.1.4	The superconductivity for electrons on a honeycomb lattice . . . . .	44
3.2	Impurities . . . . .	47
3.2.1	A single impurity in the superconducting Kane-Mele model . . . . .	47
<b>4</b>	<b>Majorana bound states</b>	<b>53</b>
4.1	Introduction . . . . .	53

## CONTENTS

4.1.1	Protected zero-modes . . . . .	54
4.1.2	Non-Abelian statistics . . . . .	55
4.2	Realizing Majorana bound states in 1D chain . . . . .	57
4.2.1	The Kitaev chain . . . . .	57
4.2.2	Physical realization - Semiconductor wire . . . . .	60
<b>5</b>	<b>Majorana in the superconducting Kane-Mele</b>	<b>63</b>
5.1	Preliminary results . . . . .	63
5.2	Square lattice . . . . .	65
5.3	Superconducting Kane-Mele model . . . . .	68
5.3.1	Zigzag edge . . . . .	68
5.4	Gap oscillations . . . . .	74
5.4.1	Armchair edge . . . . .	78
<b>6</b>	<b>Conclusions</b>	<b>81</b>
6.1	Overview . . . . .	81
6.2	Superconducting Kane-Mele model . . . . .	81
6.3	Gap oscillations . . . . .	82
6.4	Experimental implications . . . . .	83
6.5	Further developments . . . . .	83
<b>A</b>	<b>Pfaffian</b>	<b>85</b>
<b>B</b>	<b>Derivation Kane-Mele</b>	<b>87</b>
<b>C</b>	<b>Oscillations</b>	<b>95</b>

# List of Figures

1.1	Figure from [10]. The structure of silicene or stanene is buckled instead of planar as happens with graphene. . . . .	24
1.2	Adapted from [13]. (a) The differential conductance, we can see a zero energy peak for $B > 90\text{mT}$ . (b) The experimental setup, with the superconducting region (S), normal region (N), magnetic field B, and gates 1 to 4. . . . .	25
2.1	Haldane's model. Region a has flux $\phi$ region b has flux $-\phi$ in this way the total flux over the unitary cell is zero. Here we show some vectors that will be used latter. The dashed vectors indicate the direction considered for the phase in the hopping. . . . .	33
2.2	Energy bands with. (a) $M = +3\sqrt{3}t_2 \sin(\phi)$ and (b) $M = -3\sqrt{3}t_2 \sin(\phi)$ . . . . .	34
2.3	Phase diagram with the Chern number for Haldane model. . . . .	35
2.4	Phase diagram for Kane-Mele model. The gray area in the middle is the topological non-trivial phase. This is valid for $\lambda_{SO} \ll t$ . . . . .	37
2.5	Honeycomb edges.(a) Zigzag edge and (b) armchair edge. . . . .	37
2.6	Hexagonal structure, with sublattice A (black dot, $\xi = 1$ ) and B (white dot, $\xi = -1$ ). The figure shows the choice of numbering the strips. In gray is the choice of basis for the tight-biding. . . . .	38
2.7	Energy bands for a 20-strips. The values used for calculations were $\lambda_{SO} = 0.5t$ , $\lambda_R = 0.08t$ (a) $\lambda_v=0.15t$ and (b) $\lambda_v=0.6t$ . We can see in the first plot the edge states that cross the fermi energy while in the second plot is a normal insulator. . . . .	38
2.8	Plot of gap $\Delta$ in units of $E/t$ by the number of strips ( $N_{strips}$ ), for multiples $\lambda_v$ . For this calculation we used $\lambda_{so}/t = 0.6$ . . . . .	39
2.9	Plot of gap $\Delta$ in units of $E/t$ for 3 different number of strips ( $N_{strips}$ ). . . . .	39

## LIST OF FIGURES

2.10 Density plot of gap $\Delta$ in units of $E/t$ for different number of strips, when changing the parameters $\lambda_r$ and $\lambda_v$ . To produce those plots, it was used $\lambda_{so} = 0.6$ . We can compare this figures with figure 2.4 and we see that the gap going to zero is different from the quasi-1D with small number of strips and the bulk version. . . . .	40
3.1 Numerical error given by absolute value of the difference between two successive $\Delta$ over the number of iterations. . . . .	43
3.2 The system considered with 400-atoms over a superconductor which leads to an induced superconductivity. . . . .	45
3.3 Doping ( $\mu$ ) effect on superconductivity order parameter at different positions for sublattice A and B. (a) Zigzag edge. (b) Armchair edge. (c) Middle of the sample. . . . .	45
3.4 Staggering potential ( $\lambda_v$ ) effect on superconductivity order parameter at different positions for sublattice A and B. (a) Zigzag edge. (b) Armchair edge. (c) Middle of the sample. . . . .	46
3.5 Rashba spin-orbit ( $\lambda_r$ ) effect on superconductivity order parameter at different positions for sublattice A and B. (a) Zigzag edge. (b) Armchair edge. (c) Middle of the sample. . . . .	46
3.6 Pair attraction potential( $U$ ) effect on superconductivity order parameter at different positions for sublattice A and B. (a) Zigzag edge. (b) Armchair edge. (c) Middle of the sample. . . . .	47
3.7 Dependence of the energy with the strength of the impurity scattering for (a) nonmagnetic scattering, (b) magnetic in $\vec{z}$ direction, (c) magnetic in $\vec{x}$ direction, (d) magnetic in $\vec{y}$ direction . . . . .	48
3.8 Detailed dependence of the energy with the strength of the impurity scattering for magnetic in $\vec{x}$ direction. (a) In the superconductivity regime, $\lambda_v = 0$ . (b) In the normal regime, $\lambda_v = 0.6t$ . We can see a difference in the value of $V_z$ in which exists a zero energy state. . . . .	49
3.9 Superconductivity order parameter $\Delta$ at the impurity, at left the absolute value and at right the phase. We can see a transition at $V_z = 1.3$ . . . . .	49
3.10 Difference of the free-energy from superconductivity state and normal state for $\lambda_v = 0$ . . . . .	50

## LIST OF FIGURES

3.11 Magnetization of the system with $V_z=1.4t$ for many $\lambda_v$ , in the direction (a) parallel to $V_z$ , (b) perpendicular to $V_z$ . The position axis represents the number of the site at the zigzag edge. The impurity is in position 11. . . . .	51
4.1 Exchange of Majorana zero modes. . . . .	55
4.2 Exchange of two Majorana bound states in a two electron system. . . . .	56
4.3 Adapted from [29]. Kitaev chain for the case $\mu \neq 0$ , $t = \Delta = 0$ , in which Majorana bound states interacts with others in the same site. . . . .	58
4.4 Adapted from [29]. Kitaev chain for the case $\mu = 0$ , $t = \Delta \neq 0$ , we have that Majorana bound states interact with others in the next site . . . . .	58
4.5 Illustration of the two phases in Kitaev model, topological trivial (white) and topological superconductor (shaded). . . . .	59
4.6 Adapted from [3]. (a) Structure required to have stable topological phase in a 1D wire with spin-orbit. (b) Band structure for the wire with time-reversal symmetry, bands blue and red due to spin-orbit, and when its broken, black band. When the chemical potential is inside the gap at $k=0$ , the wire can be viewed as spinless. . . . .	60
4.7 Phase diagram for the semiconducting wire. . . . .	61
5.1 Impurity chain diagrams and the energy levels for both the ferromagnetic and antiferromagnetic cases. Some impurities were labeled from 1 to 6. . . .	64
5.2 LDOS for the ferromagnetic case, in the impurities labeled as fig.5.1. . . .	64
5.3 LDOS for the antiferromagnetic case, in the impurities labeled as fig.5.1. .	65
5.4 Figure from [31]. The sample considered, red circles with arrow indicate the impurity with its magnetic moment. . . . .	65
5.5 Oscillation in the gap for $\mu = 3t$ , (a) $G=0$ and $V_z=2.4t$ , (b) $G=1.01$ and $V_z=2t$ and (c) $G=3.14$ and $V_z=1.6t$ . . . . .	67
5.6 Configuration of our system. (a) the sample used with the impurities in the zigzag edge in red and in the armchair edge in blue. (b) the angle $\theta$ between two impurities. . . . .	68
5.7 Dependence of free-energy with $\theta$ for different $\mu$ . . . . .	69
5.8 LDOS for $E=0$ over the impurities for $V_z = 1.85t$ with $\theta$ shown in table5.1.	70

## *LIST OF FIGURES*

## LIST OF FIGURES

C.1	$\mu=0.4$ and $\theta = 3\pi/2$ . Oscillations with varying impurity strength $V_z$ for $\lambda_{so}$	
(a)	0.1t and (b) 0.3t.	95
C.2	$\mu=0.4$ and $\theta = \pi/2$ . Oscillations with varying impurity strength $V_z$ for $\lambda_v$	
(a)	0.05t and (b) 0.1t.	96
C.3	$\mu=0.4$ $\theta = \pi$ . Oscillations with varying impurity strength $V_z$ for $\lambda_r$ (a) 0,	
(b)	0.05t, (c) 0.1t and (d) 0.15t.	96
C.4	$\mu=0.4$ $\theta = 0$ . Oscillations with varying impurity strength $V_z$ for $\lambda_r$ (a) 0,	
(b)	0.05t, (c) 0.1t and (d) 0.15t.	97
C.5	$\mu=0.2$ $\theta = 0$ . Oscillations with varying impurity strength $V_z$ for $\lambda_r$ (a) 0,	
(b)	0.05t, (c) 0.1t and (d) 0.15t.	97
C.6	$\mu=0.2$ $\theta = \pi/2$ . Oscillations with varying impurity strength $V_z$ for $\lambda_r$ (a)	
(b)	0.05t, (c) 0.1t and (d) 0.15t.	98
C.7	$\mu=0.2$ $\theta = \pi$ . Oscillations with varying impurity strength $V_z$ for $\lambda_r$ (a) 0,	
(b)	0.05t, (c) 0.1t and (d) 0.15t.	98
C.8	$\mu=0.2$ $\theta = 0$ . Oscillations with varying impurity strength $V_z$ for $\lambda_r$ (a) 0,	
(b)	0.05t, (c) 0.1t and (d) 0.15t.	99
C.9	$\theta = 0$ . Oscillations with varying doping $\mu$ for $V_z$ (a) 1.45t and (b) 1.85t.	99

*LIST OF FIGURES*

# List of Tables

1.1	Values of parameters calculated with first principles[10]. Here, $t$ is hopping, $v_F$ the Fermi velocity, $a$ the lattice constant, $\lambda_{SO}$ the spin-orbit coupling, see equation 2.29, $l$ is the buckle height (distance between sublattices' planes) and $\theta$ is the bond angle . . . . .	24
5.1	Phase diagram with self-consistent method. The number inside the cell is $\theta/\pi$ . Yellow and green: Majorana Number +1 and the angle of the chain is clockwise and anticlockwise. Blue and red: Majorana Number -1 and the angle of the chain is clockwise and anticlockwise. A (*) means that exists more than one $\theta$ and they have different Majorana number. . . . .	69
5.2	Phase diagram without self-consistent method. The number inside the cell is $\theta/\pi$ . Yellow and green: Majorana Number +1 and the angle of the chain is clockwise and anticlockwise. Blue and red: Majorana Number -1 and the angle of the chain is clockwise and anticlockwise. A (*) means that exists more than one $\theta$ and they have different Majorana number. . . . .	71
5.3	Phase diagram with self-consistent method for a chain of 30 impurities. The number inside the cell is $\theta/\pi$ . Yellow and green: Majorana Number +1 and the angle of the chain is clockwise and anticlockwise. Blue and red: Majorana Number -1 and the angle of the chain is clockwise and anticlockwise. A (*) means that exists more than one $\theta$ and they have different Majorana number. . . . .	72
5.4	Phase diagram with self-consistent method. The number inside the cell is $\theta/\pi$ . Yellow: Majorana Number +1 and the angle of the chain is clockwise. . . . .	78
B.1	Table of values used to write the Hamiltonian at Eq. B.13 . . . . .	93

*LIST OF TABLES*

# Chapter 1

## Introduction

In this work, we study magnetic impurities at the edges of a honeycomb lattice with spin-orbit coupling and proximity-induced superconductivity. The motivation comes from the search for Majorana bound states and the possible application in quantum computation[3]. Allied with that we use as basis a honeycomb lattice, which due to its geometry brings some effects, and some materials, graphene, were even labeled "miraculous material" in the media due its possible applications.

However, here we are interested not in graphene but in materials with large spin-orbit coupling (SOC). When it is added in honeycomb lattice systems it makes possible the Quantum Spin Hall Effect in which we have chiral edge states that conducts spin currents[4]. SOC is also an important element when building a system that can host a Majorana bound state as it breaks the bands degeneracy due to spin[3].

In order to have a high SOC we are not interested in carbon atoms, graphene, but now we want silicon atoms, silicene, this of course changes a little the configuration and now the sublattice are in different planes, which in turn allow us to control the onsite energy with electric field.

Silicene on Ag(111) is known to have proximity induced superconductivity[5], a necessary element in the search for Majorana bound states. This happens because when silicene is deposited on a superconducting surface Cooper pairs flows mainly to metallic states inducing superconductivity . Because of this, we focus in silicene instead of graphene, although the parameter values used here may be different from silicene, we expect our conclusions to be applied to silicene.

In the next few sections, we introduce some important themes of this work, although

we shall see in more detail some of the topics in chapters 2 and 3.

## 1.1 Topological insulators

In Landau theory, spontaneous symmetry breaking describes phase transitions characterized by a local order parameter. However, with the discovery of Quantum Hall phase in the 1980's, topological order, which is a non-local order parameter, has been used to describe different states. For the Quantum Hall effect we can see that the Hall current is actually quantized, and a topological invariant[6] can describe the system.

It was latter found that a class of materials have a similar behavior, conducting, i.e. gapless modes, at the edges or surfaces while the bulk is insulating. These materials were called "topological insulators" and the non-locality property of the topological order plays a major role in phase transitions.

These edge states can be understood with Laughlin argument, in which they are a consequence of transverse quantized transport in an insulator[7]. Systems with Hall conductance have delocalized bulk states in valence band that rise in energy close to the edge and becomes a gapless edge mode.

This field has been experienced a fast growth and several materials have been proposed and showed to be topological insulators, in special we the HgTe/CdTe quantum well that has been proposed and confirmed experimentally. As example of the growing importance of this field is the 2016 Nobel prize given to Thouless, Haldane and Kosterlitz "for theoretical discoveries of topological phase transitions and topological phases of matter" [8].

We conclude this section, with a note about an abuse of notation. Sometimes we write just "topological phase", this should be understood as "topological non-trivial phase".

## 1.2 Honeycomb lattice materials

2D materials, in special the ones with honeycomb lattice, have been gathering a lot of attention. In 2010, the Nobel prize was awarded to Andre Geim and Konstantin Novoselov for "groundbreaking experiments regarding the two-dimensional material graphene" [9]. Since them a lot of studies have been focused in developing graphene and engineering it so it could be used in transistors.

However, similar materials with honeycomb lattice, are as promising as graphene. These materials in general have a difference in height between sublattices that can be used to control an onsite energy associated with the sublattice.

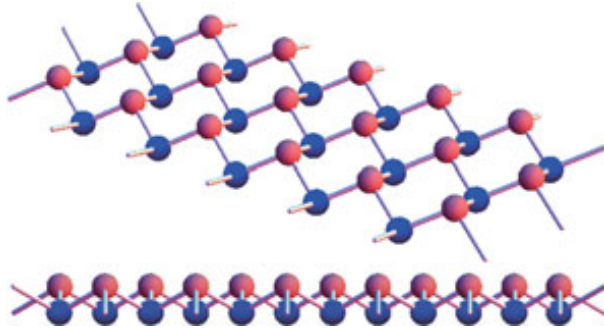


Figure 1.1: Figure from [10]. The structure of silicene or stanene is buckled instead of planar as happens with graphene.

Below we show two materials compared with graphene. First silicene which is based in Si and the second Stanene that is based on Sn.

	$t$ (eV)	$v_F$ ( $10^5$ m/s)	$a$ (Å)	$\lambda_{SO}$ (meV)	$l$	$\theta$
Graphene	2.8	9.8	2.46	$10^{-3}$	0	90
Silicene	1.6	5.5	3.86	3.9	0.23	101.7
Stanene	1.3	4.9	4.7	100	0.4	107.1

Table 1.1: Values of parameters calculated with first principles[10]. Here,  $t$  is hopping,  $v_F$  the Fermi velocity,  $a$  the lattice constant,  $\lambda_{SO}$  the spin-orbit coupling, see equation 2.29,  $l$  is the buckle height (distance between sublattices' planes) and  $\theta$  is the bond angle

An important note is that for silicene  $\lambda_{SO} \approx 2.4 \times 10^{-3}t$  however in this work we use the spin-orbit coupling two order of magnitude bigger. Stanene have spin-orbit of the order of magnitude used. Both materials are believed to host superconductivity when doped[5, 11].

### 1.3 Majorana zero modes

In this section we discuss a little about Majorana bound states, although a more in depth discussion is done in chapter 4, here we are interested in showing the field evolution and some experimental results that indicate the existence of Majorana bound states.

The first model to incorporate the idea of Majorana zero modes is from Alex Kitaev in 2001[12], in which he shows that under the right conditions we can have two unpaired modes at the end of an impurity chain. Since then, a lot of research was done in order to verify it experimentally.

The first observation was made in 2012 by Mourik et al[13], also called the Delft experiment. There they used a wire made of InSb deposited in a substrate with gates,

with a superconducting region (S) and normal region (N). The gates deplete the electron density in the superconducting region creating a weak link.

They measured the tunneling conductance current ( $I$ ) through the weak link under an applied bias  $V$ . In this regime the differential conductance  $dI/dV$  is proportional to density of states, so it's possible to probe the density of states. From the theory, we expect a zero mode to appear in the end of the superconducting region. Indeed, it was observed the existence of zero modes for a magnetic field  $B$  over 90 mT up to 400 mT. [13] [?]

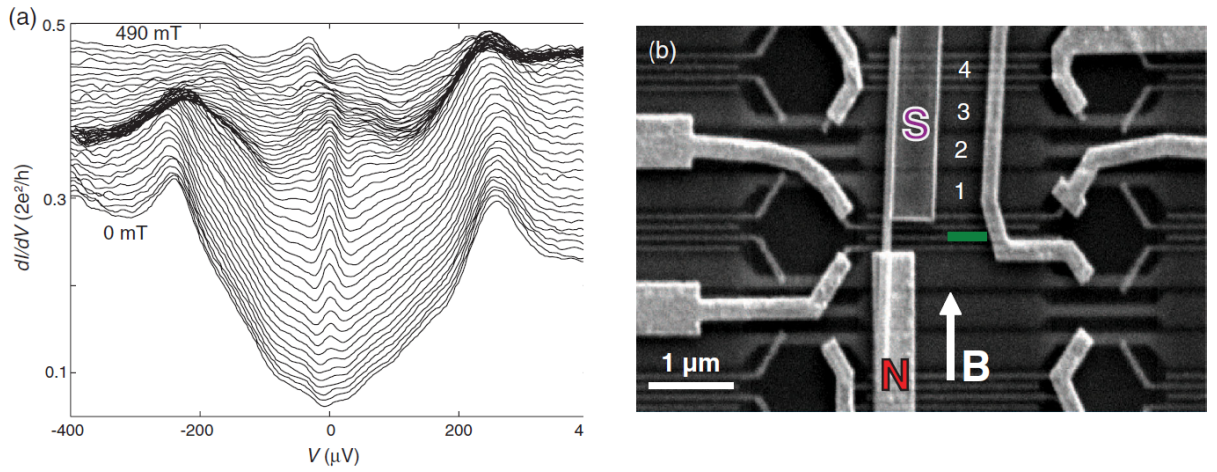


Figure 1.2: Adapted from [13]. (a) The differential conductance, we can see a zero energy peak for  $B > 90$  mT. (b) The experimental setup, with the superconducting region (S), normal region (N), magnetic field  $B$ , and gates 1 to 4.

Although it is seen as a compelling evidence of the existence of Majorana zero modes, it must be noted that zero bias anomalies sometimes happen when Majorana bound states isn't expected. Therefore, more evidence is needed to prove its existence.

Other ways to probe the existence of Majorana bound states have been proposed and realized[14]. As an example, we have half-integer conductance quantization,  $4\pi$ -periodic Josephson effect, exponential protection of zero-modes[15], and many more. However, until this day no definite proof of Majorana bound state exists.

In order to have an unequivocal proof, we could show the non-abelian property of Majorana bound states. This would also open the field of quantum computation using Majorana bound states.

Although the search for quasi-particle still carry on, all signs points to its existence. Because of this, many theoretical work is needed to understand it in order to use it to its full potential.

## 1.4 Dissertation outline

Here we present the general outline of this work. We can separate it in two main parts, the first composed of chapters 2 and 3 in which we present some key aspects of the model used and the theory with some small results. The second, composed of chapter 4 in which we show new results.

### **Chapter 2**

In this chapter we introduce some key aspects of topological invariants, deriving some important results. Then we study models in honeycomb lattice. We start with Haldane model due to its historic importance following with Kane-Mele model.

### **Chapter 3**

In this chapter we introduce some key aspects of superconductivity and what happens when we include it in Kane-Mele model. We also show some properties when we add a magnetic impurity in the zigzag edge. We close this chapter with an introduction to the Majorana bound state and a sign that our system might host it.

### **Chapter 4**

In this chapter we first use a square lattice to test our code and see if the results are compatible with the bibliography. Then we show our main result for magnetic impurity chains, the existence of topological non-trivial phases and oscillations in the energy spectrum when the chain is in the zigzag edge. We also calculate the phase diagram for armchair edge.

### **Chapter 5**

In this chapter we present the conclusions of this work, the experimental implications related with the results of chapter 4. We end this chapter with a perspective of possible developments.

# Chapter 2

## Topological invariants for honeycomb lattice systems

In this chapter we will discuss the topic of topological invariants, focusing on Chern numbers and  $Z_2$  invariants and their relationship with topological insulators. Then we will review the Haldane model and its connection with the Integer Quantum Hall effect in a honeycomb lattice. We follow up by presenting the Kane-Mele model that can be thought as two copies of the Haldane model, one for each spin. This model will be central in this work as it will be used as basis for everything.

### 2.1 Topological Invariants

Topological invariants are quantities that are conserved under homeomorphisms, such that if two topological spaces have different topological invariants, then they are not homeomorphic with each other[16].

In other words, if we have a Hamiltonian such that varying one parameter will change a topological invariant, then a gap necessarily must be closed during these changes, such that the adiabatic theorem<sup>1</sup> won't hold. That is because changes under the adiabatic theorem are homeomorphisms.

The classical example of different topologies is a sphere and a torus. One has a hole the other doesn't, and we can't deform one in the other. If we deform the band structure of two insulators to one another, i.e. the adiabatic theorem holds, then we say they are

---

<sup>1</sup>The idea behind the adiabatic theorem is that the system will stay in the same eigenstate when varying a parameter slowly, given that there is a gap between this state and the other states.

topologically equivalent. If two insulators are topologically different, then to deform one at another, a topological phase transition must happen.

In Condensed Matter, the notion of topological order was used first to describe the Quantum Hall Effect (QHE). Although this system might not show a spontaneous symmetry breaking, some properties invariant to smooth deformations change only with a phase transition[17].

In this section we review two important topological invariants, the Chern number and  $Z_2$ , we also show the bulk-edge correspondence which is central to the study of topological insulators

### 2.1.1 Chern Number

The QHE Chern number is a topological invariant associated with the QHE, also known in this context as TKKN invariant due to Thouless, Kohmoto, Nightingale e den Nijs. It was shown[6] that the Integer Quantum Hall Effect has a conductivity equal to the Chern number multiplied by the factor  $e^2/h$ .

In a 1D system with a cyclic Hamiltonian,  $H(k,t)=H(k,t+T)$ , the Chern number can be seen as a pump that transports  $n_C$  electrons per cycle, therefore relating with a change in the polarization. We shall not prove some of the calculations as they are beyond the scope of this work but the derivation can be found in several texts, e.g. [18]. We can write the Chern number as:

$$n_c = \frac{1}{2\pi} \int_T F(k, t) dk dt, \quad (2.1)$$

Integrated over the Brillouin zone, with  $0 \leq t \leq T$  and  $F = \frac{1}{2}\epsilon_{ij}\hat{d} \cdot (\partial_i\hat{d} \times \partial_j\hat{d})$  the Berry curvature. In the next section 2.2.1 we use this topological invariant to calculate the Quantum Hall phase in Haldane's model.

Due to the bulk-edge correspondence, the existence of a topological invariant, that distinguishes our system from a usual insulator, implies the presence of edge states. Those are chiral states as they propagate in only one direction. Therefore, no backscattering due to impurities is expected.

This implies that we can relate the QHE Chern number with the number of times a edge state intersect the Fermi-level with a positive group velocity  $N_R$  and negative one

$N_L$ . We write:

$$N_R - N_L = \Delta N_c \quad (2.2)$$

with  $\Delta N_c$  the Chern number variation in the interface. This is a classical example of the bulk-boundary correspondence.

### 2.1.2 Kramers' Theorem

In a system invariant to time-reversal and an odd number of fermions we have at least two degenerate states. To show that we follow the proof given at [7].

Let  $|\psi\rangle$  be an eigenstate with energy E and  $\Theta$  the time-reversal operator. If it has TRS then  $[\Theta, H] = 0$ . Therefore,  $\Theta |\psi\rangle$  is also a eigenstate with energy E. Now let us show that both are orthogonal with each other. Using  $\Theta = UK$ , with  $K$  the conjugacy operator and  $U$  antisymmetric, we get

$$\langle \psi | \Theta | \psi \rangle = \sum_{m,n} \psi_m^* U_{mn} \psi_n^* = - \sum_{m,n} \psi_n^* U_{nm} \psi_m^* = - \langle \psi | \Theta | \psi \rangle = 0.s \quad (2.3)$$

So we have a degenerate state with energy E. To conclude we show that given n excitations moving to left we can calculate the probability for them to be scattered to the right. For one excitation we have:

$$\begin{aligned} \langle \Theta \psi | H | \psi \rangle &= \sum_{m,n,p} (U_{mp} K \psi_p)^* H_{mn} \psi_n = \sum_{m,n,p} U_{pm}^\dagger \psi_p H_{mn} \psi_n = \\ &= \sum_{m,n,p} U_{pm}^\dagger \psi_p (\Theta H \Theta^{-1})_{mn} \psi_n = - \sum_{m,n,p,q,r} \psi_p U_{pm}^\dagger U_{mr} H_{rq}^* U_{qn}^* \psi_n = \\ &= - \sum_{n,p,q} \psi_p H_{pq}^* U_{qn}^* \psi_n = - \sum_{m,n,p} U_{mp}^* \psi_p H_{mn} \psi_n = - \langle \Theta \psi | H | \psi \rangle, \end{aligned} \quad (2.4)$$

therefore, for n excitations the minus sign in Eq. 2.4 becomes  $(-1)^n$ . So if n is even then there is scattering with Kramers pairs, however if n is odd this process doesn't happen.

### 2.1.3 $Z_2$

Introduced by Kane and Mele in 2005[4], the topological invariant  $Z_2$  is used to describe systems with time-reversal symmetry (TRS), and similarly to Chern number and QHE, it is associated with Quantum Spin Hall Effect (QSHE). Since it depends upon spin, if a  $s_z$  symmetry is broken, due to Rashba for example, there won't be quantization in QSHE however the  $Z_2$  still exists, i.e. there will be a finite number of edge states and spin is no longer a good quantum number.

From the Krammers Theorem, any small perturbation that doesn't break TRS will not open a gap in the edge states. Because of this property, we can distinguish QSH states from those states of a common insulator. Now we will present some explicit calculations of the  $Z_2$  invariant[18].

We start with a n-band system with spin. For this case, the time-reversal operator is  $\Theta = i(I_n \otimes \sigma_y)K$ , with  $K$  the conjugacy operator,  $I_n$  the n-dimension identity matrix and  $\sigma_y$  the Pauli matrix. We say that our Hamiltonian has TRS if

$$H(-k) = \Theta H(k) \Theta^{-1} \quad (2.5)$$

There are points,  $\Gamma_i$ , in the Brillouin zone that are invariant under time reversal symmetry operation, i.e.  $-\Gamma_i = \Gamma_i + mG$ , with  $G$  being a vector in the reciprocal lattice, such that we have in those points  $H(-k) = H(k)$ . Because of Kramers theorem, there are double degeneracies in those points, which we call Kramers' pairs. Those pairs are protected by TRS. We shall denote them as n-I and n-II, with n indicating the band and I(II) the pair. These two bands are related by:

$$|u(-k)_{n-I}\rangle = -e^{i\chi_{k,n}} \Theta |u(k)_{n-II}\rangle, \quad (2.6)$$

$$|u(-k)_{n-II}\rangle = e^{i\chi_{k,n}} \Theta |u(k)_{n-I}\rangle. \quad (2.7)$$

The polarization associated with s (s=I or II) is given by:

$$P^s = \int_{Bz} \frac{A_k^s}{2\pi} dk, \quad (2.8)$$

with  $A_k^s = i \sum \langle u(k)_{n-s} | \nabla_k | u(k)_{n-s} \rangle$  invariant under phase change of  $|u(k)_{n-s}\rangle$ . Then we

can write  $P^I$  as

$$P^I = \int_0^\pi \frac{A_k^I}{2\pi} dk + \int_{-\pi}^0 \frac{A_k^I}{2\pi} dk, \quad (2.9)$$

$$P^I = \int_0^\pi \frac{A_k^I + A_{-k}^I}{2\pi} dk, \quad (2.10)$$

using the time-reversal operator

$$\langle \Theta u(k)_{n-II} | \nabla_k | \Theta u(k)_{n-II} \rangle = - \langle u(k)_{n-II} | \nabla_k | u(k)_{n-II} \rangle, \quad (2.11)$$

$$\langle \Theta u(k)_{n-II} | \nabla_k | \Theta u(k)_{n-II} \rangle = \langle e^{-\chi_{k,n}} u(k)_{n-I} | \nabla_k | e^{-\chi_{k,n}} u(k)_{n-II} \rangle, \quad (2.12)$$

$$A_k^I + \sum_n \frac{\partial \chi_{k,n}}{\partial k} = A_k^{II}. \quad (2.13)$$

substituting at  $P^I$  and using  $A_k = A_k^I + A_k^{II}$ ,

$$P^I = \int_0^\pi \frac{A_k}{2\pi} dk - \frac{1}{2\pi} \sum_n (\chi_{\pi,n} - \chi_{0,n}). \quad (2.14)$$

Let  $w(k)$  be:

$$w_{mn}(k) = \langle u_m(-k) | \Theta | u_n(k) \rangle, \quad (2.15)$$

with non-zero elements given by  $\langle u_{n-I}(-k) | \Theta | u_{n-II}(k) \rangle = -e^{-i\chi_{k,n}}$  and  $\langle u_{n-II}(-k) | \Theta | u_{n-I}(k) \rangle = e^{-i\chi_{k,n}}$ . For  $k=0$  and  $k=\pi$ , the matrix is anti-symmetry and unitary. We can use the Pfaffian to describe it (see Appendix A).

$$\frac{Pf[w(\pi)]}{Pf[w(0)]} = \exp \left[ i \sum_n (\chi_{\pi,n} - \chi_{0,n}) \right], \quad (2.16)$$

therefore polarization is given by

$$P^I = \frac{1}{2\pi} \left[ \int_0^\pi A_k dk + i \ln \left( \frac{Pf[w(\pi)]}{Pf[w(0)]} \right) \right]. \quad (2.17)$$

Due to TRS we have  $P^{II} = P^I \bmod \alpha$  with  $\alpha$  an integer. The polarization charge is  $P = P^I + P^{II}$  and we define the time-reversal polarization as  $P_\Theta = P^I - P^{II}$ .

$$P_\Theta = \frac{1}{2\pi} \left[ \int_0^{pi} A_k dk - \int_{-\pi}^0 A_k dk + 2i \ln \left( \frac{Pf[w(\pi)]}{Pf[w(0)]} \right) \right], \quad (2.18)$$

$$P_\Theta = \frac{1}{2\pi i} \left[ \int_0^{p^i} Tr[w^\dagger \nabla_k w] dk - 2 \ln\left(\frac{Pf[w(\pi)]}{Pf[w(0)]}\right) \right], \quad (2.19)$$

with  $Tr[w^\dagger \nabla_k w] = i \sum_n (\nabla_k \chi_{-k,n} - \nabla_k \chi_{k,n})$ . As  $w$  is unitary,

$$Tr[w^\dagger \nabla_k w] = Tr[\nabla_k \ln(w)] = \nabla_k \ln(\det[w]), \quad (2.20)$$

therefore,

$$P_\Theta = \frac{1}{2\pi i} \left[ \ln\left(\frac{\det[\pi]}{\det[0]}\right) - 2 \ln\left(\frac{Pf[w(\pi)]}{Pf[w(0)]}\right) \right], \quad (2.21)$$

or

$$(-1)^{P_\Theta} = \frac{\det[w(0)]^{1/2}}{Pf[w(0)]} \frac{\det[w(\pi)]^{1/2}}{Pf[w(\pi)]}. \quad (2.22)$$

For a cyclic process  $H(t+T)=H(t)$ , we obtain:

$$H(t*1 = 0) = \Theta H(0) \Theta^{-1}, \quad (2.23)$$

$$H(t*1 = T/2) = \Theta H(T/2) \Theta^{-1}. \quad (2.24)$$

The change in time-reversal polarization is Gauge invariant and define the  $Z_2$ ,  $\nu = P_\Theta(T/2) - P_\Theta(0) \bmod 2$ , or using the invariant point  $\Gamma_i$  with  $t*_i$  we have:

$$(-1)^\nu = \prod_i \frac{\sqrt{\det[w(\Gamma_i)]}}{Pf[w(\Gamma_i)]}, \quad (2.25)$$

since  $Pf(w)^2 = \det(w)$ ,  $\nu$  is either 0 (trivial) or 1 (non-trivial).

## 2.2 Honeycomb lattice models

### 2.2.1 Haldane Model

In 1988 Haldane proposed a spinless model in a honeycomb lattice with Integer Quantum Hall effect without Landau levels and with translational symmetry[19]. In this model, the Quantum Hall effect is the result of the time-reversal symmetry breaking by a space-varying magnetic flux, which when summed over the unitary cell, is null, as shown below:

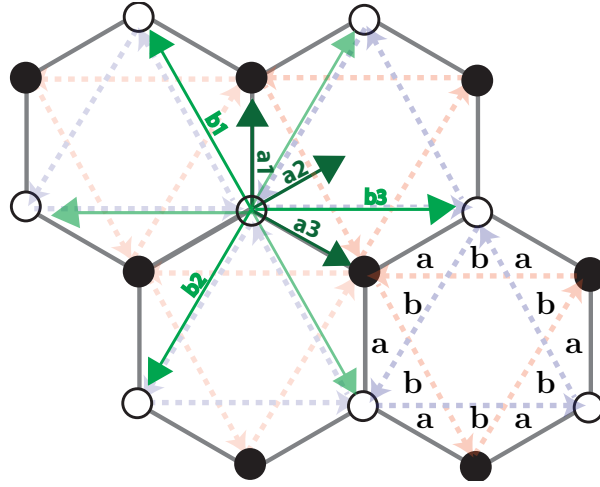


Figure 2.1: Haldane's model. Region a has flux  $\phi$  region b has flux  $-\phi$  in this way the total flux over the unitary cell is zero. Here we show some vectors that will be used latter. The dashed vectors indicate the direction considered for the phase in the hopping.

To achieve this, Haldane proposed the following toy-model Hamiltonian

$$H = t_1 \sum_{\langle i,j \rangle} c_i^\dagger c_j + t_2 \sum_{\langle\langle i,j \rangle\rangle} e^{i\phi_{ij}} c_i^\dagger c_j + M \sum_i \epsilon_i c_i^\dagger c_i \quad (2.26)$$

with  $\phi_{ij} = \pm\phi$  depending on the direction,  $t_1$  a first neighbor hopping and  $t_2$  a second neighbor hopping that has a similar effect as a spin-orbit coupling, and  $M$  a energy associated with each sublattice that have a weight  $\epsilon_i = \pm 1$  which depends on the sublattice. We will used that the Black (White) dots in figure 2.1 are sublattice A (B) with weight  $\epsilon_i=+1 (-1)$ [18].

Using  $(\mathbf{a}_1, \mathbf{a}_2, \mathbf{a}_3)$  as the vectors connecting first neighbors and  $(\mathbf{b}_1, \mathbf{b}_2, \mathbf{b}_3)$  the vector connecting the second neighbors as seen at Fig. 2.1. We can write in the basis  $(c_{k,A}^\dagger, c_{k,B}^\dagger)$

$$H(\mathbf{k}) = \epsilon(\mathbf{k})\mathbb{I} + \mathbf{d}(\mathbf{k}) \cdot \boldsymbol{\sigma}, \quad (2.27a)$$

$$\epsilon(\mathbf{k}) = \cos(\phi) \cos(\mathbf{k} \cdot \mathbf{b}_i), \quad (2.27b)$$

$$d_x(\mathbf{k}) = t_1 \sum_{i=1}^3 \cos(\mathbf{k} \cdot \mathbf{a}_i), \quad (2.27c)$$

$$d_y(\mathbf{k}) = t_1 \sum_{i=1}^3 \sin(\mathbf{k} \cdot \mathbf{a}_i), \quad (2.27d)$$

$$d_z(\mathbf{k}) = M - 2t_2 \sin(\phi) \sum_{i=1}^3 \sin(\mathbf{k} \cdot \mathbf{b}_i). \quad (2.27e)$$

Now we can diagonalize the Hamiltonian. We note that the two bands touch each other only at the points K and K' of the Brillouin zone (which also have an hexagonal form)<sup>2</sup>, and only if  $M=\pm 3\sqrt{3}t_2 \sin(\phi)$ . Thus, closing of bands at either K or K' depend only upon the sign of M.

For the case  $|t_2/t_1| < 1/3$ , which guarantees that the bands will not always intercept, we plot the two cases for M below. We can see that when the bands close in the K (K') point it doesn't close at K' (K) point.

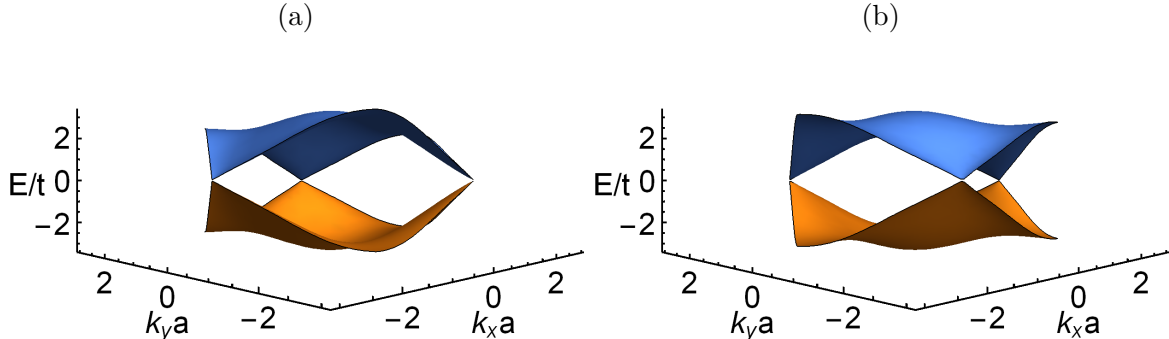


Figure 2.2: Energy bands with. (a)  $M=+3\sqrt{3}t_2 \sin(\phi)$  and (b)  $M=-3\sqrt{3}t_2 \sin(\phi)$ .

One of the similarities between this system and the Quantum Hall state, is that we can use a Chern number to calculate the Hall conductance, with the relation between Hall conductance and Chern number,  $\sigma_H = n_c \frac{e^2}{h}$ . The difference here is that this system can only have a Chern number  $\pm 1$  or zero. Differently from the QHE that can be any integer, as can be seen from calculating the Chern number for the Haldane model:

$$n_c = \frac{1}{2} [Sgn(M - 3\sqrt{3}t_2 \sin(\phi)) + Sgn(-M - 3\sqrt{3}t_2 \sin(\phi))]. \quad (2.28)$$

With Sgn the sign function. So we can make a phase diagram for Haldane model as

---

<sup>2</sup>The K and K' are the vertices of the hexagon. They arise from the sublattice XXX

function of  $\phi$  and  $M/t_2$ :

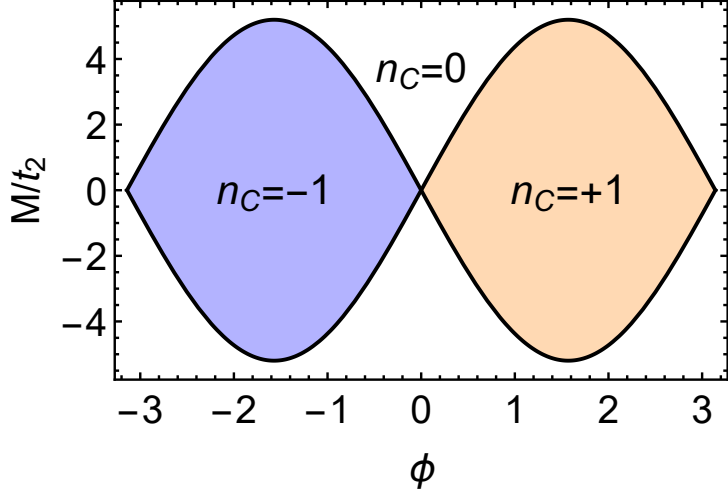


Figure 2.3: Phase diagram with the Chern number for Haldane model.

### 2.2.2 Kane-Mele model

The Kane-Mele model was introduced in 2005 as a way to describe a TRS-preserving system of electrons in a honeycomb lattice with spin-orbit interactions[1]. The idea was that graphene could be described with this model. Latter it was found that the spin-orbit coupling in pure graphene is too small to display the topological properties of the model. Still this model can be applied to other materials (silicene).

Differently from Haldane's model, now we have a spin orbit instead of a magnetic flux. In addition, since Kane-Mele model have TRS we will describe the topology with a  $Z_2$  invariant, instead of a Chern number. The final result is that we will have a Quantum Spin Hall phase instead of a Quantum Hall one.

The Kane-Mele Hamiltonian is given by the Hamiltonian

$$H = t \sum_{\langle i,j \rangle} c_i^\dagger c_j + i \frac{\lambda_{SO}}{3\sqrt{3}} \sum_{\langle\langle i,j \rangle\rangle} \nu_{ij} c_i^\dagger s_z c_j + i \frac{2\lambda_R}{3} \sum_{\langle i,j \rangle} c_i^\dagger (s \times \mathbf{d}_{ij})_z c_j + \lambda_v \sum_i \xi_i c_i^\dagger c_i, \quad (2.29)$$

where  $t$  the hopping term,  $\lambda_{so}$  the spin-orbit coupling,  $\nu_{i,j} = (\mathbf{d}_i \times \mathbf{d}_j)_z = \pm 1$  with  $\mathbf{d}_{i,j}$  the unitary vectors that connects site  $i$  with site  $j$ .  $\lambda_r$  is the Rashba term and  $\lambda_v$  is an onsite energy (staggering potential) with a weight  $\xi_i = \pm 1$  that depends from the sublattice. Here we used a slightly different notation compared to Kane and Mele so the bulk gap equation becomes more symmetric.

## Infinite systems

As we saw before, we can study the bulk to get some properties of the edges by virtue of the bulk-edge correspondence. Because of this, we start with the Hamiltonian for the Kane-Mele model in 2D, and we calculate the  $Z_2$ . In this case, our Hamiltonian will be a 4x4 matrix.

Using the Dirac matrices  $\Gamma^i = (\sigma_x \otimes \mathbb{I}, \sigma_z \otimes \mathbb{I}, \sigma_y \otimes s_x, \sigma_y \otimes s_y, \sigma_y \otimes s_z)$ ,  $\sigma$  the Pauli matrices associated with the sublattice and  $s$  the Pauli matrices associated with spin. Let  $\Gamma^{ij} = \frac{1}{2i} [\Gamma^i, \Gamma^j]$ . We can write our Hamiltonian as[18]

$$\mathcal{H} = \sum_{i=1}^5 d_i \Gamma^i + \sum_{i < j}^5 d_{ij} \Gamma^{ij} \quad (2.30)$$

In this basis we have

$$d_1 = t(1 + 2 \cos[\frac{k_x}{2}] \cos[\frac{\sqrt{3}k_y}{2}]), \quad (2.31a)$$

$$d_2 = \lambda_v, \quad (2.31b)$$

$$d_3 = \frac{2\lambda_R}{3}(1 - \cos[\frac{k_x}{2}] \cos[\frac{\sqrt{3}k_y}{2}]), \quad (2.31c)$$

$$d_4 = -\frac{2\sqrt{3}\lambda_R}{3} \sin[\frac{k_x}{2}] \sin[\frac{\sqrt{3}k_y}{2}], \quad (2.31d)$$

$$d_{12} = -2t \cos[\frac{k_x}{2}] \sin[\frac{\sqrt{3}k_y}{2}], \quad (2.31e)$$

$$d_{15} = \frac{\lambda_{SO}}{3\sqrt{3}}(2 \sin[k_x] - 4 \sin[\frac{k_x}{2}] \cos[\frac{\sqrt{3}k_y}{2}]), \quad (2.31f)$$

$$d_{23} = -\frac{2\lambda_R}{3} \cos[\frac{k_x}{2}] \sin[\frac{\sqrt{3}k_y}{2}], \quad (2.31g)$$

$$d_{24} = \frac{2\sqrt{3}\lambda_R}{3} \sin[\frac{k_x}{2}] \cos[\frac{\sqrt{3}k_y}{2}]. \quad (2.31h)$$

For  $\lambda_R = 0$  the Hamiltonian is block diagonal with respect to spin and the gap is given by  $2|\lambda_{so} - \lambda_v|$ . When the gap closes, the topological phase changes, so we need to know what phase we are in  $\lambda_{so} > \lambda_v$  to determine all phases. In this case, we can separate the Hamiltonian and calculate the Chern number for each part.

Although the sum of the parts is zero  $n_C = n_\uparrow + n_\downarrow = 0$ , if we subtract them  $n_{C,s} = n_\uparrow - n_\downarrow = 2$ . This indicates the existence of propagating spins in different directions consistent with Quantum Spill Hall effect. We could also calculate the spectrum and see the existence of edge states in a quasi-1D system as we will be doing below.

For  $\lambda_R \neq 0$ ,  $s_z$  is no longer a good quantum number and the system mixes the spins (we

can't separate in two Hamiltonians). In this case we observe that small perturbations at the  $\lambda_R$  doesn't close the bulk gap, and so it doesn't affect the edge-states.

We can calculate the bulk-gap with a continuum version of the Kane-Mele Hamiltonian:

$$\mathcal{H} = i\hbar v_F (\sigma_x \tau_z \partial_x + \sigma_y \partial_y) + \lambda_{SO} \sigma_z \tau_z s_z + \lambda_R (\sigma_x \tau_z s_y - \sigma_y s_x + \lambda_v \sigma_z) \quad (2.32)$$

from this equation we can calculate the band gap and with this we can have a phase diagram:

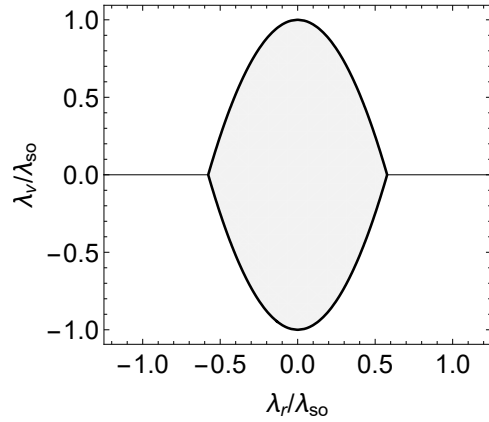


Figure 2.4: Phase diagram for Kane-Mele model. The gray area in the middle is the topological non-trivial phase. This is valid for  $\lambda_{SO} \ll t$ .

### Quasi-1D systems

We can now study the Kane-Mele model for a Quasi-1D system. Due to symmetries of the honeycomb lattice, we have two different edges. These geometric differences have effect in the properties of the edges[20].

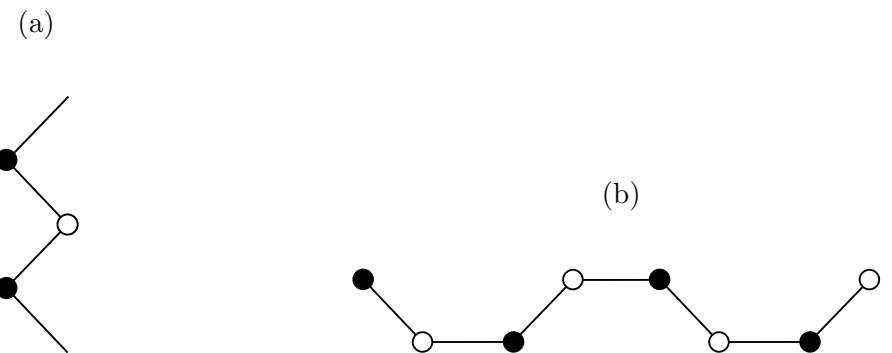


Figure 2.5: Honeycomb edges.(a) Zigzag edge and (b) armchair edge.

In this work, we will focus in the zigzag-edge. The derivation for the matrix of Kane-Mele Hamiltonian can be seen in appendix B. We now consider a system with n-strips as shown below

and we calculate the band structure for two cases, the first a topological non-trivial that we can see the edge states crossing the Fermi-level, and the second which is a normal insulator.

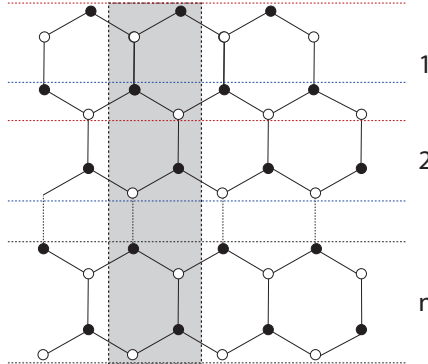


Figure 2.6: Hexagonal structure, with sublattice A (black dot,  $\xi = 1$ ) and B (white dot,  $\xi = -1$ ). The figure shows the choice of numbering the strips. In gray is the choice of basis for the tight-biding.

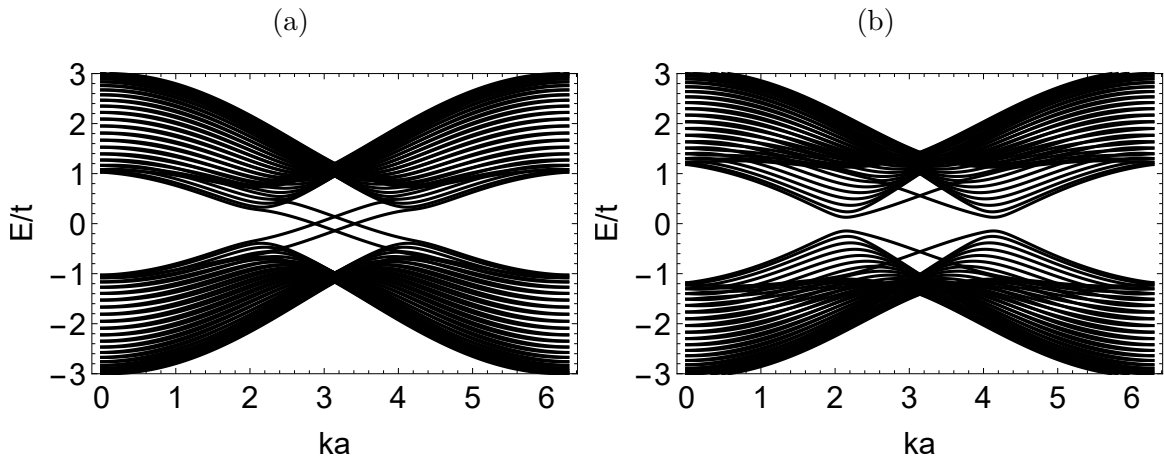


Figure 2.7: Energy bands for a 20-strips. The values used for calculations were  $\lambda_{SO} = 0.5t$ ,  $\lambda_R = 0.08t$  (a)  $\lambda_v = 0.15t$  and (b)  $\lambda_v = 0.6t$ . We can see in the first plot the edge states that cross the fermi energy while in the second plot is a normal insulator.

Now we can calculate the gap for finite sized strips. We expect that small number of strips might change open a gap (the edge states interact with each other) while  $N_{\text{strips}} \gg 1$  should be 0 for  $\lambda_v < \lambda_{SO}$  because of the edge states and  $2|\lambda_{so} - \lambda_v|$  when  $\lambda_v > \lambda_{SO}$ .

From the Fig. 2.6 we see that this indeed happens. This is important when considering applications for graphene, silicene (although the former have an almost zero spin-orbit), and also when considering effects that depend of the gap, for example superconductivity order parameter that may take place only when the edges crosses de bulk gap.

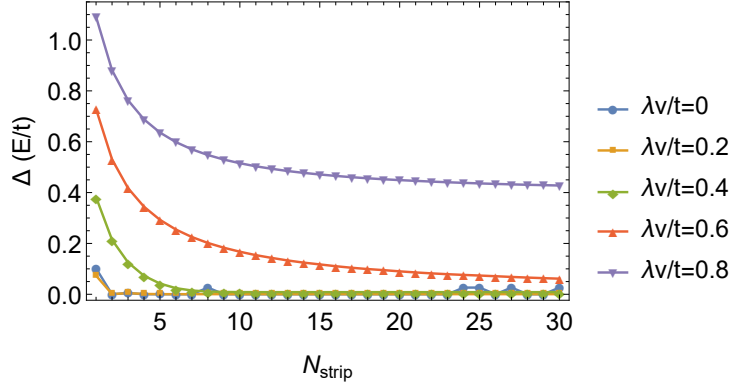


Figure 2.8: Plot of gap  $\Delta$  in units of  $E/t$  by the number of strips ( $N_{\text{strips}}$ ), for multiples  $\lambda_v$ . For this calculation we used  $\lambda_{so}/t = 0.6$

We also note that for  $\lambda_v = 0$ , the parity of the strips will affect the gap until  $N_{\text{Strip}} \approx 5$ . With even strips implying a zero gap while for odd strips we have a small non-zero gap[21]

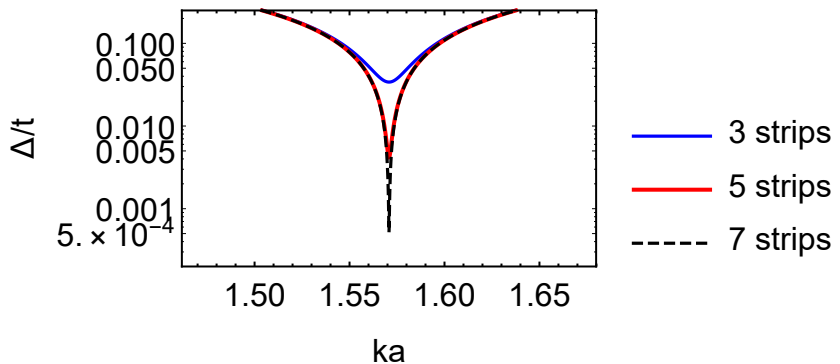


Figure 2.9: Plot of gap  $\Delta$  in units of  $E/t$  for 3 different number of strips ( $N_{\text{strips}}$ ).

We now plot the gap for the quasi-1D with 1 to 6 strips, the existence of edge states can be identified when the gap is zero. Fig 2.10, shows density plots of the gap for different sizes of systems. From the figure below is clear that up to 6 strips the gap might resemble a little of the infinite model, but have more differences, as it is in the range of the decay of the gap (see fig 2.8).

We saw how the gap depends with the number of strips, and up to 10 strips the edges effects are too large to ignore. These effects are interesting not only for applications (opening gap), but also in the theoretical framework when one needs to consider edge states in finite samples that have differences with the bulk model.

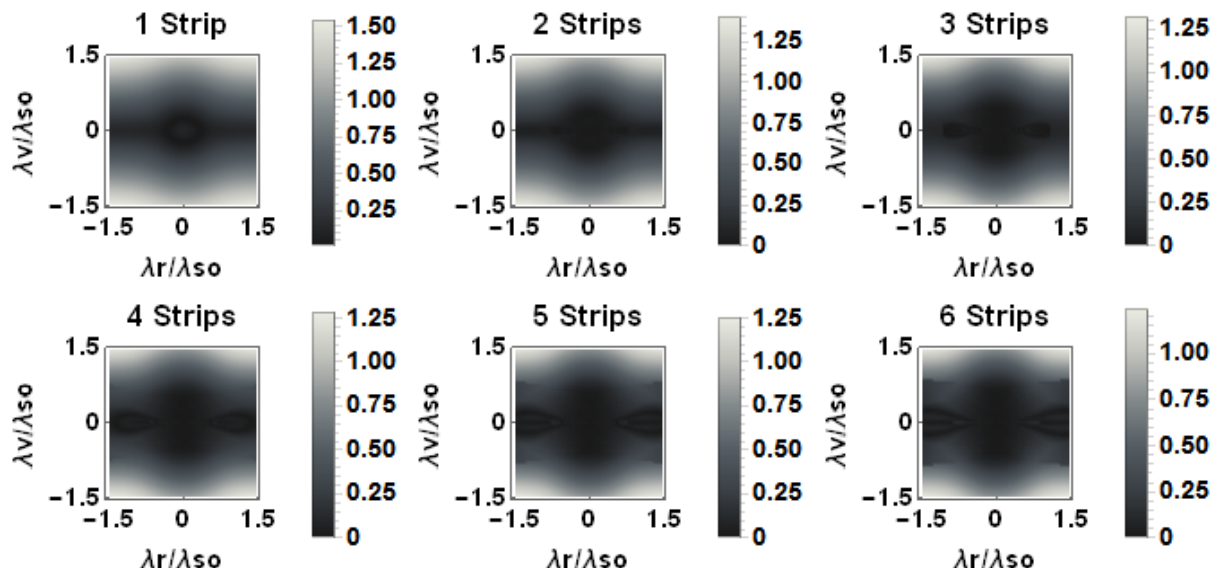


Figure 2.10: Density plot of gap  $\Delta$  in units of  $E/t$  for different number of strips, when changing the parameters  $\lambda_r$  and  $\lambda_v$ . To produce those plots, it was used  $\lambda_{so} = 0.6$ . We can compare this figures with figure 2.4 and we see that the gap going to zero is different from the quasi-1D with small number of strips and the bulk version.

# Chapter 3

## Superconductivity and Impurities

In this chapter, we will discuss the basics of superconductivity using the Bardeen, Cooper and Schrieffer theory together with mean-field in a self-consistent way. Then we proceed to study superconductivity in the Kane-Mele model. We add a magnetic impurity in the zigzag edge and we study its effects on the system.

### 3.1 Superconductivity

#### 3.1.1 Introduction to superconductivity

In this work, we will be considering a conventional s-wave superconductor. From the Bardeen, Cooper and Schrieffer theory (BCS), the superconductivity arise from Cooper pairs that are made from two electrons coupled with a attractive force. The BCS Hamiltonian can be written as[22]:

$$\mathcal{H}_{BCS} = t \sum_{\langle i,j \rangle, \sigma} c_{i,\sigma}^\dagger c_{j,\sigma} + U c_\uparrow^\dagger c_\downarrow^\dagger c_\uparrow c_\downarrow, \quad (3.1)$$

where  $-U <0$  is the effective (attractive) electron-electron interaction or the pair strength. To solve this Hamiltonian we use mean-field theory in which we rewrite it as

$$\mathcal{H}_{MF} = \Delta c_\uparrow c_\downarrow + H.C, \quad (3.2)$$

with  $\Delta_i = -U_i \langle c_{i,j\downarrow}, c_{i,j\uparrow} \rangle$  the superconducting order parameter (SOP). From this point we have two possibilities, first we can compute  $\Delta$  in a self-consistently way (i.e. we start with a first guess and then we compute until it converges) or we can fix a value.

### 3.1.2 The self-consistency method

For the mean-field condition, we have[23, 24]

$$\Delta_i = -U_i < c_{i\downarrow}, c_{i\uparrow} >, \quad (3.3)$$

$$\Delta_i = -\frac{U_i}{2} [< c_{i\downarrow}, c_{i\uparrow} > - < c_{i\uparrow}, c_{i\downarrow} >], \quad (3.4)$$

$$\Delta_i = -\frac{U_i}{2N_k} \sum_{k,k'} e^{i(k+k')R} [< c_{i,k\downarrow}, c_{i,k'\uparrow} > - < c_{i,k\uparrow}, c_{i,k'\downarrow} >], \quad (3.5)$$

$$\Delta_i = -\frac{U_i}{2N_k} \sum_k [< c_{i,-k\downarrow}, c_{i,k\uparrow} > - < c_{i,-k\uparrow}, c_{i,k\downarrow} >]. \quad (3.6)$$

Now we consider the Bogoliubov transformation that diagonalizes the Hamiltonian. In the basis  $\mathbf{B} = (c_{i,\uparrow}, \dots, c_{N,\uparrow}, c_{i,\downarrow}, \dots, c_{N,\downarrow}, c_{i,\uparrow}^\dagger, \dots, c_{N,\uparrow}^\dagger, c_{i,\downarrow}^\dagger, \dots, c_{N,\downarrow}^\dagger)^T$

$$c_{i,\sigma} = \sum_{E_n > 0}^n (u_{i,\sigma}^n \gamma_n - \sigma v_{i,\sigma}^{n*} \gamma_n^\dagger) \quad c_{i,\sigma}^\dagger = \sum_{E_n > 0}^n (u_{i,\sigma}^{n*} \gamma_n^\dagger - \sigma v_{i,\sigma}^n \gamma_n), \quad (3.7)$$

in which the sum is only over the half of eigenvalues (non-negatives). Above  $\gamma_n$  is the creation operator of a quasi-particle with energy  $E_n$ , with  $u_{i,\sigma}^n$  being the value of the eigenvector associated with  $E_n$  in the position  $c_{i\sigma}$  of basis  $\mathbf{B}$ , and  $v_{i,\sigma}^n$  is associated with the position  $c_{i\sigma}^\dagger$  of basis  $\mathbf{B}$ . Notice that  $\gamma$  satisfies the following anti-commutation relations:

$$\{\gamma_i, \gamma_j^\dagger\} = \delta_{i,j}, \quad \{\gamma_i, \gamma_j\} = \{\gamma_i^\dagger, \gamma_j^\dagger\} = 0. \quad (3.8)$$

It is also possible to show that the BdG Hamiltonian has a pair of eigenvalues  $E$  and  $-E$  and if  $(\mathbf{u}, \mathbf{v})$  is the eigenvector with energy  $E$ , then  $(-\mathbf{v}^*, \mathbf{u}^*)$  is also an eigenvector but with eigenvalue  $-E$ .

Now we can now calculate  $\Delta_i$  from Eq (3.6), using  $< \gamma_i^\dagger \gamma_j > = \delta_{i,j} f(E_i)$ , where  $f(E) = \frac{1}{1+e^{\beta E}}$ , is the Fermi-Dirac distribution, and

$$< c_{i,-k\downarrow}, c_{i,k\uparrow} > = \sum_{m,n} (v_{i,k,\downarrow}^{m*} u_{i,k,\uparrow}^n) < \gamma_m^\dagger \gamma_n > = \sum_n (v_{i,k,\downarrow}^{n*} u_{i,k,\uparrow}^n) f(E_n), \quad (3.9)$$

$$< c_{i,-k\uparrow}, c_{i,k\downarrow} > = \sum_n (v_{i,k,\uparrow}^{n*} u_{i,k,\downarrow}^n) f(E_n). \quad (3.10)$$

Therefore, we have

$$\Delta_i = -\frac{U_i}{2N_k} \sum_{k,n} (v_{i,k,\downarrow}^{n*} u_{i,k,\uparrow}^n - v_{i,k,\uparrow}^{n*} u_{i,k,\downarrow}^n) f(E_n). \quad (3.11)$$

If we want to compute  $\Delta$  in real space, we have a similar expression

$$\Delta_i = -\frac{U_i}{2} \sum_n (v_{i,\downarrow}^{n*} u_{i,\uparrow}^n - v_{i,\uparrow}^{n*} u_{i,\downarrow}^n) f(E_n). \quad (3.12)$$

If we choose the iteration error as being the absolute value of the difference between two successive  $\Delta$ , then after some iterations the error become exponentially decreasing with the number of iterations, as can be seen from figure below:

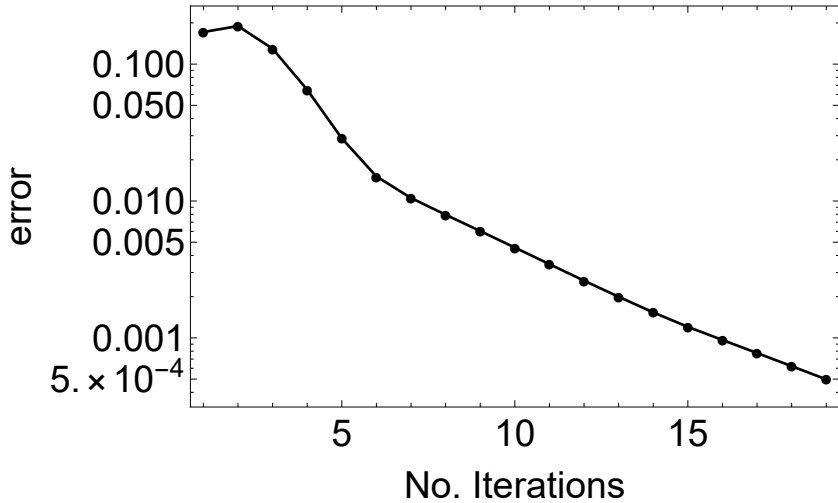


Figure 3.1: Numerical error given by absolute value of the difference between two successive  $\Delta$  over the number of iterations.

### 3.1.3 The free-energy

The free-energy is an important concept when we want to study which phase is stable and when we have phase transitions. Through this work we will use it to study both cases.

We start with the differential form of the free energy and make a Legendre transformation to Landau potential

$$dF = -SdT - PdV + \mu dN, \quad (3.13)$$

$$\Omega = F - \mu N, \quad (3.14)$$

$$d\Omega = -SdT - PdV - Nd\mu, \quad (3.15)$$

Now for a fix T and V, we have

$$N = -\left(\frac{\partial \Omega}{\partial \mu}\right)_{(T,V)}, \quad (3.16)$$

but for a fixed energy and state, we have

$$n_\epsilon = f(\epsilon) = \frac{1}{e^{\frac{\epsilon-\mu}{k_b T}} + 1} = - \left( \frac{\partial \Omega}{\partial \mu} \right)_{(T,V)}, \quad (3.17)$$

$$\Omega_\epsilon = -k_b T \ln \left( 1 + e^{-\frac{\epsilon-\mu}{k_b T}} \right) + \varphi_{(T,V)} \quad (3.18)$$

$$\Omega = -\frac{k_b T}{2} \sum_n \ln \left( 1 + e^{-\beta E_n^{BdG}} \right) - E_0, \quad (3.19)$$

with  $E_0 = -\sum_i \frac{|\Delta_i|^2}{U_i}$ , being the constant term neglected when calculating the mean-field approximation for  $H_{int} = -\sum_i U_i n_{i\uparrow} n_{i\downarrow}$ , and the half is because we are considering the energies associated with both electron and hole. Doing the same for the normal,  $\Delta = 0$ , case we have:

$$\Omega_N = -\frac{k_b T}{2} \sum_n \ln \left( 1 + e^{-\beta E_n^N} \right). \quad (3.20)$$

Taking the difference between both cases:

$$\Omega_{SC} - \Omega_N = -\frac{k_b T}{2} \sum_n \left[ \ln \left( 1 + e^{-\beta E_n^{BdG}} \right) - \ln \left( 1 + e^{-\beta E_n^N} \right) \right] + \sum_i \frac{|\Delta_i|^2}{U_i} \quad (3.21)$$

### 3.1.4 The superconductivity for electrons on a honeycomb lattice

The Kane-Mele model, discussed in Sec. 2.2.2, is an interesting basis for induced superconductivity, not only because it is a topological insulator and we induce superconductivity mainly at the metallic states. Even though this superconductivity is due a proximity with a superconductor, Cooper pairs will flow to our system and will make the honeycomb system behave like a s-wave superconductor[25]. But also because of its lattice geometry, we can expect different results as compared to a square lattice, for instance.

Therefore as a first step we have to probe the SOP both at the edge and in the middle of the sample for different parameters of our system<sup>1</sup>. In order to do that, we use a system with 400-atoms that can be seen in Fig. 3.2.

---

<sup>1</sup>In the following figures, unless we are probing the parameter, it should be fixed at  $\lambda_{SO} = 0.5t$ ,  $U=2t$  and  $\lambda_v = \mu = \lambda_R = 0$ .

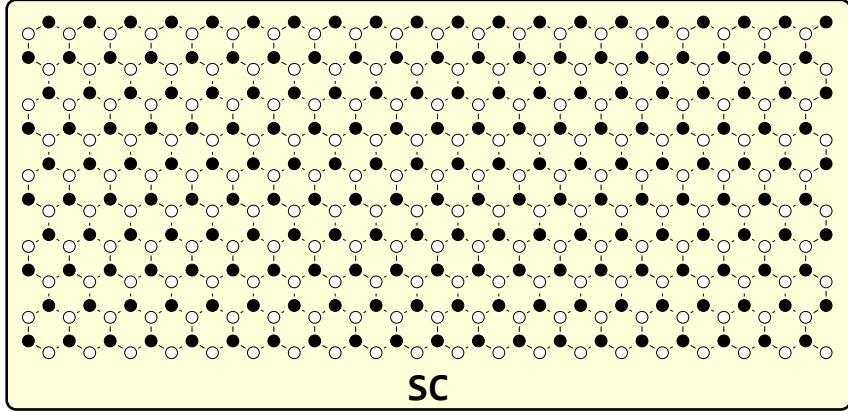


Figure 3.2: The system considered with 400-atoms over a superconductor which leads to an induced superconductivity.

The doping  $\mu$  is important, as some results[5] show that it is necessary for superconductivity. Fig. 3.3 below shows how doping affects the SOP. We note that for  $\mu \leq 0.5t$ ,  $\Delta$  is almost constant and significant at the edges, increasing  $\mu$  induces superconductivity also in the bulk, as expected because changing increasing doping the Fermi level will lie in the bands of the bulk instead of only of the edges.

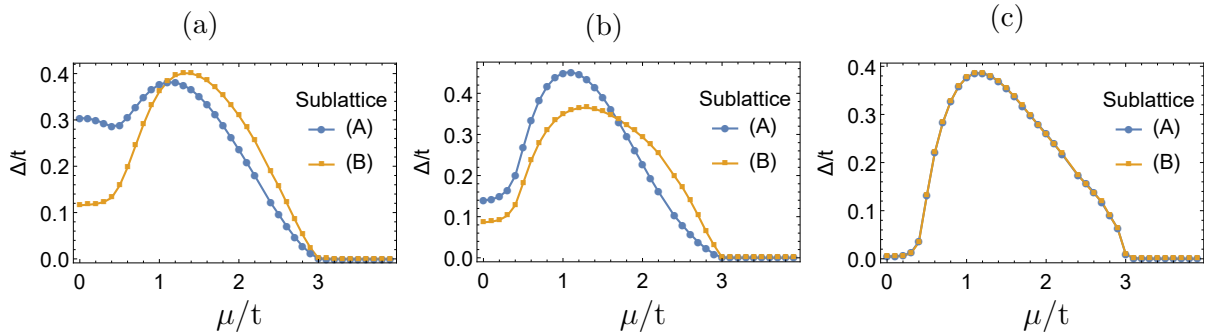


Figure 3.3: Doping ( $\mu$ ) effect on superconductivity order parameter at different positions for sublattice A and B. (a) Zigzag edge. (b) Armchair edge. (c) Middle of the sample.

Fig. 3.4 shows that, when we increase the staggering potential parameter we expect that for  $\lambda_v \rightarrow 0.5t$  the system will undergo a topological phase transition and will lose the metallic edge states. Indeed this happens, although not at  $0.5t$  but at  $0.6t$  due finite size effects. We also note that the SOP increases in the bulk but is still very small in relation to the SOP at the edges.

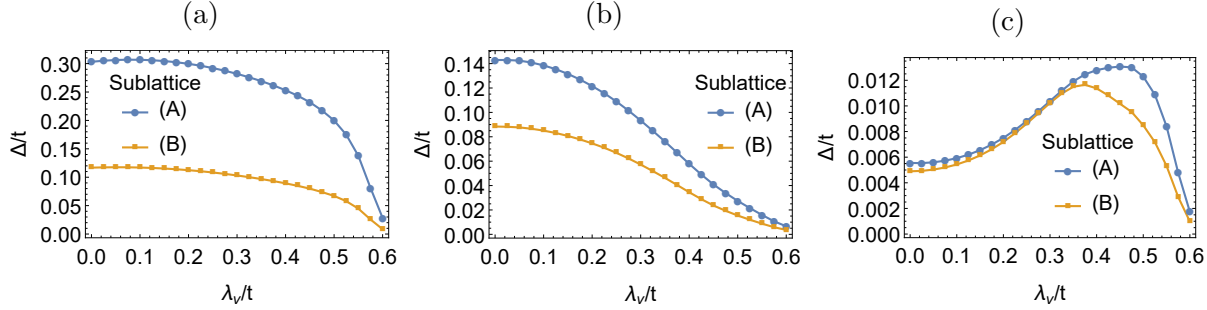


Figure 3.4: Staggering potential ( $\lambda_v$ ) effect on superconductivity order parameter at different positions for sublattice A and B. (a) Zigzag edge. (b) Armchair edge. (c) Middle of the sample.

Fig. 3.5 shows that, Rashba spin-orbit coupling has a noticeable effect at the armchair edge, however in the zigzag this effect is not as clear probably due to geometry effects. The Rashba coupling also increases  $\Delta$  at the bulk. We don't observe decrease at any edge even when  $\lambda_R > 0.5t$  because we have  $\lambda_v = 0$  and the metallic edge still exist.

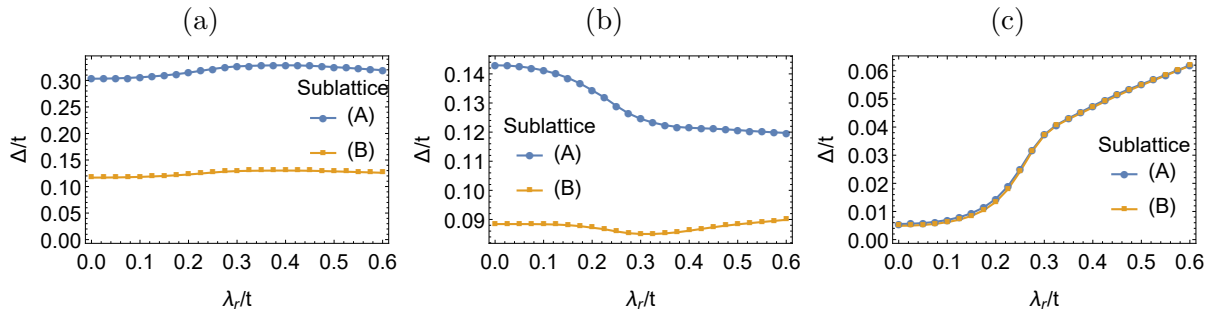


Figure 3.5: Rashba spin-orbit ( $\lambda_r$ ) effect on superconductivity order parameter at different positions for sublattice A and B. (a) Zigzag edge. (b) Armchair edge. (c) Middle of the sample.

We end this section with Fig. 3.6, when we increase  $U$  we also increase  $\Delta$ , as expected. The important point here is that if we increase too much the pair potential we also induce superconductivity in the bulk. So, if we want just the edges to be superconducting we must have  $U \leq 2t$ .

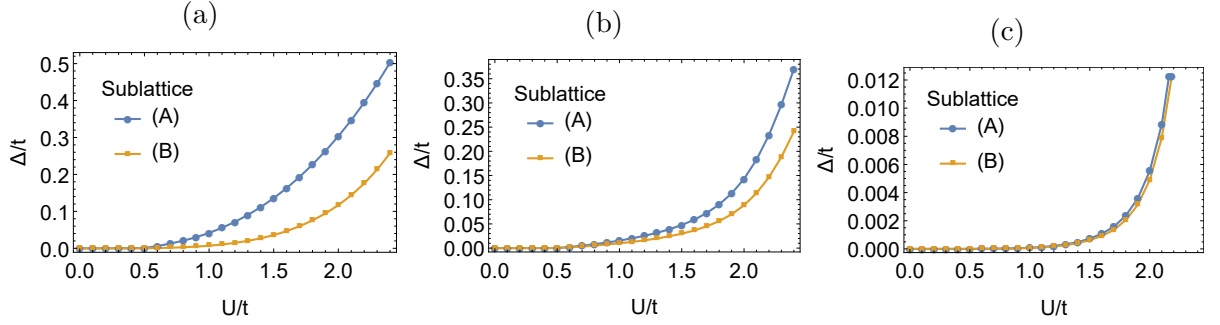


Figure 3.6: Pair attraction potential( $U$ ) effect on superconductivity order parameter at different positions for sublattice A and B. (a) Zigzag edge. (b) Armchair edge. (c) Middle of the sample.

## 3.2 Impurities

For this work we will consider localized impurities, that works as classical spins and don't interact with their neighbors. This can be written as

$$\mathcal{H}_{Imp} = \sum_{i \in \mathcal{I}} \left[ \tilde{V} c_i^\dagger c_i + V_z c_i^\dagger (\hat{n}_i \cdot \mathbf{s}) c_i \right], \quad (3.22)$$

where  $\tilde{V}$  and  $V_z$  are local non-magnetic and magnetic scattering potentials at the impurities sites  $i \in \mathcal{I}$ .  $\hat{n}_i$  is the magnetic moment direction associated with the impurity and  $\mathbf{s}$  is the Pauli matrices related to spin.  $V_z$  works as a Zeeman splitting field that plays a fundamental role in the search for Majorana bound states.

This simple model is enough to provide us with an interesting physics. Due to the distances between impurities we would not expect a large direct exchange term between them to be relevant. Such terms would also introduce new technical complications that are to be avoided in this first approach. We now apply this model and obtain some important results that will be used latter.

### 3.2.1 A single impurity in the superconducting Kane-Mele model

In order to have a general idea of the effects of a single impurity in the energy levels of the sample, we plot in Fig. 3.7 the energy spectrum dependence with the scattering potential strength( $V_z$ ). We place the impurity at the middle of zigzag-edge at the most external atom.

Fig. 3.7 shows four plots one for each kind of impurity, non-magnetic and magnetic in the x, y or z direction. It is possible to see that only the magnetic impurity cases show energy levels

inside the superconductivity gap, i.e.  $E < 0.19t$ . This is due to the Anderson Theorem<sup>2</sup>. There is also a distinction between magnetic impurities in the  $x$  or  $y$  direction and the  $z$  direction. The former are similar and cross the zero energy for a critical  $V_z$ , as can be seen clearer from fig.3.8.

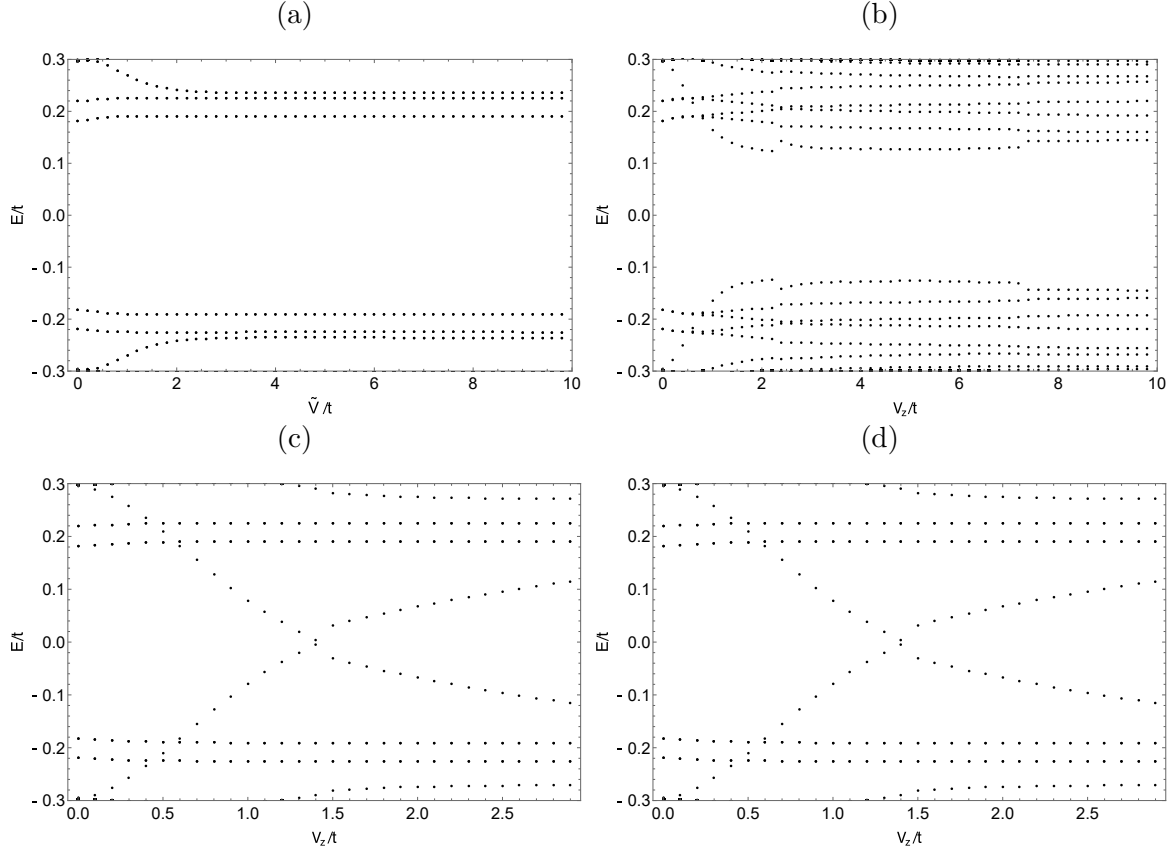


Figure 3.7: Dependence of the energy with the strength of the impurity scattering for (a) nonmagnetic scattering, (b) magnetic in  $\vec{z}$  direction, (c) magnetic in  $\vec{x}$  direction, (d) magnetic in  $\vec{y}$  direction

Because of the existence of a zero-energy mode for a  $V_z$  critical in the  $x$  or  $y$  direction, we will be studying this system only when  $V_z$  is in the  $xy$ -plane. In this case, when we increase  $\lambda_v$  there will always be a  $V_z$  critical above which there is a zero energy state. However, for  $\lambda_v < \lambda_{so}$  we can see that this zero mode is followed by a jump when we increase  $V_z$  even a little, while for  $\lambda_v > \lambda_{so}$  there is no discontinuity, as can be seen below. This shows that there are difference between an impurity in the superconductivity case<sup>3</sup>  $\lambda_v < \lambda_{so}$ , and in the normal case  $\lambda_v > \lambda_{so}$ , as can be seen in Fig. 3.8

<sup>2</sup>XXX

<sup>3</sup>This is the requirement for topological non-trivial case in Kane-Mele model and therefore the existence of a metallic edge that will host superconductivity.

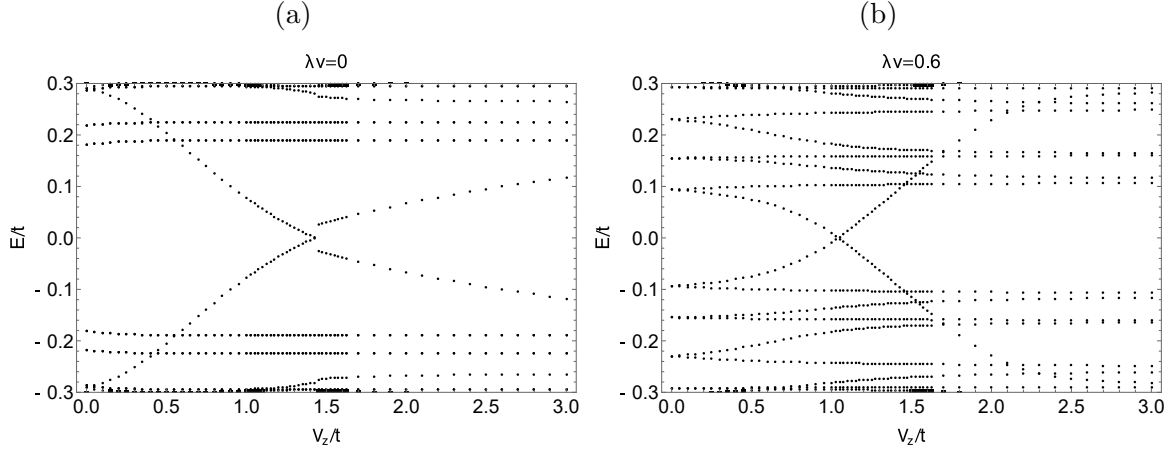


Figure 3.8: Detailed dependence of the energy with the strength of the impurity scattering for magnetic in  $\vec{x}$  direction. (a) In the superconductivity regime,  $\lambda_v = 0$ . (b) In the normal regime,  $\lambda_v = 0.6t$ . We can see a difference in the value of  $V_z$  in which exists a zero energy state.

In the superconducting state, the  $V_z$  critical represents more than just a discontinuity in the energy levels as Fig. 3.9 shows. The order parameter in the impurity position has also a jump in its absolute value and have a  $\pi$ -phase change, as have been seen in other systems [26].

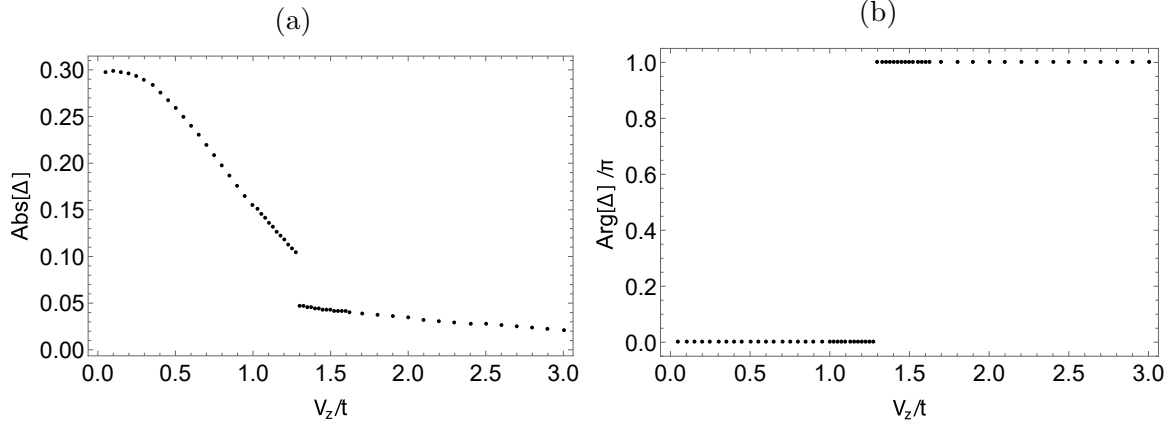


Figure 3.9: Superconductivity order parameter  $\Delta$  at the impurity, at left the absolute value and at right the phase. We can see a transition at  $V_z = 1.3$ .

This suggests that there might be a phase transition in this case. From previous studies we expect this to be a phase transition[27]. We see this transition from the difference between the free-energy of the superconductivity state with the normal state, fig.3.10.

When computing the difference of free-energy, we found that around  $V_z$  critical we have a metastable state that depends whether we start with small  $V_z$  and increase it or with a large  $V_z$  and decrease it. To solve this problem, we mixed both cases choosing the one that produces the smallest difference in the free-energy.

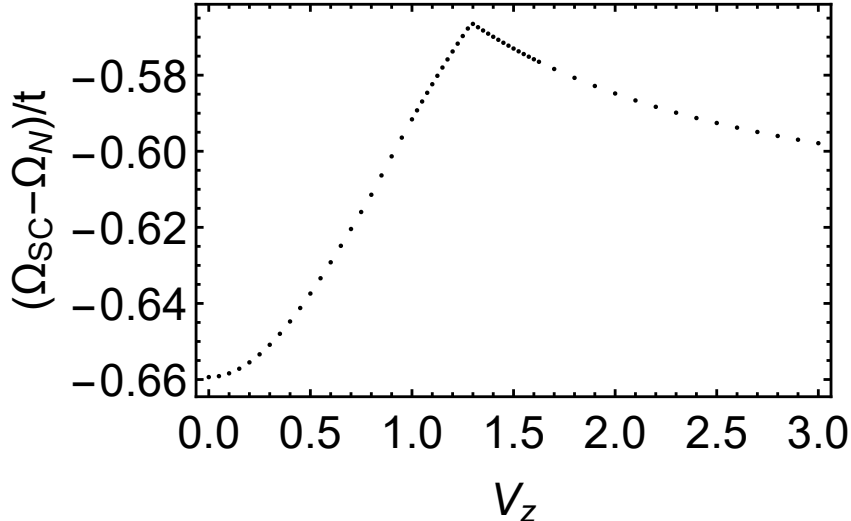


Figure 3.10: Difference of the free-energy from superconductivity state and normal state for  $\lambda_v = 0$ .

## Magnetization

The onsite magnetization from the sample is given generically by

$$\vec{m}_i = \left\langle \left( c_{\uparrow,i}^\dagger, c_{\downarrow,i}^\dagger \right) \vec{s} (c_{\uparrow,i}, c_{\downarrow,i})^T \right\rangle, \quad (3.23)$$

where  $\vec{s}$  is a Pauli matrix vector associated with spin. In terms of its components, the magnetization is given by

$$m_{x,i} = \langle s_x \rangle_i = \frac{\hbar}{2} \left( \left\langle c_{\uparrow,i}^\dagger c_{\downarrow,i} \right\rangle + \left\langle c_{\downarrow,i}^\dagger c_{\uparrow,i} \right\rangle \right), \quad (3.24a)$$

$$m_{y,i} = \langle s_y \rangle_i = \frac{\hbar}{2i} \left( \left\langle c_{\uparrow,i}^\dagger c_{\downarrow,i} \right\rangle - \left\langle c_{\downarrow,i}^\dagger c_{\uparrow,i} \right\rangle \right), \quad (3.24b)$$

$$m_{z,i} = \langle s_z \rangle_i = \frac{\hbar}{2} \left( \left\langle c_{\uparrow,i}^\dagger c_{\uparrow,i} \right\rangle - \left\langle c_{\downarrow,i}^\dagger c_{\downarrow,i} \right\rangle \right). \quad (3.24c)$$

Using the same procedure to calculate  $\Delta$  as in the previous section, we find that

$$m_{x,i} = \sum_\nu \frac{\hbar}{2} (u^{*\nu}_{i,\uparrow} u^\nu_{i,\downarrow} + u^\nu_{i,\uparrow} u^{*\nu}_{i,\downarrow}) = \sum_\nu \hbar \text{Re} [u^{*\nu}_{i,\uparrow} u^\nu_{i,\downarrow}], \quad (3.25a)$$

$$m_{y,i} = \sum_\nu \frac{\hbar}{2i} (u^{*\nu}_{i,\uparrow} u^\nu_{i,\downarrow} - u^\nu_{i,\uparrow} u^{*\nu}_{i,\downarrow}) = \sum_\nu \hbar \text{Im} [u^{*\nu}_{i,\uparrow} u^\nu_{i,\downarrow}], \quad (3.25b)$$

$$m_{z,i} = \sum_\nu \frac{\hbar}{2} (|u^\nu_{i,\uparrow}|^2 - |u^\nu_{i,\downarrow}|^2) = \sum_\nu \hbar (|u^\nu_{i,\uparrow}|^2 - |u^\nu_{i,\downarrow}|^2). \quad (3.25c)$$

We use this formalism to calculate the magnetization of one impurity at the zig-zag edge with magnetic moment aligned to the x-direction. First we notice that the magnetization in the z-direction is zero. As expected since a simple strip should not have any magnetization nor the impurity should have any effect due to symmetry in the z-direction<sup>4</sup>.

Some results are shown in Fig. 3.11, where we calculate the magnetization for different  $\lambda_v$  in the x and y-direction. For any staggering potential there will be a magnetization in the impurity site anti-parallel to  $V_z$  and for the nearest neighbors in the edge, same sublattice, will also be anti-parallel in the superconductivity case. This sites will also have a small perpendicular magnetization in relation with  $V_z$  with the sign depending on the value of  $\lambda_v$ .

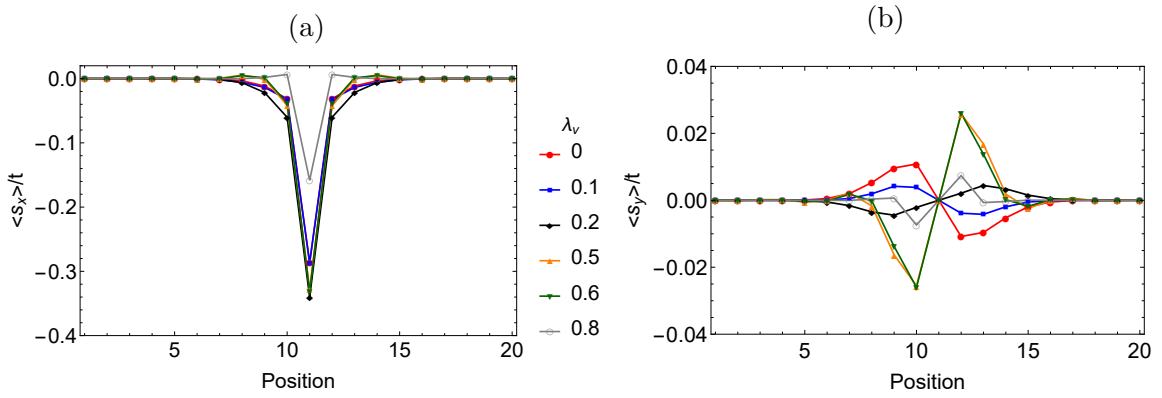


Figure 3.11: Magnetization of the system with  $V_z=1.4t$  for many  $\lambda_v$ , in the direction (a) parallel to  $V_z$ , (b) perpendicular to  $V_z$ . The position axis represents the number of the site at the zigzag edge. The impurity is in position 11.

<sup>4</sup>Changing spin  $\uparrow \rightarrow \downarrow$  doesn't affect the system



# Chapter 4

## Majorana bound states

In this chapter, we will review Majorana bound states its properties, protected zero-modes and non-Abelian statistics, and we show models for 1D chain and how to realize it. We also show how the topological properties arise in those models.

### 4.1 Introduction

In 1937 Ettore Majorana introduced the idea of Majorana fermion, a particle that it is its own antiparticle. It originated in the context of high energy physics, when Dirac's equation was split in two real wave equations, therefore producing a particle that is its antiparticle<sup>1</sup>[14], in which Majorana argued that a neutrino should have this property, a fact yet to be seen.

Although initially used to describe fundamental particles, Majorana fermions can be described as quasi-particles in the context of condensed matter physics, and we will call it Majorana bound states. Since the only fundamental particles in solids are ions and electrons, Majorana bound states can be seen as emergent excitation like phonons, magnons, plasmons. The fact that a Majorana fermion is its own antiparticle suggests that, in condensed matter, it will emerge from an electron and a hole.

This implies that superconductors are a natural place for this kind of excitation, as the cooper-pair condensation creates a superposition of electrons and holes. However, in general the superconductivity will arise from s-wave superconductor with different spins, and this would break the symmetry for particle and antiparticle. In fact, one of the first models showing Majorana bound states, the Kitaev chain with a SOP displaying p-wave symmetry, is spinless[3]. We

---

<sup>1</sup>In Dirac's equation, electron and positron are related by a symmetry operation that takes the complex conjugate of the wave function, therefore if an electron had a real wave function it would be equal to a positron.

will see after how strong spin-orbit coupling can make this model reasonable. But for now, let's define this introduction in terms of second quantization.

We can perform a change of basis from the usual creation and annihilation operator  $c^\dagger, c$  to a "Majorana basis",

$$c_j = \frac{1}{2}(\gamma_{j,1} + i\gamma_{j,2}), \quad c_j^\dagger = \frac{1}{2}(\gamma_{j,1} - i\gamma_{j,2}), \quad (4.1)$$

with  $\gamma_{j,k}$ ,  $k=1$  or  $2$ , the Majora fermion operator, that satisfies:

$$\{\gamma_{i,k}, \gamma_{j,k'}\} = 2\delta_{i,j}\delta_{k,k'} \quad \gamma_{i,k}^\dagger = \gamma_{i,k}. \quad (4.2)$$

This mathematical formulation is very interesting, since it tell us that a Majorana bound state is some sort of half electron and half hole. This procedure can always be done and most of the times doesn't bring any new information about the system, even though  $\gamma_{i,k}$  do have different properties from electrons, e.g. protected zero-modes and non-abelian statistics.

#### 4.1.1 Protected zero-modes

Let us consider a superconductor using Bogoliubov-de Gennes (BdG) formalism. Defining  $H_0(r)$  as the normal state Hamiltonian, i.e. without the superconducting interaction, and  $\Delta(r) = V < c_{\uparrow r} c_{\downarrow r} >$  the superconducting order parameter. Then the BdG Hamiltonian will be:

$$H_{BdG} = \begin{pmatrix} H_0(r) & \Delta(r) \\ \Delta^\dagger(r) & -\sigma_y H_0^*(r)\sigma_y \end{pmatrix}, \quad (4.3)$$

where  $\sigma_y$  is the Pauli y matrix, with the basis vector, the Nambu spinor

$$\Psi(r) = \begin{pmatrix} c_{\uparrow r} \\ c_{\downarrow r} \\ c_{\downarrow r}^\dagger \\ -c_{\uparrow r}^\dagger \end{pmatrix} \quad (4.4)$$

We notice that the Nambu spinor satisfies the Majorana requirement, i.e. the charge conjugation of the spinor is equal to the spinor.

$$C\Psi^*(r) = \Psi(r), \quad (4.5)$$

with  $C = \tau^y \sigma^y$ , the charge conjugacy and  $\tau^y$  the y Pauli matrix. This follows directly from the relation between the components of the spinor, and implies that Majorana bound states are related with superconductors[28].

Now suppose we have a single state with energy 0, separated from other states by a gap, we have then:

$$H_{BdG}(r)\Phi_0(r) = 0. \quad (4.6)$$

From equations 4.4 and 4.5 it is easy to show that a creation operator  $\hat{\gamma}$  that created this state have the following property  $\hat{\gamma}^\dagger(r) = \hat{\gamma}(r)$ , that means  $\hat{\gamma}$  is a Majorana bound state operator which creates or destroys a state of zero energy, in other words, a Majorana zero mode (MZM).

This zero energy modes are quite different from an electron, for example, as they need no energy to be created, which implies that the ground state of the system is degenerated.

It is also topologically protected, in a way that is impossible to change this state by continuous deformation of the band structure, without closing the gap. If it were to happen and this state become a new one with energy E, then by equation 4.5 it would be necessary to have also a new state with -E.

### 4.1.2 Non-Abelian statistics

An interesting property of systems of MZMs is that they might not respect the usual fermionic statistics, i.e. when exchange two particles the wavefunction is multiplied by -1, or for a general Abelian-anyon is multiplied by a phase factor  $e^{i\phi}$ [29].

One important ingredient for this to happen is the degenerate ground state separated from other states by a gap, such that adiabatic operations can change one ground state to another. This fact is extremely important for quantum computation. We know show how this can happen in a 1D system with 2 electrons (4 Majorana bound states). Although not rigorously, this treatment[30] is one of the simplest to understand.

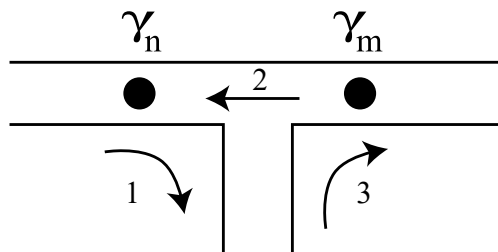


Figure 4.1: Exchange of Majorana zero modes.

We are swapping two MZMs as the above figure, so they don't come together and become a normal electron. Doing this procedure such that at the end we have  $\mathcal{H}_i = \mathcal{H}_f$ . So we want to find a unitary matrix  $U$ , with dimensions  $2^N \times 2^N$ ,  $N$  the total number of Majorana, that transform our Hamiltonian and our states when we swap the MZMs.

We want this operator  $U$  to satisfy:

- $U$  must depend only on the swapped Majorana  $\gamma_n$  and  $\gamma_m$ .
- The total electron parity should not change, the total number of electrons can change due to superconductivity but always in pairs.
- Must be unitary.

The first two items are satisfied by  $i\beta\gamma_n\gamma_m$ , for some real number  $\beta$ . We can make an hermitian operator  $X$  unitary with  $\text{Exp}[iX]$ [30]. So to satisfy it we have

$$U = \exp [\beta\gamma_n\gamma_m] = \cos [\beta] + \gamma_n\gamma_m \sin [\beta], \quad (4.7)$$

where we used the fact that  $(\gamma_n\gamma_m)^2 = -1$ . Now in we can use the Heisenberg picture to evolve our operator  $\gamma_n$  and  $\gamma_m$ .

$$U\gamma_n U^\dagger = \cos [2\beta] \gamma_n - \sin [2\beta] \gamma_m, \quad (4.8)$$

so it is clear if we want  $\gamma_n \rightarrow \gamma_m$  we need  $\beta = \pm\pi/4$ , and  $U = (1 \pm \gamma_n\gamma_m)/\sqrt{2}$ . We can now work on a concrete example with 2 electrons.

Let  $c_1^\dagger = 1/2(\gamma_1 + i\gamma_2)$  and  $c_2^\dagger = 1/2(\gamma_3 + i\gamma_4)$ , consider our base  $\{|11\rangle, |00\rangle, |10\rangle, |01\rangle\}$ , with 1 when there is an electron and 0 when there is a hole. This can be viewed in the picture below:

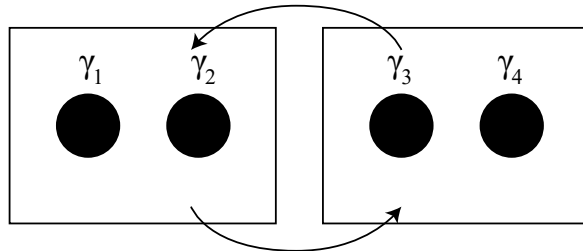


Figure 4.2: Exchange of two Majorana bound states in a two electron system.

Now let us change  $\gamma_2$  with  $\gamma_3$ . In our basis we write the operator  $U$  as

$$U = \frac{1}{\sqrt{2}} \begin{pmatrix} 1 & -i & 0 & 0 \\ -i & 1 & 0 & 0 \\ 0 & 0 & 1 & -i \\ 0 & 0 & -i & 1 \end{pmatrix},$$

so if we start in the state  $|00\rangle$  after swapping the Majorana bound states we end up in the superposition  $(|00\rangle - i|11\rangle)/\sqrt{2}$ , different from fermions or bosons that continues in the same state.

## 4.2 Realizing Majorana bound states in 1D chain

In this subsection we shall review 1D systems that may host Majorana bound states. In special, we will see the Kitaev chain in more detail as it is the simplest model and illustrate most of the ideas so far.

### 4.2.1 The Kitaev chain

The Kitaev chain was introduced in 2001 as a simple model for a 1D spinless p-wave superconductor[12]. Although it was originally a toy model, it was realized latter that it could explain systems with spin-orbit coupling in a Zeeman field as this system behaves like a spinless one[28]. Now consider a Hamiltonian of N electrons in a 1D chain, with a hopping term  $t$ , a nearest-neighbor pairing amplitude  $\Delta$ , and a chemical potential  $\mu$ .

$$\mathcal{H} = -\mu \sum_{i=1}^N n_i - \sum_{i=1}^{N-1} (t c_i^\dagger c_{i+1} + \Delta c_i c_{i+1} + H.C), \quad (4.9)$$

where H.C. means Hermitian conjugate. Using Eq. 4.1, we can rewrite the Hamiltonian in terms of Majorana operators as

$$\mathcal{H} = \frac{1}{2} \left\{ -\mu \sum_{j=1}^N (1 + i\gamma_{j,1}\gamma_{j,2}) + \sum_{j=1}^{N-1} [(t + \Delta)i\gamma_{j,2}\gamma_{j+1,1} + (-t + \Delta)i\gamma_{j,1}\gamma_{j+1,2}] \right\}. \quad (4.10)$$

For simplicity, we will always consider  $\Delta$  real, and we shall study two cases  $\mu \neq 0$ ,  $t = \Delta = 0$  and  $\mu = 0$ ,  $t = \Delta \neq 0$ . The first case maps into a simple model of non interacting electrons, and we have

$$\mathcal{H} = -\frac{\mu}{2} \sum_{j=1}^N (1 + i\gamma_{j,1}\gamma_{j,2}) = -\mu \sum_{i=1}^N n_i, \quad (4.11)$$

this can be thought in terms of Fig. 4.3. Indeed, in this case the Majorana picture doesn't bring

much information other than how the Majorana bound states might be arranged. It is also easy to see that the ground state will be when all sites are occupied (for  $\mu > 0$ ) or empty (for  $\mu < 0$ ), and is topological trivial, as it is not related to the superconducting phase.

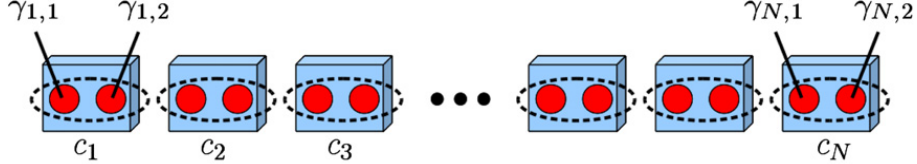


Figure 4.3: Adapted from [29]. Kitaev chain for the case  $\mu \neq 0$ ,  $t = \Delta = 0$ , in which Majorana bound states interact with others in the same site.

For the second case we have the following Hamiltonian

$$\mathcal{H} = -it \sum_{j=1}^{N-1} \gamma_{j,2} \gamma_{j+1,1}, \quad (4.12)$$

if we think of a new fermion state  $\tilde{c}_j = (\gamma_{j+1,1} + i\gamma_{j,2})/2$ , i.e the Majorana bound state interacts with the next site to form an electron as in Fig. 4.4, then we can rethink this Hamiltonian as

$$\mathcal{H} = 2t \sum_{j=1}^{N-1} \tilde{c}_j^\dagger \tilde{c}_j. \quad (4.13)$$

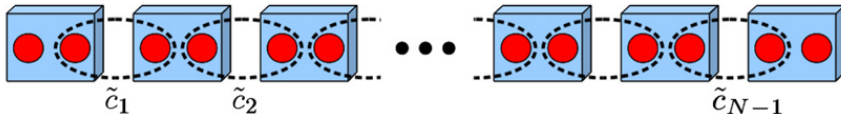


Figure 4.4: Adapted from [29]. Kitaev chain for the case  $\mu = 0$ ,  $t = \Delta \neq 0$ , we have that Majorana bound states interact with others in the next site

This is quite remarkable, since the Majorana states at the end of the wire are uncoupled by the Hamiltonian. We can create a highly non-local fermion state  $\tilde{c}_M = (\gamma_{N,2} + i\gamma_{1,1})$  that is completely decoupled, i.e we need zero energy to create or destroy this state.

If we now consider the system with periodic boundary conditions in momentum space, is possible to show that the system is gapless at  $|2t| = |\mu|$ . This two lines separate two different topological states, as we can see in the figure below.

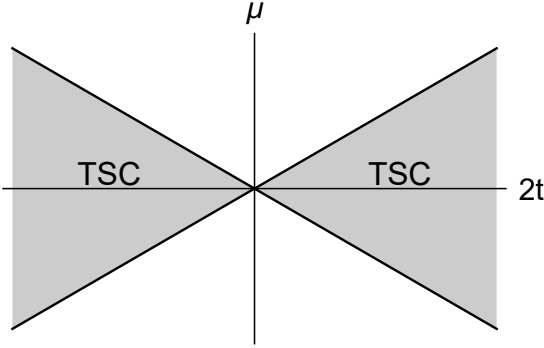


Figure 4.5: Illustration of the two phases in Kitaev model, topological trivial (white) and topological superconductor (shaded).

The difference between this two phases is the presence or absence of MZM at the end of the chain. In the case of  $\mu \neq 0$  in the shaded region, the Majorana bound states at the end of the wire leak inside[29]. It is also possible to distinguish this two phases through a topological invariant. In this case Kitaev showed that exist

$$\mathcal{M} = Sgn[Pf(H)] = \pm 1, \quad (4.14)$$

with  $\mathcal{M} = -1$  indicating a gapped system with unpaired MZM, i.e. the topological superconducting phase. The Pfaffian counts the degeneracy of the ground state that can only change when the gap goes to zero.

To calculate  $\mathcal{M}$ , we should remember that the Hamiltonian must be written in a basis where it is an antisymmetric matrix. This can be done using a unitary transformation to the Majorana basis described above, with  $\mathcal{H}_{as} = U\mathcal{H}U^\dagger$  and

$$U = \begin{pmatrix} 1 & 1 \\ i & -i \end{pmatrix} \otimes \mathbb{I}_{N \times N}, \quad (4.15)$$

in which we assumed the basis used in section 3.1.2, and  $\mathbb{I}_{N \times N}$  is the identity matrix with dimension N.

Since the Pfaffian changes only when we have a zero-energy crossing, and in k-space due to particle-hole symmetry (for every  $E(k)$  we have also  $-E(-k)$ ), the only points that are important to compute the Pfaffian is at  $k=0$  and  $k=\pi$ , any other point  $k'$  the change in Pfaffian will cancel with the change from  $-k'$ . Therefore we have:

$$\mathcal{M} = Sgn[Pf(\mathcal{H}(0))]Sgn[Pf(\mathcal{H}(\pi))], \quad (4.16)$$

### 4.2.2 Physical realization - Semiconductor wire

Some materials under specific conditions will behave like a spinless system and may be described by Kitaev's model. We shall explore in detail one of these systems, a semiconductor wire over a superconductor material[3, 29]. However, the reader should be aware that other systems exist, like the edges of 2D topological insulators, nanowires made from 3D topological insulators and Helical spin chains, that we will not discuss.

The semiconductor wire with strong spin-orbit coupling is one of the most important examples and is realized in materials like InSb or InAs[3]. Its importance come from the experimental knowledge that already exists with this kind of material, and also because some of experimental results for Majorana bound states come from those materials. We can have a simple Hamiltonian for low energy electrons with Rashba spin-orbit for the wire in the  $y$  direction

$$H = \frac{\hbar^2 k^2}{2m_{eff}} + \alpha \sigma^x k - \mu + V \sigma^z, \quad (4.17)$$

with  $m_{eff}$  the electron effective mass,  $\alpha$  the strength of the spin-orbit  $\mu$  the chemical potential and  $V$  a magnetic field in the  $z$  direction. This leads energy to be comprised by two shifted parabolas, i.e. the spin-orbit separates the energy by spin, as can be seen if Fig. 4.6 b. However, for  $V=0$  it always has an even number of Dirac points at right half of the Brillouin zone.

A Magnetic field with strength  $V \neq 0$  in the  $z$  direction, will separate the bands, Fig. 4.6a the blue and red parabola for  $V=0$  and the two black curves for  $V \neq 0$ . With this as long as  $|\mu| < V$  we will have only one Fermi point, and with the discussion in subsection 4.2.1 when we have a superconducting order parameter  $\Delta \neq 0$ , we will have Majorana bound state at the end of the wire[3].

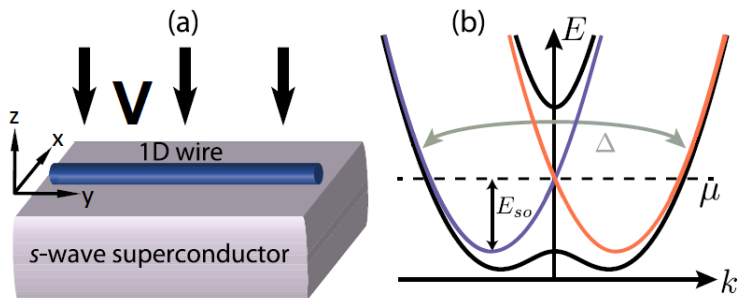


Figure 4.6: Adapted from [3]. (a) Structure required to have stable topological phase in a 1D wire with spin-orbit. (b) Band structure for the wire with time-reversal symmetry, bands blue and red due to spin-orbit, and when its broken, black band. When the chemical potential is inside the gap at  $k=0$ , the wire can be viewed as spinless.

For this discussion we considered  $|\Delta| \ll 1$ . However, when  $|\Delta|$  is bigger, one should be

more careful. Adding a p-wave superconducting term in the Hamiltonian, would lead that a gap would vanish for  $V = \sqrt{\mu^2 + |\Delta|^2}$ , in other words we would have the following phase diagram[3]:

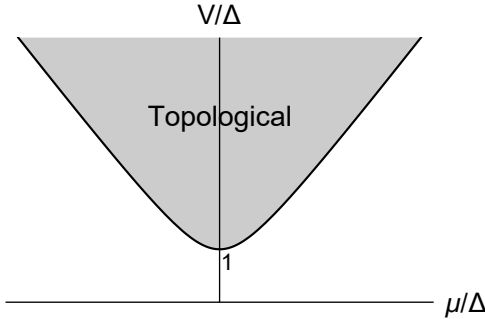


Figure 4.7: Phase diagram for the semiconducting wire.

One should notice that this is a simplified model, and for experiments it might be harder, as we not considered any kind of disorder, or any value necessary to attain the topological phase.



# Chapter 5

## Majorana states in the superconducting Kane-Mele model

### 5.1 Preliminary results

We can now think about the system we have been building so far - the superconducting Kane-Mele model with magnetic impurities. We have a s-wave pairing that opens a superconducting gap  $\Delta$ . Then we set through  $\mu$  a density of electrons in our sample. We separate our spins with  $\lambda_{so}$  so effectively we have a spinless system. To this end, we break spin conservation in the z-direction with  $V_z$  in xy-plane so we have no problem hosting a particle that is its own antiparticle, as we can't have a define spin.

With this we have all necessary elements to host a Majorana bound state. A first sign that this system might host Majorana is presented below. A zero-energy state, located at the edges of a 10-impurity chain in the zigzag-edge with  $\mu = 0.1t$  at zero-temperature and  $\lambda_{so} = 0.5t$ ,  $\lambda_v = \lambda_r = 0$  and  $U=2$  t.

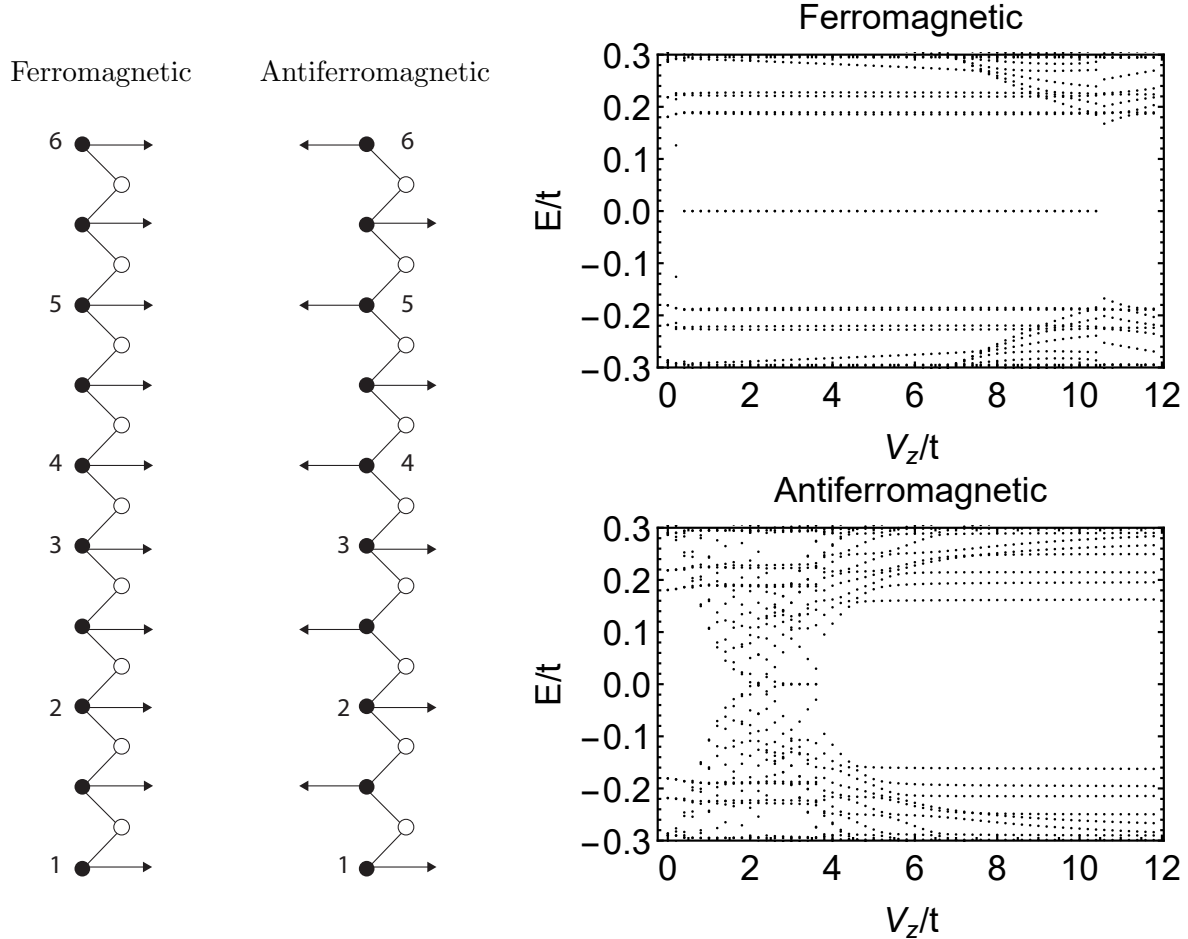


Figure 5.1: Impurity chain diagrams and the energy levels for both the ferromagnetic and antiferromagnetic cases. Some impurities were labeled from 1 to 6.

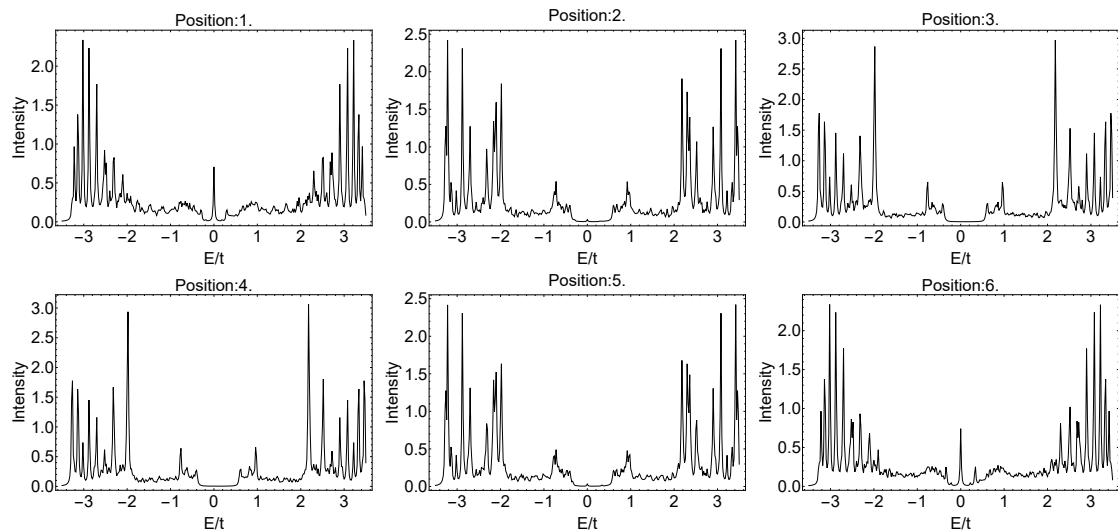


Figure 5.2: LDOS for the ferromagnetic case, in the impurities labeled as fig.5.1.

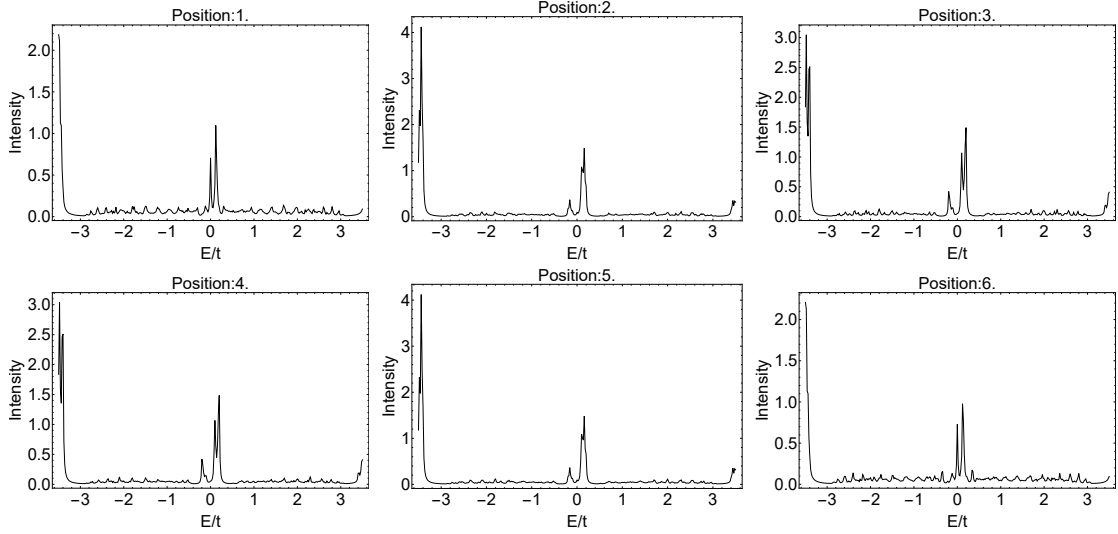


Figure 5.3: LDOS for the antiferromagnetic case, in the impurities labeled as fig.5.1.

In the next sections, we will explore how these edge states and their topological nature behave as a function of the parameters (through the computation of  $\text{Pf}(\mathcal{H})$ ).

## 5.2 Square lattice

Before we proceed to other results, it is worth to check if our functions to calculate the Pfaffian and SOP were rightly implemented. To this end, we will use a square lattice system that have already been studied in previous work[31].

In this system, we are interested in studying a chain of magnetic adatoms on the surface of a square lattice with s-wave superconductivity. We also use periodic boundary conditions (PBCs) in both directions.

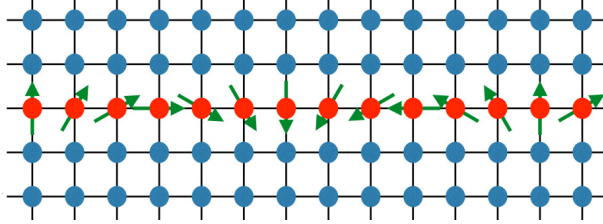


Figure 5.4: Figure from [31]. The sample considered, red circles with arrow indicate the impurity with its magnetic moment.

The Hamiltonian used to describe this model is

$$\begin{aligned} \mathcal{H}_0 = & - \sum_{\langle i,j \rangle, \sigma} t c_{i\sigma}^\dagger c_{j\sigma} - \mu \sum_{i,\sigma} c_{i\sigma}^\dagger c_{i\sigma} + V_z \sum_{i \in \mathcal{I}} \mathbf{S}_i \cdot (c_{i\sigma}^\dagger \boldsymbol{\sigma}_{\sigma\sigma'} c_{i\sigma'}) \\ & + \sum_j \left( \Delta_j c_{j\uparrow}^\dagger c_{j\downarrow}^\dagger + \text{H.c.} - \frac{1}{V} |\Delta_j|^2 \right), \end{aligned} \quad (5.1)$$

with  $t$  being the usual hopping,  $\mu$  the doping,  $V_z$  the impurities' magnetic moment,  $\mathbf{S}$  the direction of this moment,  $\sigma$  the Pauli matrices, and  $\Delta_j = U \langle c_{j\uparrow} c_{j\downarrow} \rangle$  the superconducting order parameter. Here, we restrict  $\mathbf{S}_j$  to be a coplanar spiral at wave vector  $\mathbf{G}$  such that:

$$\mathbf{S}_j = (\cos[Gx_j], -\sin[Gx_j], 0)$$

Performing a spin-dependent gauge transformation, we can eliminate the dependence of the magnetic moments with position which allows us to work in the reciprocal space.

$$c_{j\uparrow} \rightarrow c_{j\uparrow} e^{\frac{i}{2}Gx_j} \quad c_{j\downarrow} \rightarrow c_{j\downarrow} e^{-\frac{i}{2}Gx_j},$$

with this we go to the reference frame which all impurities magnetic momentum are aligned in the x-direction and the Hamiltonian becomes

$$\begin{aligned} \mathcal{H}_0 = & - \sum_{\langle i,j \rangle, \sigma} t e^{-\frac{i}{2}\sigma G(x_i-x_j)} c_{i\sigma}^\dagger c_{j\sigma} - \mu \sum_{i,\sigma} c_{i\sigma}^\dagger c_{i\sigma} + V_z \sum_{i \in \mathcal{I}} \cdot (c_{i\sigma}^\dagger \sigma_{\sigma\sigma'}^x c_{i\sigma'}) \\ & + \sum_j \left( \Delta_j c_{j\uparrow}^\dagger c_{j\downarrow}^\dagger + \text{H.c.} - \frac{1}{V} |\Delta_j|^2 \right), \end{aligned} \quad (5.2)$$

now the hoping acquires a spin-dependent phase that effectively works as a spin-orbit coupling and the magnetic moments become a uniform Zeeman field. With this, we can easily perform a Fourier transformation.

If we have  $N_y$  sites in the y direction, the Hamiltonian is a  $4N_y \times 4N_y$  matrix in which we use a similar basis as before  $(c_{i,\uparrow,k}, \dots, c_{N_y,\uparrow,k}, c_{i,\downarrow,k}, \dots, c_{N_y,\downarrow,k}, c_{i,\uparrow,k}^\dagger, \dots, c_{N_y,\uparrow,k}^\dagger, c_{i,\downarrow,k}^\dagger, \dots, c_{N_y,\downarrow,k}^\dagger)^T$ . To apply the PBC in the y-direction we connect the sites 1 and  $N_y$ , i.e the site  $N_y+1$  is the same of site 1.

In the original paper[31], it was shown that the vector  $\mathbf{G}$  that minimizes the ground-state energy for a set of parameters was calculated and then the Pfaffian was computed<sup>1</sup>. Since we wanted to check just the self-consistent calculation and the Pfaffian, we skipped this part and used the  $\mathbf{G}$  available in the paper.

In all cases we tested we found an agreement with the article so our functions should be working as intended.

Motivated by later results, which will be discussed in section 5.4, we calculate the gap while varying  $V_z$  for some parameters. The results are shown in Fig. 5.5 below.

---

<sup>1</sup>Every calculation used a self-consistently  $\Delta$ .

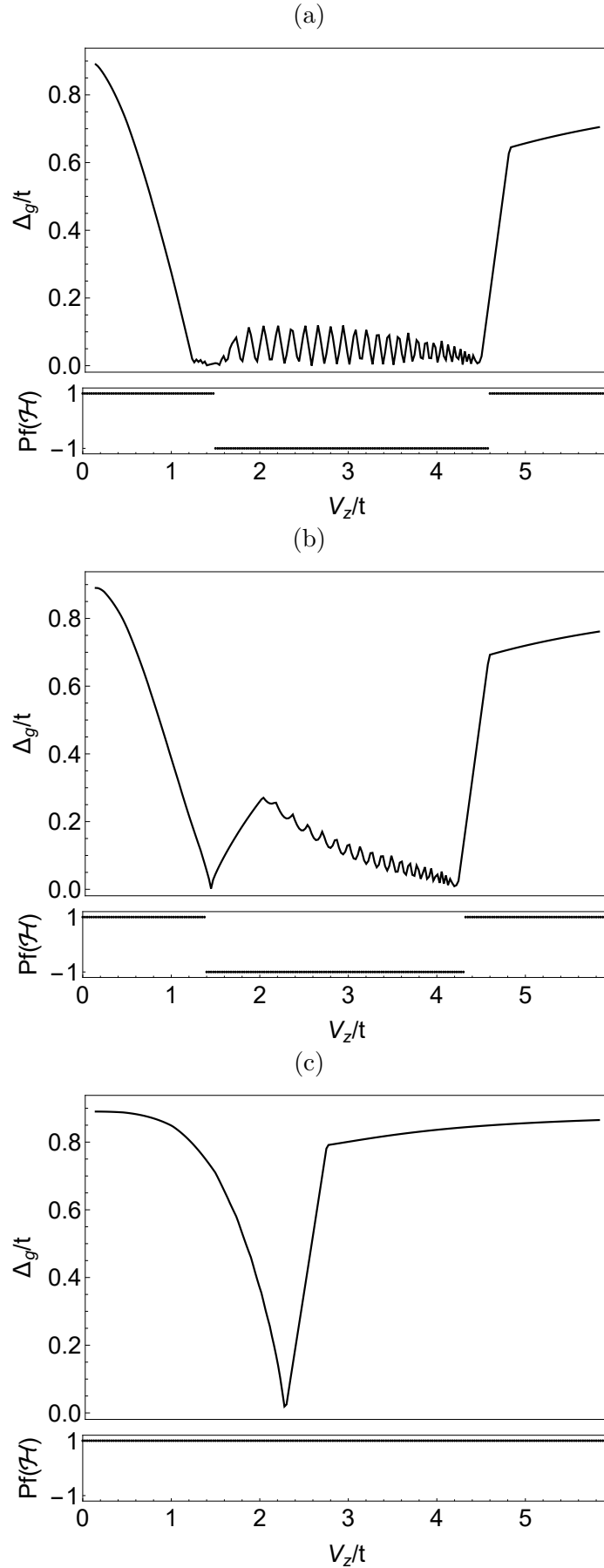


Figure 5.5: Oscillation in the gap for  $\mu = 3t$ , (a)  $G=0$  and  $V_z=2.4t$ , (b)  $G=1.01$  and  $V_z=2t$  and (c)  $G=3.14$  and  $V_z=1.6t$ .

When we have a topological phase we observe some oscillations related to the Majorana states interacting with each other, this oscillations don't change the topological phase so it was suggested that it could be used as a "smoking gun" evidence for the existence of Majorana bound state[2]. We also have critical  $V_z$  the system go back to trivial phase, destroying the Majorana.

We notice in Fig. 5.5, even tough the gap oscillates the sign of Pfaffian doesn't change

### 5.3 Superconducting Kane-Mele model

So far we have been developing the theory and the numerical tools needed to characterize the Majorana bound states in the model. We are now ready to study a impurity chain in the superconducting Kane-Mele model. Here we will use the same system that was used in section 3.1, a 400-atom honeycomb with 20-atoms in the armchair direction, and  $\lambda_{SO} = 0.5t$ ,  $\lambda_v = \lambda_R = 0$ ,  $U=2t$  and zero-temperature, unless stated otherwise. We will also consider a chain of impurities in the zigzag edge or in the armchair.

Differently from the end of chapter 3, we are not only interested in ferromagnetic and anti-ferromagnetic chains but also in spiral magnetic chains. All of them can be thought as a chain that starts with a magnetic moment and the next impurity is rotated by a  $\theta$  as shown in Fig. 5.6 (b). The ferromagnetic case is  $\theta=0$ , the antiferromagnetic is  $\theta = \pi$ , any other  $\theta$  will be called a "spiral phase". We proceed to study both chains shown in the figure below.

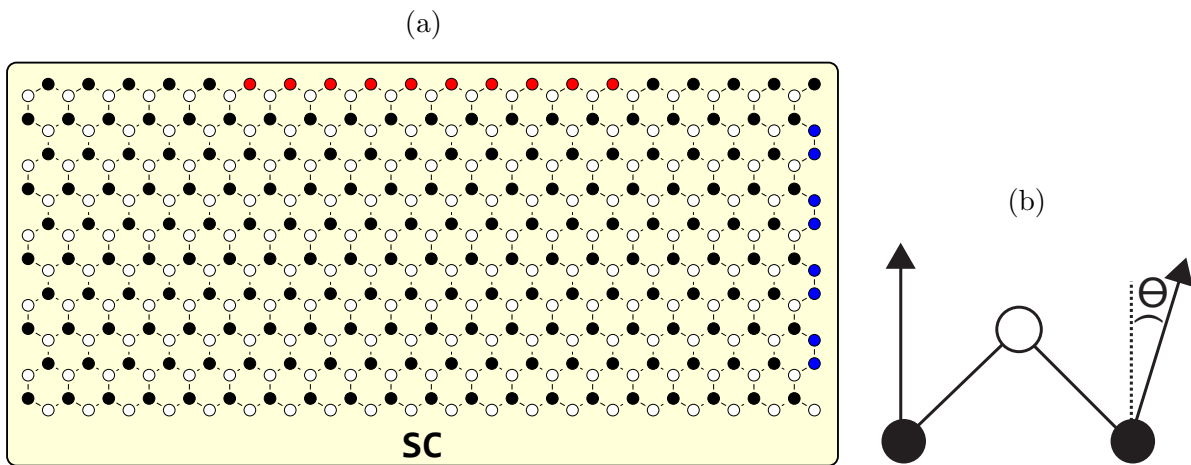


Figure 5.6: Configuration of our system. (a) the sample used with the impurities in the zigzag edge in red and in the armchair edge in blue. (b) the angle  $\theta$  between two impurities.

#### 5.3.1 Zigzag edge

With the above configuration, we can now ask the following question: which  $\theta$  minimizes the free-energy for some  $V_z$  and  $\mu$ , and this phase is topological non-trivial or not? With this

information, we can build a phase diagram.

In order to do this, we first calculate the free-energy for each  $\theta$  from  $-\pi$  to  $\pi$  with steps of  $\pi/60$ . Below we show one of those plots calculate for  $V_z = 2.3t$ :

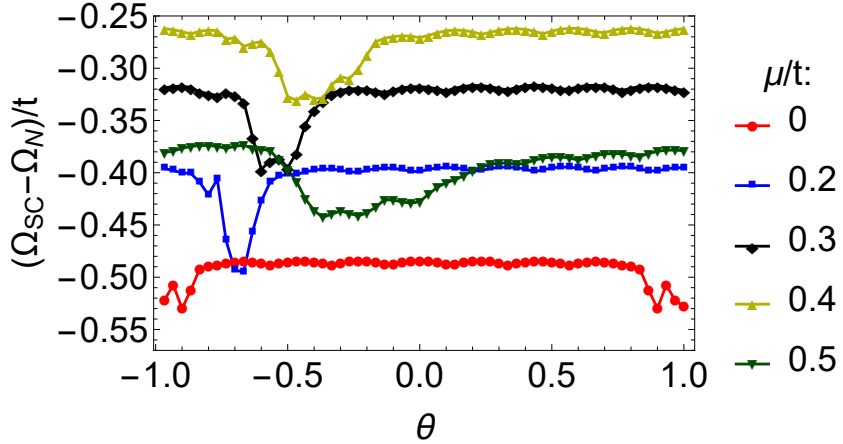


Figure 5.7: Dependence of free-energy with  $\theta$  for different  $\mu$ .

We see that, for some parameters, we have two minima (or the difference between the free-energy of two  $\theta$  is lower than the numerical error). For this case, we consider only one of the minima for constructing the phase diagram. We indicate that there are more than one  $\theta$  that minimizes the free-energy if they have different Majorana number.

Below we show a table with  $\theta$  that minimizes the free-energy. For this case, we calculated  $\Delta$  self-consistently:

$\mu \setminus V_z$	1.45	1.55	1.65	1.75	1.85	1.95	2.05	2.15	2.25	2.35	2.45	2.55	2.65	2.75
0.1	-0.97	-0.87	-0.93	-0.70	-0.73	-0.73	-0.77	-0.80	-0.80	-0.83	-0.83	-0.83	-0.83	-0.83
0.2	-0.57	-0.57	-0.60	-0.60	-0.63	-0.63	-0.67	-0.67	-0.67	-0.70	-0.70	-0.70	-0.70	-0.73
0.3	-0.43	-0.43	-0.50	-0.50	-0.47	-0.50	-0.50	-0.50	-0.50	-0.60	-0.60	-0.60	-0.60	-0.63
0.4	-0.37	-0.37	-0.37	-0.37	-0.40	-0.40	-0.40	-0.40	-0.40	-0.47	-0.47	-0.47	-0.50	-0.50
0.5	-0.23	-0.20	-0.20	-0.20	-0.33	-0.33	-0.30	-0.27	-0.23	-0.37	-0.37	-0.33	-0.33	-0.43
0.6	0.27	0.27	0.27	0.27	0.27	0.30	0.30	0.30	0.30	0.30	0.30	0.30	0.30	-0.37
0.7	0.37	0.37	0.37	0.37	0.40*	0.40	0.40	0.40	0.40	0.37	0.40*	-0.27	-0.27	-0.23

Table 5.1: Phase diagram with self-consistent method. The number inside the cell is  $\theta/\pi$ . Yellow and green: Majorana Number +1 and the angle of the chain is clockwise and anticlockwise. Blue and red: Majorana Number -1 and the angle of the chain is clockwise and anticlockwise. A (\*) means that exists more than one  $\theta$  and they have different Majorana number.

Two features are worth noticing in the table. First, we can see that for  $\mu \leq 0.2t$  there are no topological non-trivial phases. Second for  $\mu \geq 0.6t$  we start having a clockwise spiral,  $\theta > 0$ , instead of anti-clockwise,  $\theta < 0$ .

We can now calculate the LDOS over the impurity chain for  $V_z = 1.85t$  at zero-energy so we can see if the ends show zero-modes.

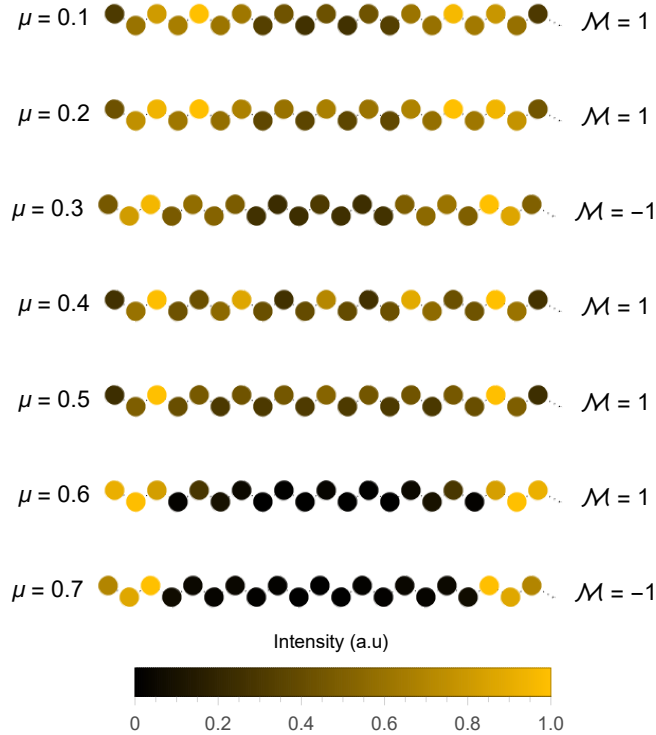


Figure 5.8: LDOS for  $E=0$  over the impurities for  $V_z = 1.85t$  with  $\theta$  shown in table 5.1.

From the LDOS alone, we can't distinguish between topological trivial and non-trivial phases, as all of them show high intensity in zero-energy states at the ends. This implies that we can't affirm that the ferromagnetic case shown in the ends of chapter 3 is a Majorana bound state. One possible way to probe whether the system is in the topological phase is to calculate the Pfaffian. As this procedure demands a large computational effort due the self-consistent method, one can ask: what if we started with  $\Delta$  calculated self-consistently for a clean sample, i.e. no impurities, and just add them with  $V_z \neq 0$  afterwards. The biggest difference between they is that impurities tend to suppress the  $\Delta$  locally as shown below:

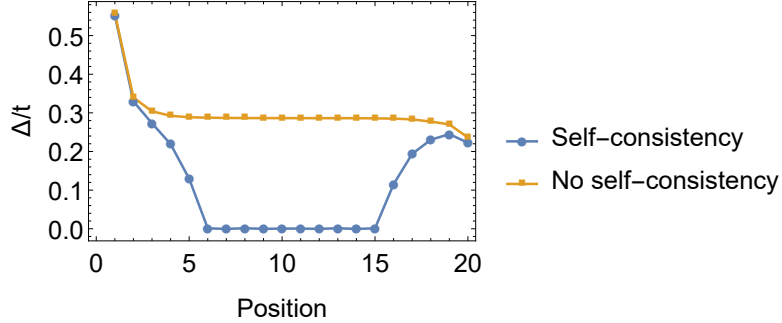


Figure 5.9: SOP over the sublattice A in the zigzag edge calculated with self-consistency, and without self-consistency, i.e using it only with clean sample  $V_z = 0$ .

Still we could ask: does Majorana bound states exist without enforcing the self-consistency condition in the zigzag edge? To answer that, we calculate the same phase diagram as table 5.1 but now without the self-consistency condition.

$\mu \setminus V_z$	1.45	1.55	1.65	1.75	1.85	1.95	2.05	2.15	2.25	2.35	2.45	2.55	2.65	2.75
0.2	-0.83	-0.83	-0.80	-0.80	-0.80	-0.87	-0.77	-0.67	-0.70	-0.70	-0.70	-0.70	-0.70	-0.67*
0.3	-0.70	-0.80	-0.67	-0.77	-0.77	-0.73	-0.73	-0.53	-0.57	-0.57	-0.57	-0.60*	-0.60	-0.60
0.4	-0.67	-0.67	-0.67	-0.63	-0.63	-0.47*	-0.37	-0.37*	-0.40	-0.40	-0.40	-0.37	-0.37	-0.37
0.5	-0.70	-0.67	-0.67	-0.37	-0.33	-0.33	-0.17	-0.17	-0.03	-0.03	0	-0.20*	-0.20	-0.17
0.6	0.23	0.23	0.27	0.27	0.27	0.27	0.27	0.27	0.30	0.27	0.27	0.27	0.30*	0.30
0.7	0.30	0.30*	0.30*	0.30	0.30	0.33	0.37*	0.37	0.37	0.37	0.37	0.33	0.33*	0.33

Table 5.2: Phase diagram without self-consistent method. The number inside the cell is  $\theta/\pi$ . Yellow and green: Majorana Number +1 and the angle of the chain is clockwise and anticlockwise. Blue and red: Majorana Number -1 and the angle of the chain is clockwise and anticlockwise. A (\*) means that exists more than one  $\theta$  and they have different Majorana number.

This diagram is very different from the self-consistent one, Table 5.1, as both the  $\theta$  that minimizes the free-energy and the Majorana number change for a given set of parameters. However, Majorana bound states do appear even at low values of  $\mu$  such as  $\mu = 0.2t$ . We can try and calculate a LDOS for zero-energy to see if we can now distinguish the different topological phases. The results are shown in Fig. 5.10 in which is possible to observe the same phenomenon that happened in the self-consistency case.

It is clear from this that the appearance of topological trivial zero-states is a robust property of the system and it does not depend on whether or not we include the self-consistent loop in the calculations.

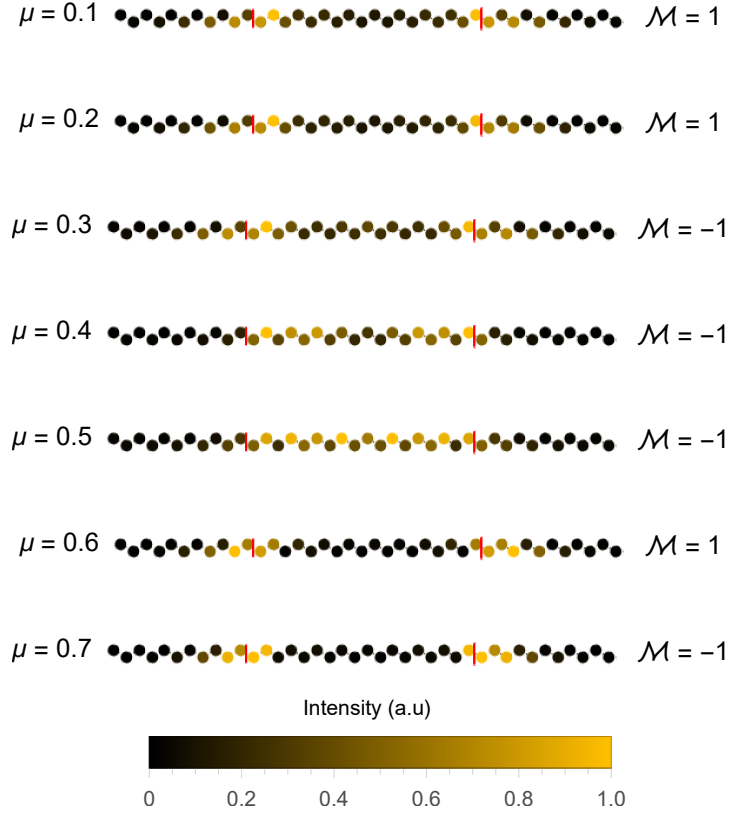


Figure 5.10: LDOS for  $E=0$  through the zigzag edge for  $V_z = 2.05t$  with  $\theta$  shown in table 5.2. The red line shows the start and end of the impurity chain.

To conclude this part, we add 20 more impurities in the middle of the chain, forming a 30-impurity chain. Now our sample has 40 atoms in the zigzag instead of 20. We start with the  $\theta$  from table 5.1 and calculate  $\Delta$  self-consistently. In Table 5.3, below, we show the phase diagram:

$\mu \setminus V_z$	1.45	1.55	1.65	1.75	1.85	1.95	2.05	2.15	2.25	2.35	2.45	2.55	2.65	2.75
0.2	-0.83	-0.57	-0.60	-0.60	-0.63	-0.63	-0.67	-0.67	-0.67	-0.70	-0.70	-0.70	-0.70	-0.73
0.3	-0.43	-0.43	-0.50	-0.50	-0.47	-0.50	-0.50	-0.50	-0.50	-0.60	-0.60	-0.60	-0.60	-0.63
0.4	-0.37	-0.37	-0.37	-0.37	-0.40	-0.40	-0.40	-0.40	-0.40	-0.47	-0.47	-0.47	-0.50	-0.50
0.5	-0.23	-0.20	-0.20	-0.20	-0.33	-0.33	-0.30	-0.30	-0.23	-0.37	-0.37	-0.33	-0.33	-0.43
0.6	0.27	0.27	0.27	0.27	0.27	0.27	0.27	0.30	0.30	0.30	0.30	0.30	0.30	-0.37
0.7	0.33	0.33	0.33	0.30	0.33	0.37	0.37	0.37	0.37	0.33	0.30	-0.27	-0.27	-0.27

Table 5.3: Phase diagram with self-consistent method for a chain of 30 impurities. The number inside the cell is  $\theta/\pi$ . Yellow and green: Majorana Number +1 and the angle of the chain is clockwise and anticlockwise. Blue and red: Majorana Number -1 and the angle of the chain is clockwise and anticlockwise. A (\*) means that exists more than one  $\theta$  and they have different Majorana number.

The result is very different from table 5.1 which lead us to think that the size of the chain

affects the topological state. This is expected as the two MBS located at the edges of the chain couple more strongly each other for smaller chain sizes. Indeed, we observe this, in our calculations. Fig 5.11, shows that even for a chain with same size depending on the parameters we will have MBS interacting more and different topological phases.

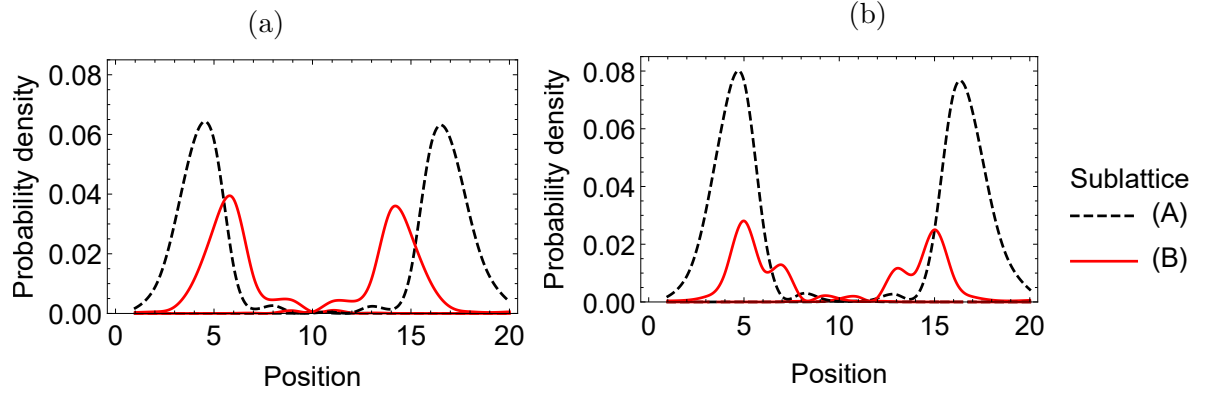


Figure 5.11: Probability density for the states with almost zero-energy. The position correspond to each site in the zigzag edge, the impurity chain ranges from position 6 to 15 in sublattice A. Here we have two cases for  $\theta = 0$  (a)  $V_z = 3t$  and  $M=-1$  and (b)  $V_z=1.85t$  and  $M=1$ .

Those interactions actually change the energy of the end-states and now it becomes quasi zero-energy states. For different size of chains this interaction changes and the topological phase might change. We now plot the energy states when changing the field  $V_z$  for the ferromagnetic case, see Fig 5.1. We note that the energy of the edge states is not fixed at zero but actually oscillates with  $V_z$ , Fig. 5.12.

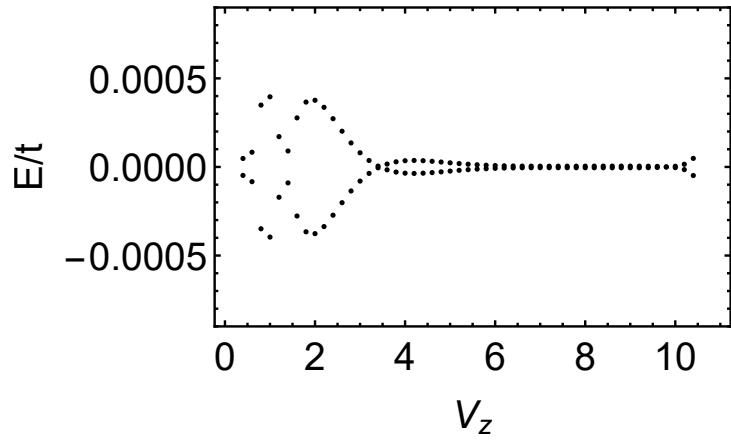


Figure 5.12: Zoom in the energy spectrum for 10 impurities chain in the ferromagnetic case.

Although this oscillation look similar to the ones we found in the square lattice, Fig. 5.5, they are actually different as the Pfaffian changes sign for every oscillation. We will study more in depth these oscillations and how they are affected by the parameters.

## 5.4 Gap oscillations

We now look closer the oscillations shown in Fig. 5.12 above. In 2012 Das Sarma and collaborators[2] argued that, in a square lattice, such gap oscillations could be a sign of Majorana bound state. They predicted that the oscillations should increase in amplitude and be described with the following equation:

$$\Delta E \approx \hbar^2 k_{F,eff} \frac{e^{-2L/\xi}}{m\xi} \cos[k_{F,eff} L],$$

with  $k_{F,eff}$  the effective Fermi wave vector associated with the zero-mode,  $\xi$  the effective coherence length, both of them depending on the system's parameter, and  $L$  the Length separating the two Majorana.

Later, in 2016 an article published by the Marcus group in Nature[15] showing experimental results for a InAs nanowire, found a decreasing amplitude with the magnetic field  $V_z$ . This lead to another paper by the Das Sarma group[32] that tried to explain this effect and found that a mixture of Andreev bound states and Majorana were responsible for this.

Although the Andreev bound states needed to be added by hand[32] or by considering quantum dots in the system[33], interestingly, a similar behavior occurs naturally in our model by a simple change of parameters. Below we show this oscillations and the change in Pfaffian with every time the bands cross the zero-energy.

Changing the spin-orbit coupling,  $\lambda_{SO}$ , does not change the results qualitatively. As  $\lambda_{SO}$  decreases, the oscillations get sharper and the amplitude increases, as shown in Fig. 5.13.

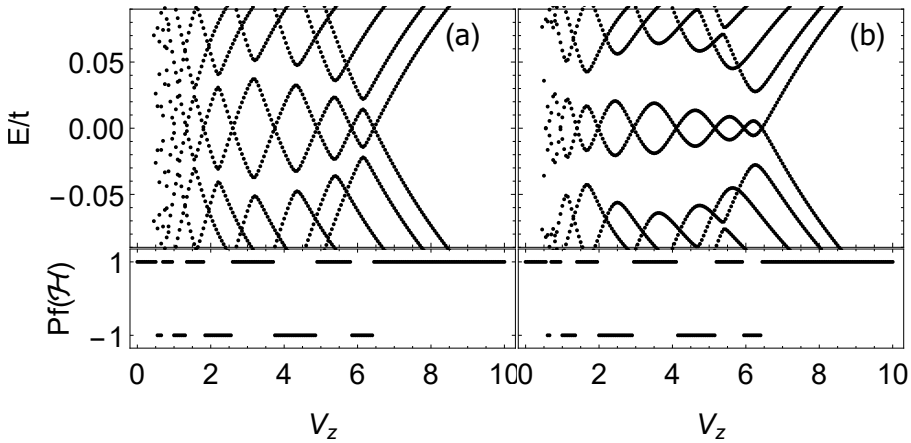


Figure 5.13:  $\mu=0.4$  and  $\theta=0$ . Oscillations with varying impurity strength  $V_z$  for  $\lambda_{so}$  (a)  $0.1t$  and (b)  $0.3t$ .

Increasing the staggering potential,  $\lambda_v$ , also increases the oscillation amplitude, as shown in Fig. 5.14. This indicates that the Majorana bound states interact more with each other probably

because they would leak less to the other sublattice.

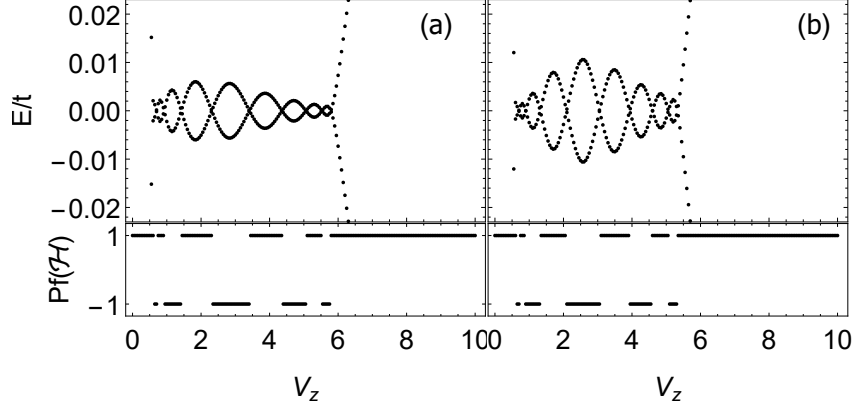


Figure 5.14:  $\mu=0.4$   $\theta = 0$ . Oscillations with varying impurity strength  $V_z$  for  $\lambda_v$  (a)  $0.05t$  and (b)  $0.1t$ .

In Figs. 5.15 and 5.16, each panel shows a fixed spiral angle,  $\theta$ , for  $\mu = 0.4t$  (Fig. 5.15) and for  $\mu = 0.2t$  (5.16). The effect of  $\theta$  can be thought as a effective spin-orbit coupling, and since we already have a spin-orbit coupling  $\lambda_{SO}$  depending on the sign of this new spin-orbit we have different effects and that is why a clockwise or anti-clockwise rotation will have different effect.

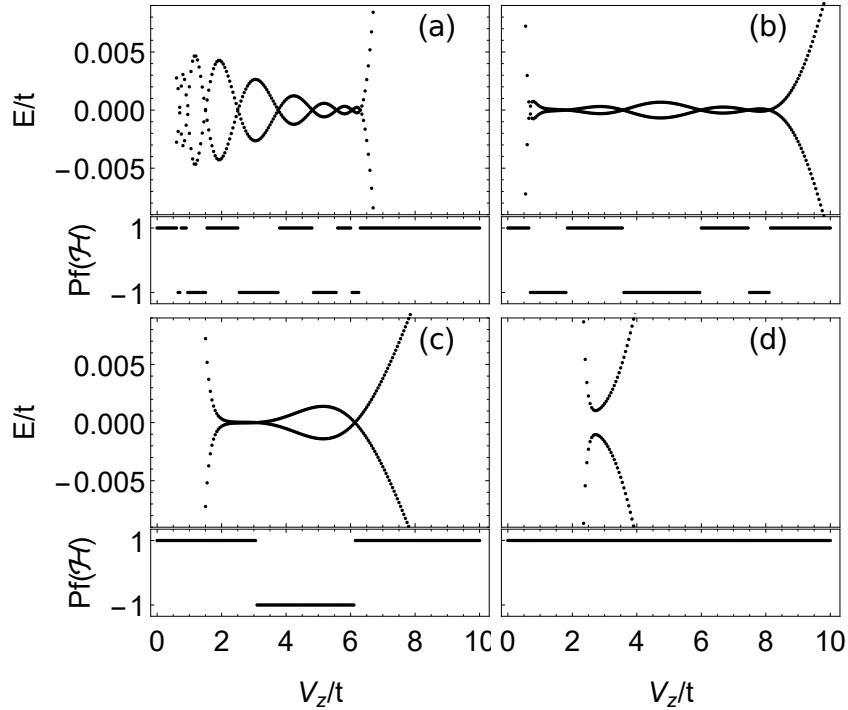


Figure 5.15:  $\mu=0.4$   $\lambda_r = 0$ . Oscillations with varying impurity strength  $V_z$  for  $\theta$  (a)  $0$ , (b)  $\pi/2$ , (c)  $\pi$  and (d)  $5\pi/4$ .

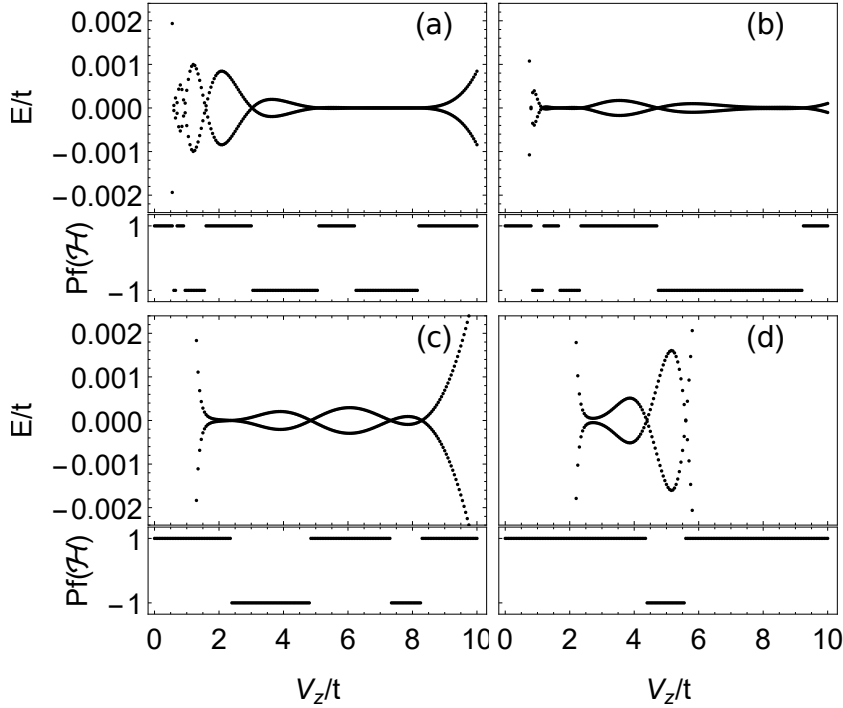


Figure 5.16:  $\mu=0.2$   $\lambda_r = 0$ . Oscillations with varying impurity strength  $V_z$  for  $\theta$  (a) 0, (b)  $\pi/2$ , (c)  $3\pi/4$  and (d)  $\pi$ .

Figs. 5.17 and 5.18, show panels with different Rashba coupling,  $\lambda_R$ , for fixed spiral angles ( $\theta = 0$  and  $\pi/2$  respectively). We can see that the amplitude grows with increasing Rashba coupling, also the number of times the gap crosses zero decreases. This could be due Rashba coupling creating an interaction between the impurity and the closest neighbor which allows the end states of the chain to interact more.

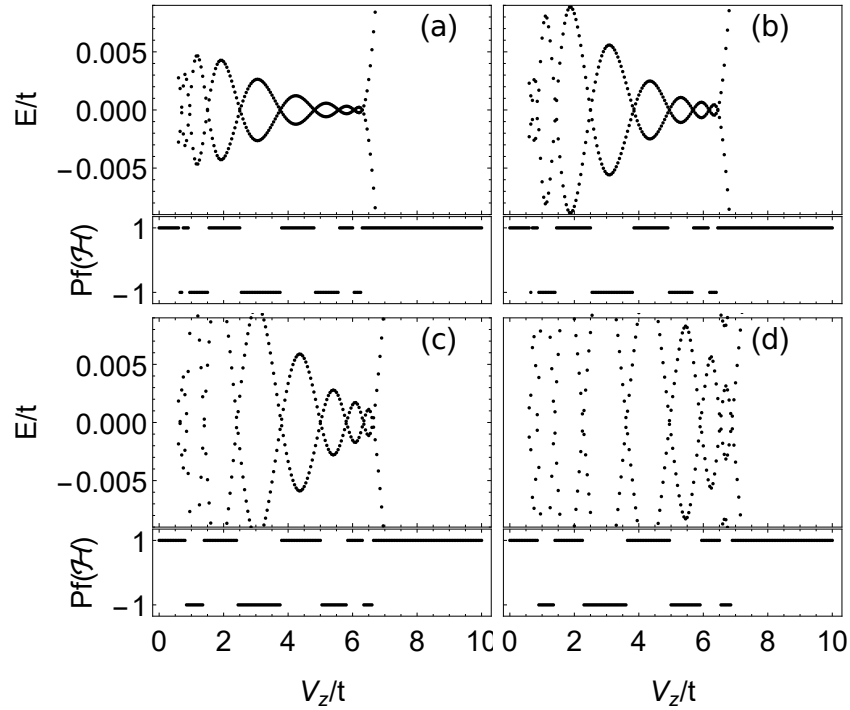


Figure 5.17:  $\mu=0.4$   $\theta = 0$ . Oscillations with varying impurity strength  $V_z$  for  $\lambda_r$  (a) 0, (b)  $0.05t$ , (c)  $0.07t$  and (d)  $0.1t$ .

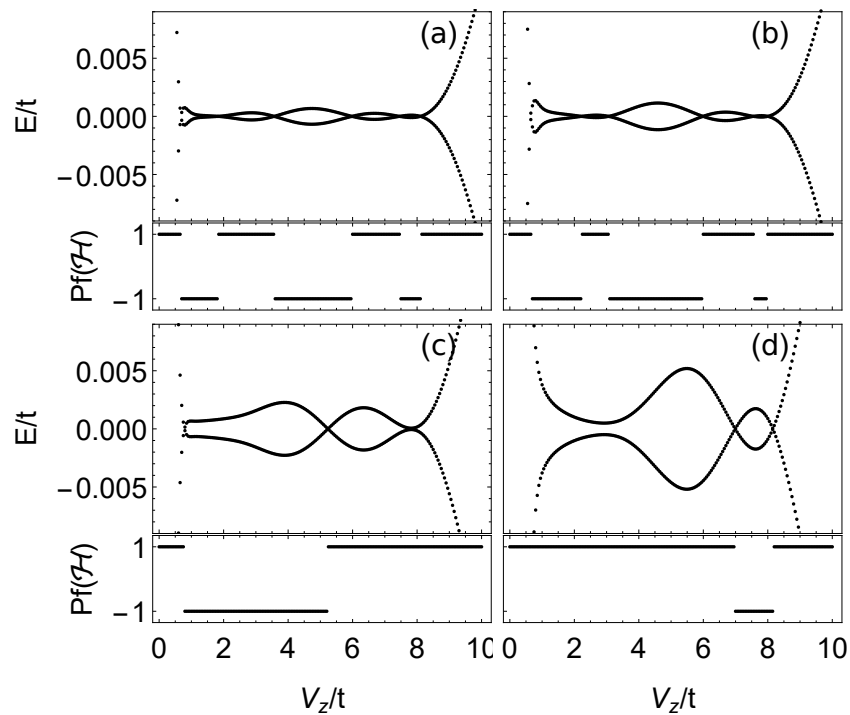


Figure 5.18:  $\mu=0.4$   $\theta = \pi/2$ . Oscillations with varying impurity strength  $V_z$  for  $\lambda_r$  (a) 0, (b)  $0.05t$ , (c)  $0.1t$  and (d)  $0.15t$ .

We end this section showing that gap oscillations also occur as the chemical potential changes for a fixed field<sup>2</sup>, as shown in Fig. 5.19. As in the case of varying  $V_z$ , the Pfaffian also changes sign at the crossing points. This behavior is distinct of that of the square lattice, where the gap oscillates by changing the doping, although the Pfaffian does not change [2].

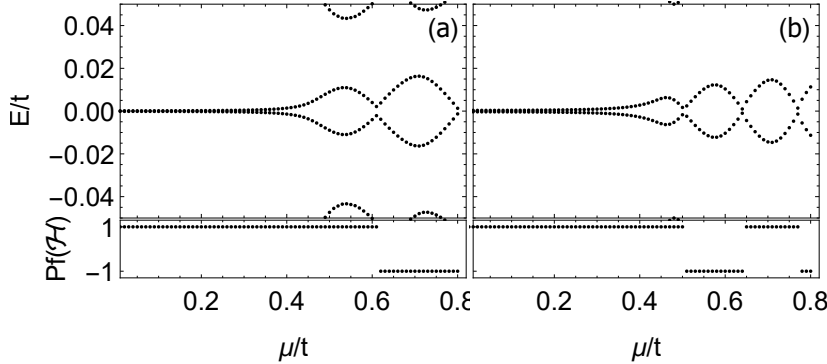


Figure 5.19:  $\theta = 0$ . Oscillations with varying doping  $\mu$  for  $V_z$  (a)  $1.45t$  and (b)  $1.85t$ .

### 5.4.1 Armchair edge

Now we proceed to study an impurity chain in the armchair edge, with a configuration that can be seen in figure 5.6 (b). If on the one hand we have a rich phase diagram for the zigzag edge, on the other hand we don't see any phase transitions in the armchair edge.

In table 5.4 we show the phase diagram. We choose to show the phase every  $0.4t$  as we could cover a larger range of  $V_z$  and no topological phase was found in between.

$\mu \setminus V_z$	0.4	0.8	1.2	1.6	2.	2.4	2.8	3.2	3.6	4.	4.4	4.8
0.2	0.27	0.43	0.57	0.57	0.20	0.23	0.23	0.27	0.30	0.30	0.33	0.33
0.3	0.07	0.50	0.70	0.70	0.50	0.33	0.33	0.17	0.17	0.17	0.13	0.13
0.4	0.40	0.63	0.57	0.57	0.40	0.43	0.47	0.47	0.27	0.27	0.27	0.27
0.5	0.43	0.67	0.67	0.73	0.53	0.57	0.57	0.57	0.57	0.40	0.40	0.40
0.6	0.33	0.47	0.53	0.53	0.40	0.40	0.40	0.40	0.40	0.40	0.40	0.40
0.7	0.47	0.57	0.93	0.83	0.70	0.53	0.53	0.53	0.53	0.53	0.50	0.50
0.8	0.50	0.87	0.93	0.87	0.77	0.63	0.57	0.53	0.50	0.50	0.50	0.47

Table 5.4: Phase diagram with self-consistent method. The number inside the cell is  $\theta/\pi$ . Yellow: Majorana Number +1 and the angle of the chain is clockwise.

The reason for this is that we don't see zero-energy states that for a finite range of  $V_z$  in this configuration. Instead, we have at most one point with  $E=0$ . This can be seen in the energy spectrum for the ferromagnetic case, shown in Fig. 5.20 below.

<sup>2</sup>These energy spectrum were calculated using self-consistency method.

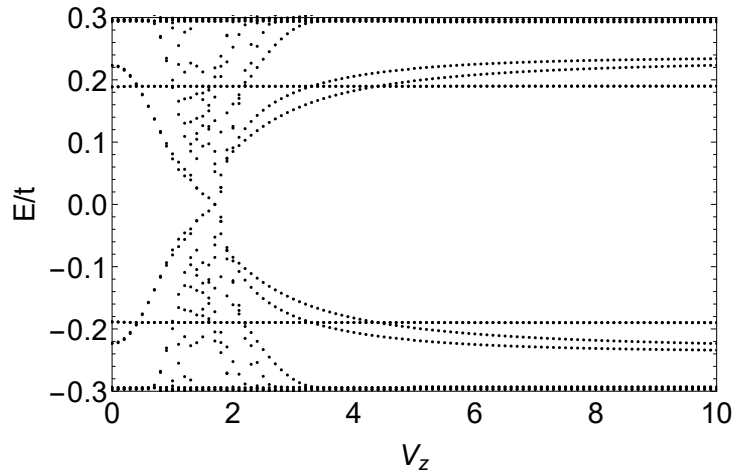


Figure 5.20: Energy spectrum with changing field  $V_z$  with  $\theta = 0$  and  $\mu = 0.1t$  in the armchair edge. Note that we don't have many

Thus, our results then point to the conclusion that only magnetic chains on zig-zag edges will display Majorana zero modes for a finite range of  $V_z$  values.



# Chapter 6

## Conclusions

### 6.1 Overview

In this work, we try to answer a simple question: can Majorana bound states occur in impurity chains placed in the edges of silicene or other 2D materials with strong spin-orbit coupling?

This question makes sense when considering the theoretical and experimental implication of Majorana bound states, and the different properties of honeycomb lattice materials as compared to other lattice geometries in 2D.

In order to provide an answer, we review some important points about topological insulators and honeycomb lattice models. We introduce the Haldane model due to its historical importance and followed up with the Kane-Mele model[1], as a more realistic approach to describe honeycomb lattice topological materials, showing the existence of edge states and finite size effects.

Majorana bound states can appear as edge modes in topological superconductors. In order to have the appropriate conditions for MBSs to emerge in our system, we introduced a proximity induced superconductivity and a chain of magnetic impurities located in a zig-zag edge. We characterize the properties of this model and how the different phases depends upon the parameters of Kane-Mele model and the magnetic impurity strength.

### 6.2 Superconducting Kane-Mele model

Following up on the Majorana trail, we show how to calculate the position-dependent superconducting order parameter in the lattice in a self-consistent fashion. We use this to compute

the SOP at the edges and in the center of a finite sample and how it depends upon the doping, spin-orbit coupling, staggering potential, Rashba coupling and pair potential.

This is an important result as we use it to choose the values of these parameters for the following sections, such that the superconductivity is mostly present at the edges (we still have a residual superconductivity in the middle due finite size effects).

We continue adding the local magnetic impurity, and we show that only in-plane spins allow a zero-energy state to occur in a critical impurity's magnetic moment. This critical value is related to a phase transition and a  $\pi$ -phase change in the SOP, as it happens in other systems[26].

With this we have enough elements to build an impurity-chain and try to find a Majorana bound state. To do this, we build a chain with spiral moments, defined by an angle  $\theta$ , and we search which angle minimizes the free-energy of the system, for a set of parameters.

Using this information, we build a phase diagram showing the existence of Majorana bound states only in the zigzag edge. However, here we find a problem when studying the LDOS for energies close to zero, we can't distinguish the MBS from trivial states. Here we found that this indistinguishability is related to gap oscillations.

### 6.3 Gap oscillations

Those oscillations appear both in the square and the honeycomb lattices, due to a finite-size-induced coupling of the Majorana modes at the ends of the magnetic chain. These gap oscillations have important experimental consequences and was even dubbed a “smoking gun” for detecting Majorana bound states[2].

However, we show that in the superconducting Kane-Mele model those oscillations actually are accompanied by a change of sign in Pfaffian, which could be interpreted as transitions in and out of the topological state. This is an interesting feature, as those states continue at the end of the chain even after morphing in a non-topological state. This explains why we can't capture the difference in the LDOS, because it's the same state that changes.

We are still not sure the mechanism behind those changes, why they happen in the honeycomb lattice and not in the square lattice. This is still an on-going research. From this point, we try to understand how the parameters of our system affect the shape of those oscillations as in square lattice they are expected to *increase* the amplitude[2] while experimental results show a *decrease* in amplitude[15].

Here, we find that in general the staggering potential and Rashba couplings behave similarly: by increasing their value actually increases the amplitude of the oscillation as a function of the

impurity magnetization (which takes the role of a magnetic field here). This shows that both parameters increase the interactions between the MBSs, even though the mechanism for this is different. The staggering potential probably does not allow the MBS to leak to a different sublattice increasing the interaction in the chain, while the Rashba coupling creates a new channel for the MBS to interact.

We also found that increasing the spin-orbit coupling decreases the amplitude and changing the impurities' rotation in the chain will change the oscillations depending on the rotation direction (clockwise or anticlockwise) as it will change the effective spin-orbit coupling of the chain.

All of this suggests that this theme is not completely understood and a better description both of the mechanism and the shape of the oscillations is needed.

## 6.4 Experimental implications

Our results have a broad practical implication. If we want to host MBS using silicene or other honeycomb lattice material as basis, we might not know in which regime we are just by looking at the LDOS. Small changes could change from MBS to a trivial state if the system was close to a closing point in the gap oscillation.

Probably one of the best way to determine if it is a MBS, would be testing when we have non-abelian statistics, but right now this is very difficult to accomplish (although it is a result many important experimental groups are competing to achieve!). Because of this using the edge of silicene to host Majorana bound states to apply in quantum computation might not be ideal.

However, this system might still be of practical interest as it is prone to host interesting properties both due its geometry and because of the mixture of topological insulator and superconductor.

## 6.5 Further developments

We believe this work can pave the way for many future developments. Primarily, and with great experimental interest, would be to check whether gap oscillations are indeed a "smoking gun signature" of Majorana bound states in magnetic chains.

A second possible development is to understand the mechanism behind the change from Majorana bound state to a trivial phase as the gap oscillates. A model that can explain it would also be able to relate the parameters with the shape of oscillations and how we can control it, so it could be used.

We are currently writing a paper in collaboration with Dushko Kuzmanovski and Annica Black-Schaffer, in which we discuss the gap oscillation. We expect that this work can lead to a clarification of these results and further developments in the topic.

# Appendix A

## Pfaffian

As we saw in chapters 2 and 3 the Sign of Pfaffian is related with topological invariant  $Z_2$  and Majorana number. Because of this is worth to state its definition and show some of its properties even though we might not prove them.

We define the Pfaffian for a anti-symmetric  $2n$  square-matrix  $A$  as:

$$Pf(A) = \frac{1}{2^n n!} \sum_{\substack{\text{Permutations of} \\ \{i_1, \dots, i_{2n}\}}} sgn(P) A_{i_1 i_2} \dots A_{i_{2n-1} i_{2n}}, \quad (\text{A.1})$$

and zero if it a matrix of odd order.  $Sgn(P)$  is 1 if  $P$  is an even permutation and -1 if  $P$  an odd permutation. As example let us consider a  $4 \times 4$  matrix:

$$A = \begin{pmatrix} 0 & a & b & c \\ -a & 0 & d & e \\ -b & -d & 0 & f \\ -c & -e & -f & 0 \end{pmatrix},$$

then  $Pf(A) = af - be + dc$ .

The Pfaffian also have some interesting properties. Let  $A$  be an antisymmetric  $2n \times 2n$  matrix and  $S$  also a  $2n \times 2n$  matrix then:

- $Pf(A)^2 = \det(A)$
- $Pf(A^T) = (-1)^n Pf(A)$
- $Pf(\beta A) = \beta^n Pf(A)$
- $Pf(SAS^T) = \det(S) Pf(A)$

To calculate the Pfaffian we used the package written by Wimmer[34], as it is more efficient than calculating the permutations.

# Appendix B

## Derivation Kane-Mele

In this appendix we derive step by step each element from the Kane-Mele Hamiltonian. Since this calculation is straightforward, we will do only for the quasi-1D case, because of the presence of edge-states. However, it should be noticed that the biggest difference from the bulk-Hamiltonian is the size of the unity cell and the periodic condition at the y-direction.

We will consider the following cell for our calculations:

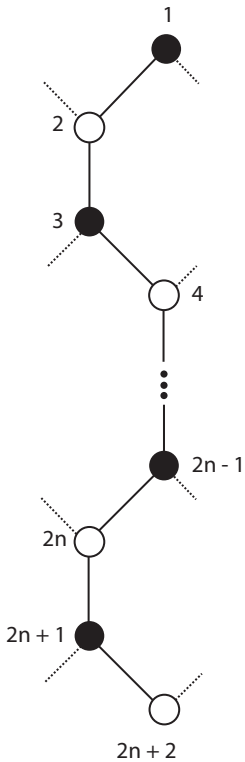


Figure B.1: Unitary cell for  $n$  strips. We will call the odd numbered sublattice A and the even numbered sublattice B.

where we named the sites with numbers so it is clear what our basis  $(c_{1,k,\uparrow}^\dagger |0\rangle, c_{2,k,\uparrow}^\dagger |0\rangle, \dots, c_{2(N+1),k,\uparrow}^\dagger |0\rangle, c_{1,k,\downarrow}^\dagger |0\rangle, c_{2,k,\downarrow}^\dagger |0\rangle, \dots, c_{2(N+1),k,\downarrow}^\dagger |0\rangle)$  means.

## Staggering potential and doping

Both of this terms are onsite energies, i.e. they are written as  $\epsilon c_i^\dagger c_i$  so when we fourier-transform to k-space they won't depend on k and are simple diagonal terms as before.

## Hopping

The hopping term  $tc_i^\dagger c_j$  with i and j being neighbors is simple to compute. We have two possibilities for thee neighbors position. Either the positions are  $\vec{R}$  and  $\vec{R} + a\hat{j}$  or the positions are  $\vec{R}$  and  $\vec{R} + \left(\frac{a\sqrt{3}}{2}\hat{i} + \frac{a}{2}\hat{j}\right)$ .

The first case is the simplest:

$$tc_i^\dagger c_j = \frac{t}{V} \left( \sum_k e^{-ikr} c_{i,k}^\dagger \right) \left( \sum_{k'} e^{ik'(r+a\hat{j})} c_{j,k'} \right), \quad (\text{B.1})$$

since k is only in the x-direction, we have

$$\frac{t}{V} \left( \sum_k e^{-ikr} c_{i,k}^\dagger \right) \left( \sum_{k'} e^{ik'(r+a\hat{j})} c_{j,k'} \right) = \frac{t}{V} \sum_{k,k'} e^{i(k'-k)r} c_{i,k}^\dagger c_{j,k'} = tc_{i,k}^\dagger c_{j,k'} \quad (\text{B.2})$$

The second case is also simple but now we have to consider the hopping not only in the same cell but the one next to it so we will have 2 sums:

$$tc_i^\dagger c_j = \frac{t}{V} \left( \sum_k e^{-ikr} c_{i,k}^\dagger \right) \left( \sum_{k'} e^{ik'(r+[a\sqrt{3}/2\hat{i}+a/2\hat{j}])} c_{j,k'} \right) + \frac{t}{V} \left( \sum_k e^{-ikr} c_{i,k}^\dagger \right) \left( \sum_{k'} e^{ik'(r+[-a\sqrt{3}/2\hat{i}+a/2\hat{j}])} c_{j,k'} \right), \quad (\text{B.3})$$

$$tc_i^\dagger c_j = \frac{t}{V} \sum_{k,k'} e^{i(k'-k)r} \left( e^{ik\sqrt{3}/2a} + e^{-ik\sqrt{3}/2a} \right) = 2t \cos[\frac{\sqrt{3}}{2}ka] c_{i,k}^\dagger c_{j,k} \quad (\text{B.4})$$

Here we used that  $\frac{1}{V} \sum_{k,k'} e^{i(k'-k)r} = \delta(k - k')$  and that the sum over k is understood when writing both  $c^\dagger$  and c that depends upon the same k.

## Spin-orbit coupling

The spin-orbit coupling doesn't mix the spins, as it is proportional to  $s_z$ . Below we show the coefficient  $\nu_{ij}$  for each type of interaction. We separate them in 6 different

configurations to simplify the matrix elements calculation.

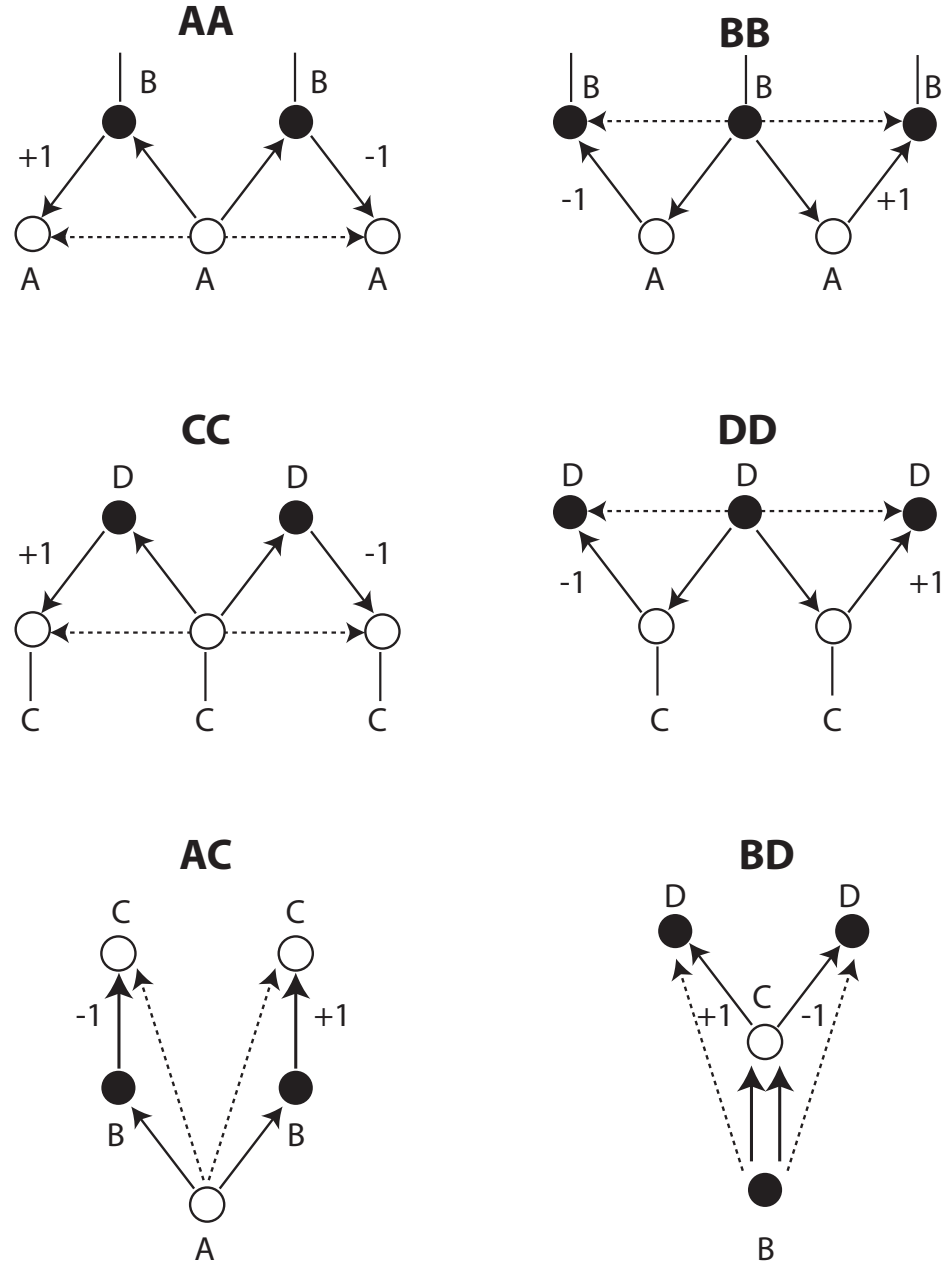


Figure B.2: Sign of  $\nu_{ij}$  for each possible interaction. The difference between AA and CC or BB and DD is the position in relation to the edge - for the calculations they are the same.

For the AA or CC, case we have the site in the unit cell interacting with the same site

of the near unit cells so we have for the AA case:

$$\begin{aligned} i \frac{\sqrt{3}\lambda_{SO}}{3} c_A^\dagger s_z c_A &= i \frac{\sqrt{3}\lambda_{SO}}{3V} \left( \sum_k e^{-ikr} c_{A,k}^\dagger \right) s_z \left[ \sum_{k'} \left( -e^{ik'(r+a\sqrt{3})} + e^{ik'(r-\sqrt{3}a)} \right) c_{A,k'} \right] = \\ &\quad \frac{2\sqrt{3}\lambda_{SO}}{3} s_z \sin(k\sqrt{3}a) c_{A,k}^\dagger c_{A,k}. \end{aligned} \quad (\text{B.5})$$

We have a similar result for BB or DD, but now we have a minus sign due to  $\nu_{ij}$ :

$$\begin{aligned} i \frac{\sqrt{3}\lambda_{SO}}{3} c_B^\dagger s_z c_B &= i \frac{\sqrt{3}\lambda_{SO}}{3V} \left( \sum_k e^{-ikr} c_{B,k}^\dagger \right) s_z \left[ \sum_{k'} \left( e^{ik'(r+\sqrt{3}a)} - e^{ik'(r-\sqrt{3}a)} \right) c_{B,k'} \right] = \\ &\quad - \frac{2\sqrt{3}\lambda_{SO}}{3} s_z \sin(k\sqrt{3}a) c_{B,k}^\dagger c_{B,k}. \end{aligned} \quad (\text{B.6})$$

We now start the interaction between two different sites, for AC we have:

$$\begin{aligned} i \frac{\sqrt{3}\lambda_{SO}}{3} c_C^\dagger s_z c_A &= i \frac{\sqrt{3}\lambda_{SO}}{3V} \left( \sum_k e^{-ikr} c_{C,k}^\dagger \right) s_z \left[ \sum_{k'} \left( e^{ik'(r+a\sqrt{3}/2\hat{i}+a/2\hat{j})} - e^{ik'(r-a\sqrt{3}/2\hat{i}+a/2\hat{j})} \right) c_{A,k'} \right] = \\ &\quad - \frac{2\sqrt{3}\lambda_{SO}}{3} s_z \sin(\sqrt{3}/2ka) c_{C,k}^\dagger c_{A,k}. \end{aligned} \quad (\text{B.7})$$

The BD case we have:

$$\begin{aligned} i \frac{\sqrt{3}\lambda_{SO}}{3} c_D^\dagger s_z c_B &= i \frac{\sqrt{3}\lambda_{SO}}{3V} \left( \sum_k e^{-ikr} c_{D,k}^\dagger \right) s_z \left[ \sum_{k'} \left( -e^{ik'(r+a\sqrt{3}/2\hat{i}+a/2\hat{j})} + e^{ik'(r-a\sqrt{3}/2\hat{i}+a/2\hat{j})} \right) c_{B,k'} \right] = \\ &\quad \frac{2\sqrt{3}\lambda_{SO}}{3} s_z \sin(\sqrt{3}/2ka) c_{D,k}^\dagger c_{B,k}. \end{aligned} \quad (\text{B.8})$$

## Rashba

The Rashba coupling mix spins, therefore it will be elements at the block anti-diagonal. Here we will be using the same nomenclature as in the spin-orbit sections. We will be using the following unitary vectors that describe the nearest neighbors at the honeycomb lattice:

$\mathbf{a}_1 = \hat{j}$ ,  $\mathbf{a}_2 = \sqrt{3}/2\hat{i} + 1/2\hat{j}$ ,  $\mathbf{a}_3 = \sqrt{3}/2\hat{i} - 1/2\hat{j}$ , so the coefficient  $(\mathbf{s} \times \mathbf{d}_i)_z$  are:

$$(\mathbf{s} \times \mathbf{a}_1)_z = \sigma_x, \quad (\text{B.9a})$$

$$(\mathbf{s} \times \mathbf{a}_2)_z = \frac{1}{2}\sigma_x - \frac{\sqrt{3}}{2}\sigma_y, \quad (\text{B.9b})$$

$$(\mathbf{s} \times \mathbf{a}_3)_z = -\frac{1}{2}\sigma_x - \frac{\sqrt{3}}{2}\sigma_y. \quad (\text{B.9c})$$

Now we can easily compute the matrix elements associated with the Rashba term. This is a nearest neighbor interaction, so we will have AB,BC,CD. However the spins will be opposite. It worth note that since these elements we calculate are imaginary we also have the interactions BA,CB,DC. We will use the notation  $c_A$  as a vector with two components  $(c_{A,\uparrow}, c_{A,\downarrow})$ . Now we will calculate the AB element.

$$= i \frac{2\lambda_R}{3} \left( \sum_k e^{-ikr} c_{A,k}^\dagger \right) \left\{ \sum_{k'} \left[ \left( -\frac{1}{2}\sigma_x + \frac{\sqrt{3}}{2}\sigma_y \right) e^{ik'(r+a\sqrt{3}/2\hat{i}+a/2\hat{j})} + \left( -\frac{1}{2}\sigma_x - \frac{\sqrt{3}}{2}\sigma_y \right) e^{ik'(r-a\sqrt{3}/2\hat{i}+a/2\hat{j})} \right] c_{B,k'} \right\} \quad (\text{B.10a})$$

$$i \frac{2\lambda_R}{3} c_{A,\uparrow}^\dagger c_{B,\downarrow} = i \frac{2\lambda_R}{3} \left( \sqrt{3} \sin(\sqrt{3}/2ka) - \cos(\sqrt{3}/2) \right) c_{A,k,\uparrow}^\dagger c_{B,k,\downarrow}, \quad (\text{B.10b})$$

$$i \frac{2\lambda_R}{3} c_{A,\downarrow}^\dagger c_{B,\uparrow} = i \frac{2\lambda_R}{3} \left( -\sqrt{3} \sin(\sqrt{3}/2ka) - \cos(\sqrt{3}/2) \right) c_{A,k,\downarrow}^\dagger c_{B,k,\uparrow}. \quad (\text{B.10c})$$

For CD, we have:

$$= i \frac{2\lambda_R}{3V} \left( \sum_k e^{-ikr} c_{C,k}^\dagger \right) \left\{ \sum_{k'} \left[ \left( -\frac{1}{2}\sigma_x + \frac{\sqrt{3}}{2}\sigma_y \right) e^{ik'(r+a\sqrt{3}/2\hat{i}+a/2\hat{j})} + \left( -\frac{1}{2}\sigma_x - \frac{\sqrt{3}}{2}\sigma_y \right) e^{ik'(r-a\sqrt{3}/2\hat{i}+a/2\hat{j})} \right] c_{D,k'} \right\}, \quad (\text{B.11a})$$

$$i \frac{2\lambda_R}{3} c_{C,\uparrow}^\dagger c_{D,\downarrow} = i \frac{2\lambda_R}{3} \lambda_R \left( \sqrt{3} \sin(\sqrt{3}/2ka) - \cos(\sqrt{3}/2ka) \right) c_{C,k,\uparrow}^\dagger c_{D,k,\downarrow}, \quad (\text{B.11b})$$

$$i\frac{2\lambda_R}{3}c_{C,\downarrow}^{\dagger}c_{D,\uparrow}=i\frac{2\lambda_R}{3}\left(-\sqrt{3}\sin(\sqrt{3}/2ka)-\cos(\sqrt{3}/2ka)\right)c_{C,k,\downarrow}^{\dagger}c_{D,k,\uparrow}. \quad (\text{B.11c})$$

For CB, we have:

$$i\frac{2\lambda_R}{3}c_C^{\dagger}c_B=i\frac{2\lambda_R}{3V}\left(\sum_ke^{-ikr}c_{C,k}^{\dagger}\right)\left(\sum_{k'}\sigma_xe^{-ik'(r+a\hat{j})}c_{B,k'}\right), \quad (\text{B.12a})$$

$$i\frac{2\lambda_R}{3}c_{C,\uparrow}^{\dagger}c_{B,\downarrow}=i\frac{2\lambda_R}{3}c_{C,\uparrow}^{\dagger}c_{B,\downarrow}, \quad (\text{B.12b})$$

$$i\frac{2\lambda_R}{3}c_{C,\downarrow}^{\dagger}c_{B,\uparrow}=i\frac{2\lambda_R}{3}c_{C,\downarrow}^{\dagger}c_{B,\uparrow}. \quad (\text{B.12c})$$

## Matrix

Now we consider a system with N strips as in figure B.1. It is easy to see that the interactions between sites will repeat with periodicity of two sites, i.e. the site n has the same interactions of n+2, this is valid however, only away from the edges that will miss some interactions.

We have all terms calculated we just need to organize them in the matrix being careful only at the edges. We can get the Matrix that will be a bloc matrix with each of the 4 blocs of size 2(N+1).

$$\begin{pmatrix} H_+ & H_R \\ H_R^{\dagger} & H_- \end{pmatrix}, \quad (\text{B.13a})$$

$$H_{\pm} = \begin{pmatrix} a_{\pm 1} & b_{\pm 1} & c_{\pm 1} & 0 & \cdots & 0 & 0 & 0 & 0 \\ b_{\pm 1} & a_{\pm 2} & b_{\pm 2} & c_{\pm 2} & 0 & \cdots & 0 & 0 & 0 \\ c_{\pm 1} & b_{\pm 2} & a_{\pm 1} & b_{\pm 1} & c_{\pm 1} & 0 & \cdots & 0 & 0 \\ 0 & c_{\pm 2} & b_{\pm 1} & a_{\pm 2} & b_{\pm 2} & c_{\pm 2} & 0 & \cdots & 0 \\ 0 & \ddots & 0 \\ \vdots & \ddots & \vdots \\ 0 & \cdots & 0 & 0 & c_{\pm 2} & b_{\pm 1} & a_{\pm 2} & b_{\pm 2} & c_{\pm 2} \\ 0 & \cdots & 0 & 0 & 0 & c_{\pm 1} & b_{\pm 2} & a_{\pm 1} & b_{\pm 1} \\ 0 & \cdots & 0 & 0 & 0 & 0 & c_{\pm 2} & b_{\pm 1} & a_{\pm 2} \end{pmatrix}, \quad (\text{B.13b})$$

$$H_R = \begin{pmatrix} 0 & -i\lambda_R\Omega_+ & 0 & \cdots & 0 & 0 & 0 & 0 \\ i\lambda_R\Omega_- & 0 & i\lambda_R & 0 & \cdots & 0 & 0 & 0 \\ 0 & -i\lambda_R & 0 & -i\lambda_R\Omega_+ & 0 & \cdots & 0 & 0 \\ 0 & 0 & i\lambda_R\Omega_- & 0 & i\lambda_R & 0 & \cdots & 0 \\ 0 & \ddots \\ 0 & \cdots & 0 & 0 & 0 & 0 & i\lambda_R\Omega_- & 0 \end{pmatrix}, \quad (\text{B.13c})$$

with  $a_{\pm i}, b_{\pm i}, c_{\pm i}$  and  $\Omega_{\pm}$  given by the table B.1.

$a_{\pm 1}$	$(\lambda_{\nu} - \mu) \mp 2\sqrt{3}/3\lambda_{SO} \sin(\sqrt{3}ka)$
$a_{\pm 2}$	$(-\lambda_{\nu} - \mu) \pm 2\sqrt{3}/3\lambda_{SO} \sin(\sqrt{3}ka)$
$b_{\pm 1}$	$2t \cos(\sqrt{3}/2ka)$
$b_{\pm 2}$	$t$
$c_{\pm 1}$	$\pm 2\sqrt{3}/3\lambda_{SO} \sin(\sqrt{3}/2ka)$
$c_{\pm 2}$	$\mp 2\sqrt{3}/3\lambda_{SO} \sin(\sqrt{3}/2ka)$
$\Omega_{\pm}$	$\pm \sqrt{3} \sin(\sqrt{3}/2ka) - \cos(\sqrt{3}/2ka)$

Table B.1: Table of values used to write the Hamiltonian at Eq. B.13



# Appendix C

## Oscillations

In this appendix we show more plots for different  $\theta$  and  $\mu$  so the reader can compare the overall change in oscillations due to  $\lambda_R$ . We also show the effects of increasing  $\lambda_{SO}$  and  $\lambda_v$  for  $\theta \neq 0$ .

We start with plots of different  $\lambda_{SO}$  for  $\theta = 3\pi/2$ :

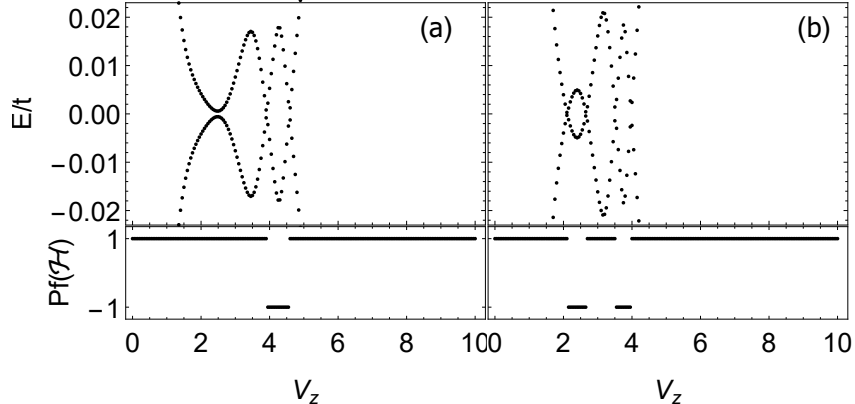


Figure C.1:  $\mu=0.4$  and  $\theta = 3\pi/2$ . Oscillations with varying impurity strength  $V_z$  for  $\lambda_{so}$  (a)  $0.1t$  and (b)  $0.3t$ .

This plot is interesting because we can see that a gap around  $V_z = 2.5t$  with no oscillation, it becomes an oscillation with opposite sign of Pfaffian. This shows that increasing spin-orbit coupling might also increase the number of oscillations.

Below we have a plot for  $\lambda_v$  with  $\theta = \pi/2$ . Although similar with the one showed in the results, here we can see that the first oscillation is smaller with increase  $\lambda_v$ .

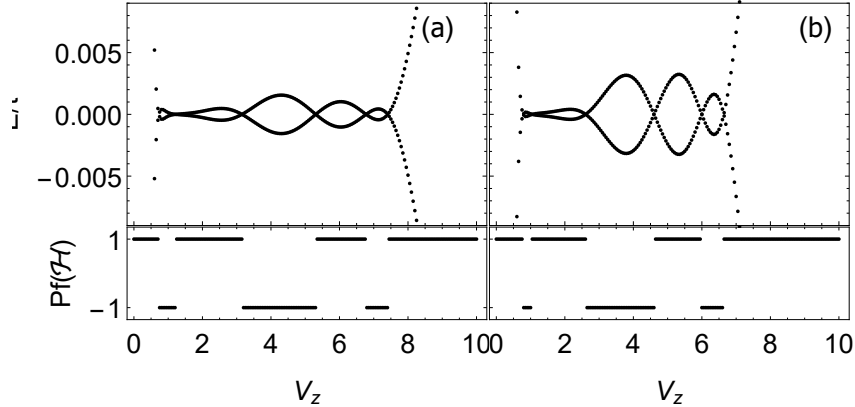


Figure C.2:  $\mu=0.4$  and  $\theta = \pi/2$ . Oscillations with varying impurity strength  $V_z$  for  $\lambda_v$  (a)  $0.05t$  and (b)  $0.1t$ .

Now we present many plots with  $\lambda_R$  for different  $\theta$  to show how deformation of the oscillations may happen and generic features of this oscillations.

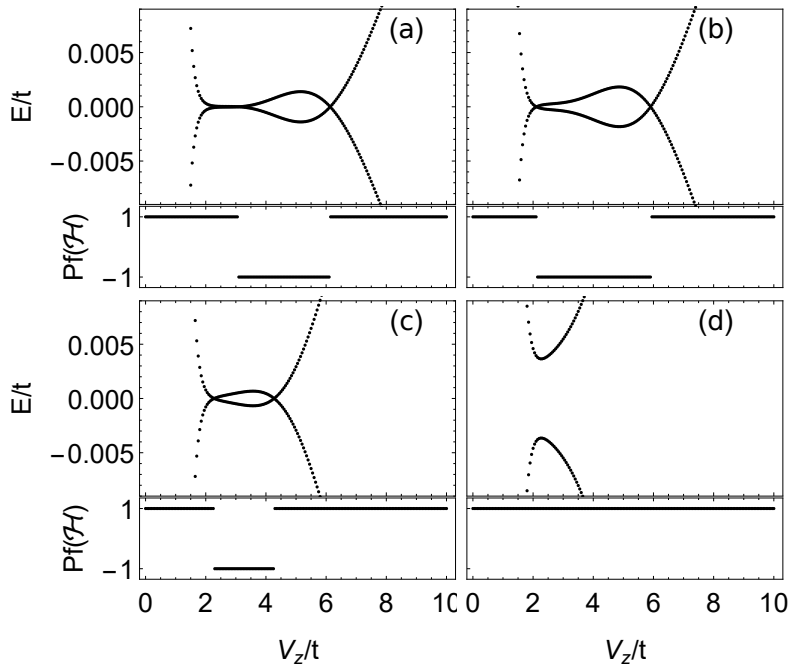


Figure C.3:  $\mu=0.4$   $\theta = \pi$ . Oscillations with varying impurity strength  $V_z$  for  $\lambda_r$  (a) 0, (b)  $0.05t$ , (c)  $0.1t$  and (d)  $0.15t$ .

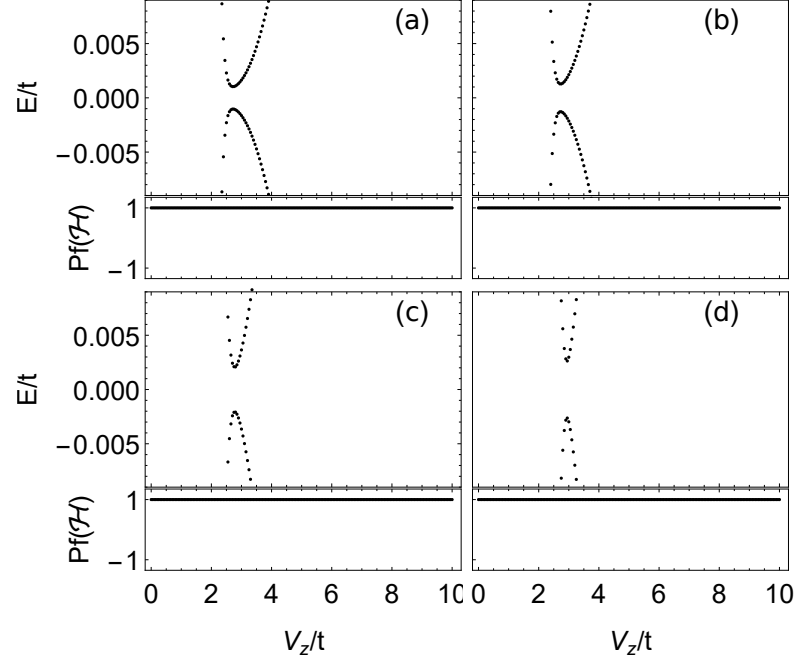


Figure C.4:  $\mu=0.4$   $\theta=0$ . Oscillations with varying impurity strength  $V_z$  for  $\lambda_r$  (a) 0, (b)  $0.05t$ , (c)  $0.1t$  and (d)  $0.15t$ .

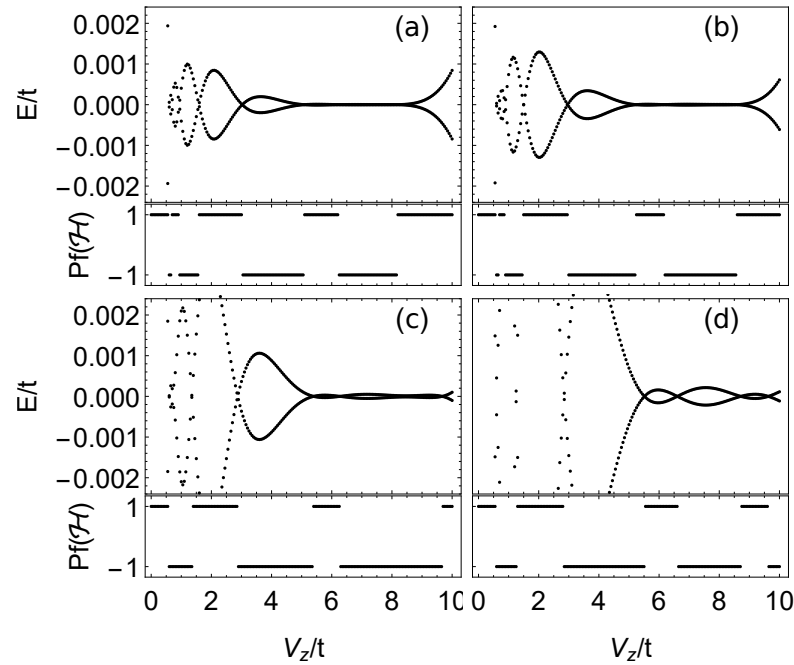


Figure C.5:  $\mu=0.2$   $\theta=0$ . Oscillations with varying impurity strength  $V_z$  for  $\lambda_r$  (a) 0, (b)  $0.05t$ , (c)  $0.1t$  and (d)  $0.15t$ .

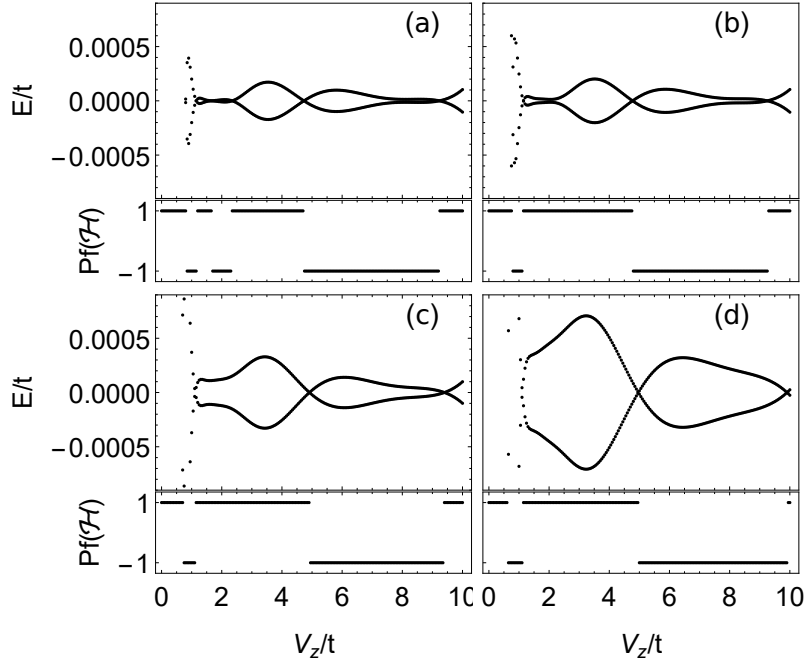


Figure C.6:  $\mu=0.2$   $\theta = \pi/2$ . Oscillations with varying impurity strength  $V_z$  for  $\lambda_r$  (a) 0, (b)  $0.05t$ , (c)  $0.1t$  and (d)  $0.15t$ .

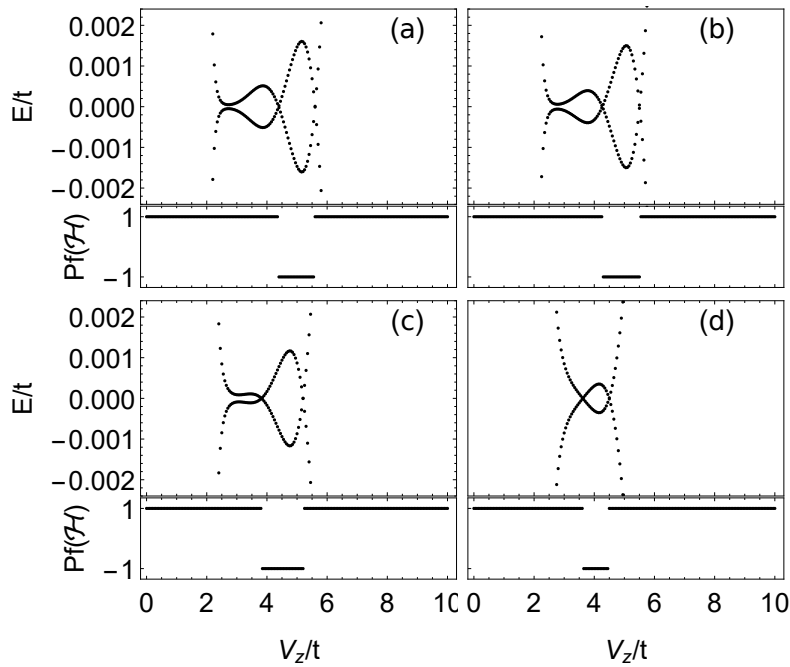


Figure C.7:  $\mu=0.2$   $\theta = \pi$ . Oscillations with varying impurity strength  $V_z$  for  $\lambda_r$  (a) 0, (b)  $0.05t$ , (c)  $0.1t$  and (d)  $0.15t$ .

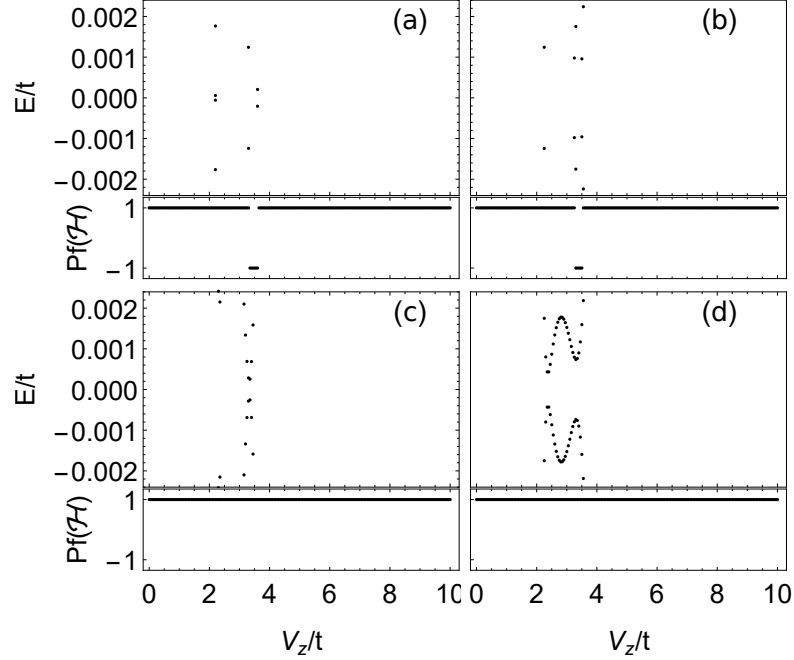


Figure C.8:  $\mu=0.2$   $\theta = 0$ . Oscillations with varying impurity strength  $V_z$  for  $\lambda_r$  (a) 0, (b)  $0.05t$ , (c)  $0.1t$  and (d)  $0.15t$ .

we conclude this appendix showing the effect of varying  $\mu$  for  $\theta = \pi$ . In this case we don't have oscillation for  $V_z = 1.45t$  but we do have it for  $V_z = 1.85t$ , but they are so small that we can only notice because of the change in Pfaffian.

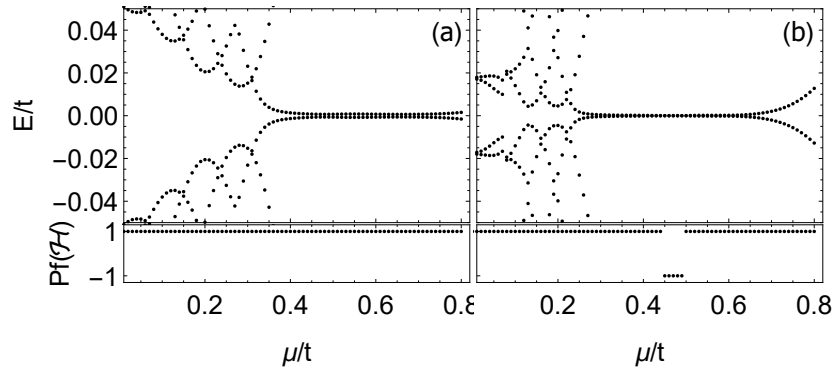


Figure C.9:  $\theta = 0$ . Oscillations with varying doping  $\mu$  for  $V_z$  (a)  $1.45t$  and (b)  $1.85t$ .



# Bibliography

- [1] C. L. Kane and E. J. Mele. Quantum spin hall effect in graphene. *Physical Review Letters*, 95(22), nov 2005.
- [2] S. Das Sarma, Jay D. Sau, and Tudor D. Stanescu. Splitting of the zero-bias conductance peak as smoking gun evidence for the existence of the majorana mode in a superconductor-semiconductor nanowire. *Phys. Rev. B*, 86:220506, Dec 2012.
- [3] Jason Alicea. New directions in the pursuit of majorana fermions in solid state systems. *Reports on Progress in Physics*, 75(7):076501, jun 2012.
- [4] C. L. Kane and E. J. Mele.  $Z_2$ . *Phys. Rev. Lett.*, 95:146802, Sep 2005.
- [5] Lan Chen, Baojie Feng, and Kehui Wu. Observation of a possible superconducting gap in silicene on ag(111) surface. *Applied Physics Letters*, 102(8):081602, 2013.
- [6] D. J. Thouless, M. Kohmoto, M. P. Nightingale, and M. den Nijs. Quantized hall conductance in a two-dimensional periodic potential. *Phys. Rev. Lett.*, 49:405–408, Aug 1982.
- [7] B.A. Bernevig and T.L. Hughes. *Topological Insulators and Topological Superconductors*. Princeton University Press, 2013.
- [8] Nobel Media AB 2014. The nobel prize in physics 2016. [http://www.nobelprize.org/nobel\\_prizes/physics/laureates/2016/](http://www.nobelprize.org/nobel_prizes/physics/laureates/2016/). Accessed: 2018-02-08.
- [9] Nobel Media AB 2014. The nobel prize in physics 2010. [http://www.nobelprize.org/nobel\\_prizes/physics/laureates/2010/](http://www.nobelprize.org/nobel_prizes/physics/laureates/2010/). Accessed: 2018-01-08.
- [10] M. Spencer and T. Morishita. *Silicene: Structure, Properties and Applications*. Springer Series in Materials Science. Springer International Publishing, 2016.

- [11] Yusuf Shaidu and Omololu Akin-Ojo. First principles predictions of superconductivity in doped stanene. *Computational Materials Science*, 118(Supplement C):11 – 15, 2016.
- [12] A Yu Kitaev. Unpaired majorana fermions in quantum wires. *Physics-Uspekhi*, 44(10S):131, 2001.
- [13] V. Mourik, K. Zuo, S. M. Frolov, S. R. Plissard, E. P. A. M. Bakkers, and L. P. Kouwenhoven. Signatures of majorana fermions in hybrid superconductor-semiconductor nanowire devices. *Science*, 336(6084):1003–1007, apr 2012.
- [14] C.W.J. Beenakker. Search for majorana fermions in superconductors. *Annu. Rev. Condens. Matter Phys.*, 4(1):113–136, apr 2013.
- [15] Sven Marian Albrecht, A. P. Higginbotham, Morten Madsen, Ferdinand Kuemmeth, Thomas Sand Jespersen, Jesper Nygård, Peter Krogstrup, and C. M. Marcus. Exponential protection of zero modes in majorana islands. *Nature*, 531(7593):206–209, 3 2016.
- [16] M. Nakahara. *Geometry, Topology and Physics, Second Edition*. Graduate student series in physics. Taylor & Francis, 2003.
- [17] M. Franz and L. Molenkamp. *Topological Insulators*. Contemporary Concepts of Condensed Matter Science. Elsevier Science, 2013.
- [18] S.Q. Shen. *Topological Insulators: Dirac Equation in Condensed Matter*. Springer Series in Solid-State Sciences. Springer-Verlag Berlin Heidelberg, 2012.
- [19] F. D. M. Haldane. Model for a quantum hall effect without landau levels: Condensed-matter realization of the "parity anomaly". *Phys. Rev. Lett.*, 61:2015–2018, Oct 1988.
- [20] Laura Cano-Cortés, Carmine Ortix, and Jeroen van den Brink. Fundamental differences between quantum spin hall edge states at zigzag and armchair terminations of honeycomb and ruby nets. *Phys. Rev. Lett.*, 111:146801, Oct 2013.
- [21] Chung-Hou Chung, Der-Hau Lee, and Sung-Po Chao. Kane-mele hubbard model on a zigzag ribbon: Stability of the topological edge states and quantum phase transitions. *Phys. Rev. B*, 90:035116, Jul 2014.

- [22] M. Tinkham. *Introduction to Superconductivity: Second Edition.* Dover Books on Physics. Dover Publications, 2004.
- [23] Annica M. Black-Schaffer and Sebastian Doniach. Effect of nearest neighbor spin-singlet correlations in conventional graphene sns josephson junctions. *Phys. Rev. B*, 79:064502, Feb 2009.
- [24] J.X. Zhu. *Bogoliubov-de Gennes Method and Its Applications.* Lecture Notes in Physics. Springer International Publishing, 2016.
- [25] Annica M. Black-Schaffer. Self-consistent superconducting proximity effect at the quantum spin hall edge. *Physical Review B*, 83(6), feb 2011.
- [26] Morten H. Christensen, Michael Schechter, Karsten Flensberg, Brian M. Andersen, and Jens Paaske. Spiral magnetic order and topological superconductivity in a chain of magnetic adatoms on a two-dimensional superconductor. *Phys. Rev. B*, 94:144509, Oct 2016.
- [27] Kristofer Björnson, Alexander V. Balatsky, and Annica M. Black-Schaffer. Superconducting order parameter  $\pi$ -phase shift in magnetic impurity wires. *Phys. Rev. B*, 95:104521, Mar 2017.
- [28] Steven R. Elliott and Marcel Franz. Colloquium : Majorana fermions in nuclear, particle, and solid-state physics. *Reviews of Modern Physics*, 87(1):137–163, feb 2015.
- [29] Martin Leijnse and Karsten Flensberg. Introduction to topological superconductivity and majorana fermions. *Semiconductor Science and Technology*, 27(12):124003, nov 2012.
- [30] Bernard van Heck. Braiding of majoranas. [https://topocondmat.org/w2\\_majorana/braiding.html](https://topocondmat.org/w2_majorana/braiding.html). Accessed: 2017-12-27.
- [31] I. Reis, D. J. J. Marchand, and M. Franz. Self-organized topological state in a magnetic chain on the surface of a superconductor. *Phys. Rev. B*, 90:085124, Aug 2014.

- [32] Ching-Kai Chiu, Jay D. Sau, and S. Das Sarma. Conductance of a superconducting coulomb-blockaded majorana nanowire. *Phys. Rev. B*, 96:054504, Aug 2017.
- [33] Chun-Xiao Liu, Jay D. Sau, Tudor D. Stanescu, and S. Das Sarma. Andreev bound states versus majorana bound states in quantum dot-nanowire-superconductor hybrid structures: Trivial versus topological zero-bias conductance peaks. *Phys. Rev. B*, 96:075161, Aug 2017.
- [34] M. Wimmer. Algorithm 923: Efficient numerical computation of the pfaffian for dense and banded skew-symmetric matrices. *ACM Trans. Math. Softw.*, 38(4):30:1–30:17, August 2012.